



UNIVERSIDADE FEDERAL DO CEARÁ
CENTRO DE CIÊNCIAS
DEPARTAMENTO DE FÍSICA
DOUTORADO EM FÍSICA

LUCAS SAMIR RAMALHO CAVALCANTE

OPTOELECTRONICS IN TWO DIMENSIONAL MATERIALS

FORTALEZA
2020

LUCAS SAMIR RAMALHO CAVALCANTE

OPTOELECTRONICS IN TWO DIMENSIONAL MATERIALS

Tese apresentada ao Curso de Pós-graduação em Física da Universidade Federal do Ceará como parte dos requisitos necessários para a obtenção do título de Doutor em Física.

Orientador: Prof. Dr. Andrey Chaves

Co-Orientador: Prof. Dr. Kristian Sommer Thygesen

Fortaleza
2020

Dados Internacionais de Catalogação na Publicação
Universidade Federal do Ceará
Biblioteca Universitária
Gerada automaticamente pelo módulo Catalog, mediante os dados fornecidos pelo(a) autor(a)

C364o Cavalcante, Lucas Samir Ramalho.

Optoelectronics in two dimensional materials / Lucas Samir Ramalho Cavalcante. – 2020.
109 f. : il. color.

Tese (doutorado) – Universidade Federal do Ceará, Centro de Ciências, Programa de Pós-Graduação em Física, Fortaleza, 2020.

Orientação: Prof. Dr. Andrey Chaves.

Coorientação: Prof. Dr. Kristian Sommer Thygesen.

1. optoelectronics. 2. two dimensional materials. 3. electrostatic transfer matrix. 4. quantum electrostatic heterostructure. I. Título.

CDD 530

Lucas Samir Ramalho Cavalcante

OPTOELECTRONICS IN TWO DIMENSIONAL MATERIALS

Tese apresentada ao Curso de Pós-graduação em Física da Universidade Federal do Ceará como parte dos requisitos necessários para a obtenção do título de Doutor em Física.

Orientador: Prof. Dr. Andrey Chaves

Co-Orientador: Prof. Dr. Kristian Sommer Thygesen

Aprovada em: 28/05/2020.

BANCA EXAMINADORA

Prof. Dr. Andrey Chaves (Orientador)
Departamento de Física – UFC

Prof. Dr. Kristian Sommer Thygesen (Co-Orientador)
Departamento de Física – DTU

Prof. Dr. João Milton Pereira Jr.
Departamento de Física – UFC

Prof. Dr. Jeanlex Soares de Sousa
Departamento de Física – UFC

Prof. Dr. André Jorge Carvalho Chaves
Divisão de Ciências Fundamentais – ITA

*Dedicated to mom and dad, Ana and Cavalcante, and to the
love of my life, Lia.*

Aknowledgements

I wish to express my gratitude to the people that contributed to the completion of this work.

To my parents, Francisco Cavalcante and Ana Clara, for their unconditional support. I will be forever grateful. Also, to my brothers, Felipe and Isaac, for the companionship and friendship built during all my life. To my wife, Lia, for the love and care. Without her adventurous spirit, most of our great experiences would not be possible. To her grandmother, Leda, for her wisdom and patience.

To Prof. Andrey Chaves for all the teaching and dedication offered so brilliantly. To Prof. Kristian Thygesen for providing an amazing professional experience and for his caring attitude during my time at Denmark. To Dr. Morten Gjerging for his guidance and friendship.

To my friends from GTMC, Duarte, Gabriel, Johnathas and Luan for the support, companionship and love.

This study was supported by the Coordenação de Aperfeiçoamento de Pessoal de Nível Superior - Brasil (CAPES) - Finance Code 001.

"What I cannot create, I do not understand."

Richard P. Feynman

Resumo

Excitons, i.e., aglomerados de elétrons e buracos ligados, e plasmons, oscilações coletivas de densidade eletrônica, desempenham um papel fundamental nas interações luz-matéria em materiais semicondutores. Estudamos complexos excitônicos e efeitos plasmônicos em materiais bidimensionais de van der Waals em contextos diferentes. Nós nos concentramos em materiais que recentemente atraíram atenção por causa de suas propriedades optoeletrônicas interessantes, como grafeno, fósforo negro em poucas camadas, TMDCs e suas heteroestruturas.

Inicialmente, o papel da blindagem dielétrica na interação elétron-buraco em heteroestruturas de van der Waals é teoricamente investigado. É feita uma comparação entre os modelos disponíveis na literatura para descrever essas interações e as limitações dessas abordagens são discutidas. Uma solução numérica simples da equação de Poisson para o empilhamento de camadas dielétricas baseada em um método de matriz de transferência é desenvolvida, permitindo o cálculo do potencial de interação elétron-buraco a um custo computacional muito baixo e com precisão razoável. Usando diferentes modelos de potencial, as energias de ligação de exciton direto e indireto nesses sistemas são calculadas dentro da teoria de Wannier-Mott, e é discutida uma comparação de resultados teóricos com experimentos recentes sobre excitons em materiais bidimensionais.

Paralelamente, o modelo *quantum electrostatic heterostructure* (QEH) permite um cálculo eficiente do vetor de onda e da função dielétrica dependente da frequência de heteroestruturas de van der Waals através das funções dielétricas das camadas individuais, que são acopladas classicamente através da interação eletrostática de Coulomb. Aqui, estendemos o modelo QEH incluindo (1) a contribuição dos fônons infravermelhos ativos das camadas 2D para a função dielétrica, (2) a possibilidade de incluir efeitos de substratos e (3) a possibilidade de incluir a blindagem intrabanda de portadores de carga livres em camadas semicondutoras dopadas. Demonstramos o potencial do modelo QEH calculando a dispersão de fônons eletrostaticamente acoplados em multicamadas de nitreto de boro hexagonal (hBN), a forte hibridização de plasmons e fônons ópticos em heteroestruturas de grafeno/hBN, incluindo o surpreendente longo alcance do efeito de blindagem de substrato composto por SiO₂, o efeito da blindagem do substrato nos níveis de excitons de MoS₂ e as propriedades de plasmons hiperbólicos em uma folha de fosforeno dopado. O novo código QEH é distribuído como um pacote Python com uma interface simples de linha de comando e uma biblioteca abrangente de blocos dielétricos (DBB) está disponível gratuitamente, fornecendo uma plataforma aberta e eficiente para modelagem e design de heteroestruturas de vdW.

Nós empregamos o método QEH para explorar o uso de camadas de materiais Janus, e.g. MoSSe, que possuem um dipolo elétrico intrínseco causado por sua assimetria estrutural fora do plano, para dopar seletivamente grafeno em uma heteroestrutura sem

a necessidade de fontes externas (como *gates* eletrostáticos ou funcionalização química) para excitar plasmons em grafeno. Demonstramos que, através do controle da energia plasmônica por meio do nível de dopagem e da hibridização de plasmons em diferentes camadas, podemos atingir energias plasmônicas de grafeno até 0.5 eV ou extinguir seletivamente certos modos (simétricos) pelo amortecimento de Landau. A possibilidade de usar outros dicalcogenetos de metais de transição Janus que possam melhorar esse efeito também é investigada.

Finalmente, desenvolvemos um estudo teórico do efeito de um campo elétrico externo aplicado no plano em estados de excitons carregados. Demonstramos que esses estados são fortemente ligados, de modo que a dissociação do par elétron-buraco não é observada até altas intensidades de campo elétrico. As polarizabilidades dos excitons são obtidas a partir da parabolicidade do efeito de *Stark shift* calculado numericamente. Para trions (excitons carregados), no entanto, é observada uma variação de quarta ordem na energia, que permite a verificação experimental da hiperpolarizabilidade em materiais 2D, como observado em estados altamente excitados da série de Rydberg em átomos e íons. Além disso, uma energia de ligação tão alta de excitons carregados pode permitir sistemas onde os trions são transportados no plano dos materiais por um campo externo aplicado, abrindo espaço para possíveis novas aplicações de dispositivos optoeletrônicos no futuro.

Abstract

Excitons, i.e. clusters of bound electrons and holes, and plasmons, collective oscillations of electronic density, play a fundamental role in light-matter interactions in semiconductor materials. We study excitonic complexes and plasmonic effects in two-dimensional van der Waals materials within many different contexts. We focus on materials that have recently attracted attention because of their interesting optoelectronic properties, such as graphene, few-layers black phosphorus, TMDCs, and their heterostructures.

Initially, the role of dielectric screening of electron-hole interaction in van der Waals heterostructures is theoretically investigated. A comparison between models available in the literature for describing these interactions is made and the limitations of these approaches are discussed. A simple numerical solution of Poisson's equation for a stack of dielectric slabs based on a transfer matrix method is developed, enabling the calculation of the electron-hole interaction potential at very low computational cost and with reasonable accuracy. Using different potential models, direct and indirect exciton binding energies in these systems are calculated within Wannier-Mott theory, and a comparison of theoretical results with recent experiments on excitons in two-dimensional materials is discussed.

In parallel, the quantum electrostatic heterostructure (QEH) model enables an efficient computation of the wave vector and frequency-dependent dielectric function of layered van der Waals bonded heterostructures in terms of the dielectric functions of the individual layers, which are coupled classically via the electrostatic Coulomb interaction. Here we extend the QEH model by including (1) the contribution to the dielectric function from infrared active phonons of the 2D layers, (2) the possibility of including screening from homogeneous bulk substrates, and (3) the possibility to include intraband screening from free carriers in doped semiconducting layers. We demonstrate the potential of the QEH model by calculating the dispersion of electrostatically coupled phonons in multilayer stacks of hexagonal boron-nitride (hBN), the strong hybridization of plasmons and optical phonons in graphene/hBN heterostructures including the surprisingly long ranged effect of a SiO₂ substrate, the effect of substrate screening on the exciton series of MoS₂, and the properties of hyperbolic plasmons in a doped phosphorene sheet. The new QEH code is distributed as a Python package with a simple command line interface and comprehensive library of dielectric building blocks are freely available providing an efficient open platform for modeling and design of vdW heterostructures.

We employ the QEH method to explore the use of MoSSe Janus layers, which possess an intrinsic electric dipole caused by their out-of-plane structural asymmetry, to selectively dope graphene embedded inside a heterostructure without the need of external sources (such as electrostatic gates or chemical functionalization) in order to engineer graphene plasmons. We demonstrate that, through the control of the plasmon energy via the doping level and the hybridization of plasmons in different layers, we can reach graphene plasmon

energies up to 0.5 eV or selectively quench certain (symmetric) modes by Landau damping. The possibility of using other Janus transition-metal dichalcogenides that could improve this effect is also investigated.

Further work is then developed on the theoretical study of the effect of an external in-plane electric field on charged exciton states. These states are shown to be strongly bound so that electron hole dissociation is not observed up to high electric field intensities. Polarizabilities of excitons are obtained from the parabolicity of numerically calculated Stark shifts. For trions (charged excitons), however, a fourth order Stark shift is observed, which enables the experimental verification of hyperpolarizability in 2D materials, as observed in highly excited states of Rydberg series of atoms and ions. Moreover, such a high binding energy of charged excitons may allow for systems where trions are carried through the materials plane by an applied external field, which opens an avenue for possible novel optoelectronic device applications in the future.

Contents

Resumo	8
Abstract	10
List of Figures	14
List of Tables	20
1 Introduction	21
1.1 Two dimensional materials	21
1.2 Exciton	25
1.3 Trion	29
1.4 Plasmon	31
1.5 Scope of the thesis	35
2 Electrostatics of electron-hole interactions in van der Waals heterostructures	36
2.1 Motivation	36
2.2 Theoretical framework	37
2.2.1 Electrostatic transfer matrix method	38
2.2.2 Quantum Electrostatic Heterostructure Model	39
2.2.3 Wannier-Mott Model	40
2.3 Results and discussion	41
2.3.1 Classical limits	41
2.3.2 Inter layer excitons in hetero-bilayers	45
2.3.3 Dielectric screening due to a graphene capping layer	48
3 Efficient ab-initio based modeling of dielectric screening in 2D heterostructures	50

3.1	Motivation	50
3.2	Theoretical framework	51
3.2.1	Basics of the QEH model	51
3.2.2	Lattice polarization	53
3.2.3	Bulk substrates	54
3.2.4	Doped graphene	55
3.2.5	Doped 2D semi-conductors	55
3.3	Results and Discussion	56
3.3.1	Phonon polaritons in hBN multilayers	56
3.3.2	Plasmon-phonon coupling in graphene/hBN	58
3.3.3	Substrate screening of excitons in MoS ₂	59
3.3.4	Hyperbolic plasmons in doped phosphorene	61
3.4	QEH Python package	62
4	Enhancing and Controlling Plasmons in Janus MoSSe-Graphene Based van der Waals Heterostructures	63
4.1	Motivation	63
4.2	Computational Methods	64
4.3	Results and Discussion	64
5	Stark shift of excitons and trions in two-dimensional materials	72
5.1	Motivation	72
5.2	Theoretical model	73
5.3	Results and discussion	75
6	Concluding remarks	82
	Appendices	85
A	Effective mass model	86
B	Lattice polarizability: Derivation	88
C	Doping of anisotropic 2D semi-conductors	91
D	Plasmon propagation lengths	92
E	QEH library	94
F	Published papers	96
	Bibliography	101

List of Figures

1.1	Side and top view of MX_2	22
1.2	From left to right: DFT calculations of the band structure of single layer, bilayer and bulk MoS_2 in the LDA (thin dashed lines) and in the G_0W_0 approximation. [7]	22
1.3	From left to right: DFT calculations of the band structure of single layer, bilayer and trilayer BP. [5]	23
1.4	Side and top view of phosphorene.	23
1.5	Building van der Waals heterostructures. If one considers 2D crystals to be analogous to Lego blocks (right panel), the construction of a huge variety of layered structures becomes possible. [19]	24
1.6	(a) In semiconductors crystals, the upper full band is called valence band and the lowest empty one is called conduction band. (b) An electron is remove from valence and placed at conduction band leaving an empty state. (c) The valence band states behave as a particle with positive charge called hole that has momentum with opposite sign. Adapted Fig. from Ref.[30]	25
1.7	(a) Free electron in the conduction band \mathbf{k}_e interacts with a free valence hole \mathbf{k}_h via attractive Coulomb processes. (b) Bound state with momentum $\mathbf{Q} = \mathbf{k}_e + \mathbf{k}_h$ called Exciton. Adapted Fig. from [30]	26
1.8	(a) Cu_2O spectra measured with a single-frequency laser. Peaks are related to the principal quantum number n . The inferior panels show the close-up for higher values of n . (b) Exciton binding energies with dependence of n . The energies follow the Rydberg formula as they are fitted with a n^{-2} dependency.[36]	27

1.9	Absorption spectrum of monolayer MoS_2 at 10 K (solid green line) [38]. A and B are exciton resonances corresponding to transitions from the two spin-split valence bands to the conduction bands. The blue dashed line shows the absorbance (arbitrary units) if excitonic effects were absent. The inset illustrates the possible transitions considering spin orbit coupling, forming bound excitons. Adapted Fig. from [37].	28
1.10	(a) Free electron in the conduction band \mathbf{k}_e interacts with an exciton $\mathbf{Q} = \mathbf{k}_e + \mathbf{k}_h$ via attractive Coulomb processes. (b) Set of relevant coordinates for the relative motion of an χ^- trion.	29
1.11	Absorption and photoluminescence spectra (red lines) in the range of 1.8 - 2.0 eV for the indicated back-gate voltages. The exciton (A) and trion (A^-) resonances behave differently with gate voltage. Left: Absorption spectra, with the dashed blue lines as a guide to the eye for the threshold energies of A and A^- features. The green lines are power-law fits to the experimental results with the A and A^- components shown as the blue lines. Right: The photoluminescence spectra of the A and A^- features are fit to Lorentzians (green lines). The dashed blue line indicates the absorption peak of the A^- resonance and the arrows show the doping-dependent Stokes shift of the trion photoluminescence.[38]	30
2.1	(Color online) Sketch of the series of interfaces between slabs with dielectric constants ϵ_n describing each material layer. The charge (e) placed at the c -th slab generates a screened Coulomb potential at each layer, that obeys the Poisson equation with a space-dependent dielectric constant.	38
2.2	(Color online) (a) Average dielectric function for MoS_2 as calculated by QEH model for increasing number of layers. (b) Maximum value (red, left scale) of the curves shown in (a), along with their derivatives at $k = 0$ (black, right scale) as a function of the number of layers. Numerical results are shown as symbols. The curve on top of the ϵ_{max} (red) symbols is a fitting function (see text), whereas the one on top of the derivative results (black) is a guide to the eyes.	42
2.3	(Color online) (a) Effective dielectric function of a suspended monolayer MoS_2 as obtained by ETM and QEH methods, as well as with the Rytova-Keldysh effective potential approach. The effective interaction potential between electron and hole, as obtained by these methods, is shown in (b) and (c), for monolayer MoS_2 in the suspended case and over N_s layers of BN substrate, respectively.	43
2.4	(Color online) Screened interaction potential between electron and hole, as obtained by QEH (symbols) and ETM (curves) methods, for N-layer MoS_2 (a) in the suspended case, (b) over a BN substrate, and (c) encapsulated by a BN substrate and a BN capping medium.	43

2.5	(Color online) Exciton energy states, as obtained by ETM (black full circles) and QEH (red open squares) methods, for monolayer MoS ₂ (a) in the suspended case, (b) over a BN substrate, and (c) encapsulated by BN. Curves are guides to the eye.	44
2.6	(Color online) (a) Exciton ground state energy as a function of the number of MoS ₂ layers, as obtained by ETM (full symbols) and QEH (open symbols) methods, in the suspended case (black squares), over a BN substrate (red triangles), and encapsulated by BN (blue circles). (b) Relative difference between results obtained with the ETM and QEH methods. Lines are guides to the eye.	45
2.7	(Color online) Comparison between inter-layer electron-hole interaction potentials obtained by the ETM (solid) and the standard Coulomb form (dashed), for a MoS ₂ /WS ₂ heterostructure encapsulated by BN and with a N_s -layer BN spacer between the TMDCs, for $N_s = 0$ (black), 5 (red), 10 (blue) and 30 (green). Inset: comparison between inter-layer electron-hole interaction potentials for suspended MoS ₂ /WS ₂ hetero-bilayer, as obtained by ETM (black solid) and QEH (red symbols) methods.	47
2.8	(Color online) Difference between ground (1s) and first excited (2s) exciton states in WS ₂ as calculated by ETM (black circles), assuming substrate dielectric constants $\epsilon_s = 7.6\epsilon_0$ and $3.9\epsilon_0$. Experimental values for this system [55] are shown as red triangles.	48
3.1	Loss function (3.21) of a 10-layer hBN stack reveals the formation of subbands of longitudinal in-plane phonon-polaritons. The white dashed lines correspond to the in-plane TO and LO frequencies of bulk hBN. The well known breakdown of the LO-TO splitting in the $q \rightarrow 0$ for 2D materials is clearly seen. The strong hybridization of the LO sheet phonons leading to the subband formation is due to electrostatic interactions captured by the QEH model.	57
3.2	Loss function (3.21) of freestanding and supported graphene/hBN heterostructures. (a) Two doped graphene sheets separated by 3 layers of hBN. Only the electronic response is included in the dielectric building blocks. (b) Same as (a) but with the phonon contribution included in the hBN building blocks as indicated by a blurring of the atoms. (c) Same as (b) but with 18 layers of hBN added below the heterostructure. (d) Same as (c) but with the entire heterostructure placed on a SiO ₂ substrate. Screening from the substrate is described by the dielectric function in Eq. (3.22) with $\epsilon_\infty = 2.4\epsilon_0$, $f_j = (0.7514, 0.1503, 0.6011)$ and $\omega_{\text{TO},j} = (0.055, 0.098, 0.140)$ eV.	58

3.3	Effect of substrate screening on excitons in MoS ₂ . (a) We consider two different models for the substrate, namely n layers of hBN dielectric building blocks (model 1) and a homogeneous bulk dielectric (model 2). (b) Comparison of the dielectric function of the supported MoS ₂ layer obtained with the two different substrate models. The dielectric function of freestanding MoS ₂ is shown for comparison. Note that model 1 reproduces the 2D limit $\epsilon(q) \rightarrow 1$ for $q \rightarrow 0$ because the substrate has finite thickness. (c) Binding energies of the lowest five s excitons in MoS ₂ . (d) Exciton binding energies for the lowest exciton in MoS ₂ as function of the number of hBN layers included in model 1.	60
3.4	(a) Loss function of n-doped monolayer black phosphorus. The in-plane structural anisotropy is reflected by the different plasmon dispersion curves in the x and y directions. Dashed white lines indicate the Landau damped regions. (b) Isofrequency contours evaluated for $\hbar\omega = 0.1\text{eV}$ and $\hbar\omega = 0.2\text{eV}$ corresponding to the normal and hyperbolic frequency regimes, respectively.	61
4.1	Graphene doping level as a function of the number of MoSSe layers, for the structure illustrated in the inset, as calculated using DFT (blue) and the capacitor model (orange), with $t = 6.4 \text{ \AA}$, $\Delta_{\text{MoSSe}} = 0.51 \text{ eV}$ and $\epsilon = 1.76$	65
4.2	(a) Loss function for monolayer of MoSSe encapsulated by graphene, as illustrated in the inset, with $\epsilon_F = 0.2 \text{ eV}$ and relaxation rate of $\hbar\omega = 1 \text{ meV}$. Induced density presents one symmetric and one antisymmetric mode, as shown in (b) for the higher (top, orange) and lower (bottom, blue) energy branches at $q = 0.01 \text{ \AA}^{-1}$. The vertical dashed grey lines represent the graphene layers positions.	66
4.3	Doping level in the middle and external graphene layers of the structure illustrated in the inset, as a function of the number of MoSSe layers, as calculated using the capacitor model.	67
4.4	(a) Loss function for the heterostructure illustrated in the inset, composed by two external graphene layers ($\epsilon_F = 0.18 \text{ eV}$), one middle graphene layer ($\epsilon_F = 0.25 \text{ eV}$) and two layers of MoSSe with opposite orientation with relaxation rate of $\hbar\omega = 1 \text{ meV}$. White dashed lines delimit the region of Landau damping of the plasmon modes. (b) The induced densities for $q = 0.01 \text{ \AA}^{-1}$ now present three modes: two symmetric and one antisymmetric. The vertical dashed grey lines represent the graphene layers positions.	68

4.5	Comparison between loss functions of heterostructures composed by (a) five layers of MoSSe encapsulated by two graphene layers ($\epsilon_F = 0.36$ eV, $\hbar\omega = 1$ meV) and (b) ten layers of MoSSe, divided into two stacks of MoSSe with opposite orientations, intercalated and encapsulated by three layers of graphene ($\epsilon_{F,\text{external}} = 0.36$ eV and $\epsilon_{F,\text{middle}} = 0.50$ eV). White dashed lines delimit the Landau damping region of the plasmon modes of the outer graphene layers.	69
4.6	Loss function for two MoSSe layers encapsulated by graphene ($\epsilon_F = 0.29$ eV, $\hbar\omega = 1$ meV) where we add one (a) and two (b) layer(s) of graphene in the middle of the heterostructure.	70
4.7	Optical plasmon energies (orange circles) for different Janus TMDs composing the structure sketched on the inset of Fig. 4.5 (a), for $q = 0.001$ Å. Electron-hole pair continuum for each material is shown by blue bars.	70
5.1	(a) Sketch of the top view of the TMDC and BP crystal lattices, along with the direction of F_x and F_y components of the applied field. Stark shift of exciton binding energies in (b) MoS ₂ , in the suspended, on-substrate, and encapsulated cases, and in (c,d) suspended phosphorene with different numbers of layers. In the latter, results are shown for fields applied in the y - and x -direction respectively (c,d). The values of polarizability (fitting parameters) are presented in Table 5.1.	74
5.2	(a) Numerically obtained (symbols) field dependence of the trion binding energy E_b in monolayer MoS ₂ in the suspended case, on a BN substrate, and encapsulated by BN. The values of polarizability and hyperpolarizability (fitting parameters for the curves) are presented in Table 5.3. (b) Countour map of the square modulus of the trion wave function in suspended MoS ₂ with x and y axis in angstrom. The square modulus of the wave function is calculated by an integral in the coordinates that are not variables in each plot. The left (right) column represents the exciton's (trion's) center of mass wave function in the absence of electric field in the first row, and for a $F = 60$ kV/cm field applied in the x -direction in the second row. The colour scale goes from 0 (blue, MIN) to 0.012 (red, MAX).	76
5.3	Comparison between fitting curves of second and fourth order corrections (lines) to the numerically obtained Stark shift of trions (symbols) in suspended MoS ₂ . For the former, two cases are considered, namely with and without a first order term in the fitting expression (see manuscript).	77

5.4 (a) Numerically obtained (symbols) electric field dependence of the binding energy E_b for trions in phosphorene with different number of layers for a field applied in the y (left) and x (right) directions. The values of polarizability and hyperpolarizability (fitting parameters for the curves) are presented in Table 5.3. (b) Countour maps of the square modulus of the trion wave function in suspended monolayer BP with x and y axis in angstrom. The left (right) column represents the exciton (trion) center-of-mass wave function in the absence of electric field in the first row, and for a $F = 60$ kV/cm field applied in the x -direction in the second row, and $F = 100$ kV/cm applied in the y -direction in the third row. The colour scale ranges from 0 (blue, MIN) to 0.018 (red, MAX) 78

List of Tables

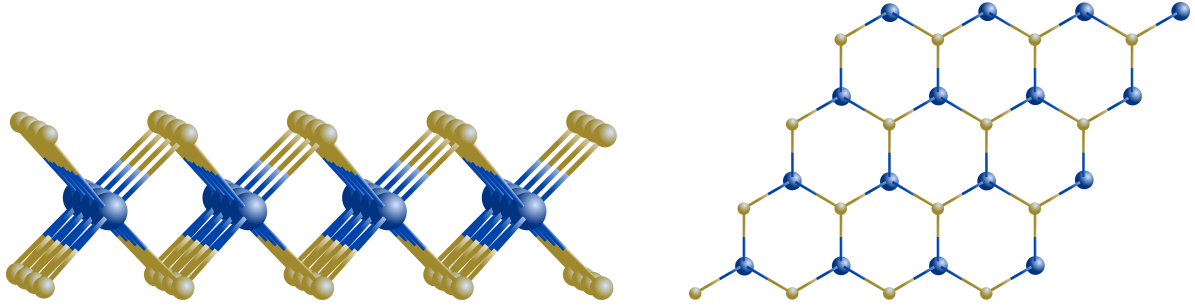
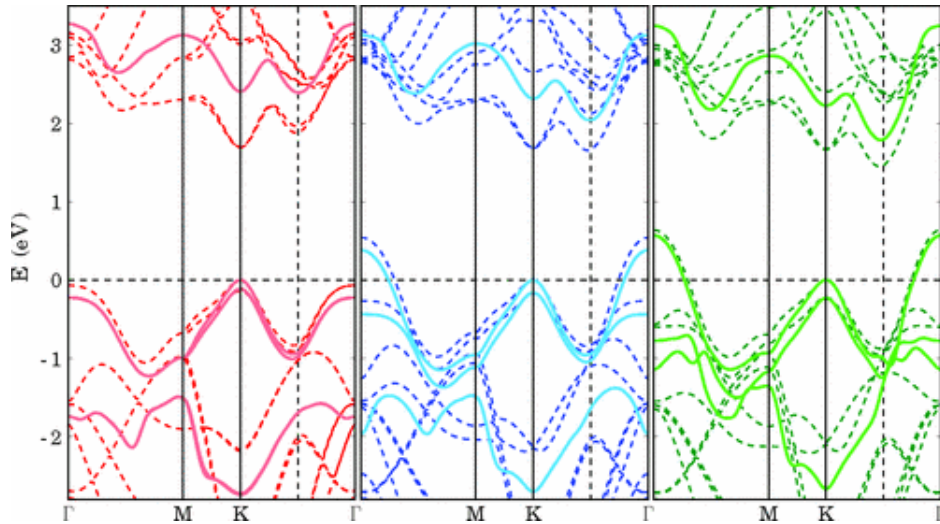
- 5.1 Exciton polarizabilities for monolayer TMDC and *n*-BP in the suspended, on substrate and encapsulated cases, in units of 10^{-5} meVcm²/kV². Results inside (outside) the brackets for *n*-BP are for electric fields applied in *x* and *y* directions, respectively. 80
- 5.2 Trion binding energies (in meV), in the absence of electric fields, for monolayer TMDCs and *n*-BP in the suspended case, on a BN substrate, and encapsulated by BN, respectively. 80
- 5.3 Trions polarizabilities / hyperpolarizabilities for monolayer TMDCs and *n*-BP in the suspended, on substrate and encapsulated cases, in units of 10^{-5} meVcm²/kV² / 10^{-7} meVcm⁴/kV⁴. Results in the middle (bottom) for *n*-BP are for electric fields applied in *x* and *y* directions, respectively. . . 81

1.1 Two dimensional materials

The experimental production of graphene in 2004, through mechanical exfoliation of a highly oriented pyrolytic graphite sample [1], demonstrated that it was possible to obtain a stable two-dimensional crystal, emerging a search for new materials whose crystalline structure was similar to that of graphite, that is, composed of layers of atoms stacked and weakly bound by van der Waals bonds, allowing exfoliation in monolayers. From this search, the transition metal dichalcogenides (TMDCs) [2, 3] and phosphorene arose. [4, 5] Compared to graphene, an important advantage of these new materials is the fact that they have an intrinsic energy gap in their band structures, which is essential for the future application of these materials in electronic devices, such as transistors and diodes.

TMDCs are composed by a transition metal M and two chalcogenides X , generally represented by MX_2 . Each monolayer has two hexagonal planes of X atoms and one hexagonal plane of M atoms as seen in Fig. 1.1. Common examples are MoS_2 , $MoSe_2$, WS_2 , and WSe_2 . Even before the discovery of monolayer versions of such materials, they attracted attention to a rich variety of phenomena, including superconductivity, semi-conductivity, etc. [6] However, concerning to the optical properties, MoS_2 monolayer, for example, demonstrates higher photoluminescence compared to few-layers or bulk due to the direct gap in the band structure as represented in Fig. 1.2. That direct band gap is located at the K points of the 2D hexagonal Brillouin zone and lays in the visible frequency range, which favors optoelectronics applications.

On the other hand, black phosphorus, the most stable allotrope of phosphorus, has attracted interest because it has a two-dimensional form called phosphorene composed of a single element (as well as graphene), with a peculiar property, compared to the TMDCs: its band structure exhibits a strong anisotropy, both for the valence band as well as for the conduction band. This can be seen when we compare the bands curvatures in the Γ to X and Γ to Y directions in Fig. 1.3. Such anisotropy is due to its puckered honeycomb structure which yields two inequivalent directions within the lattice, presented in Fig. 1.4, and it is reflected in unusual electronic, optical and transport properties. Also in contrast

Figure 1.1: Side and top view of MX_2 .Figure 1.2: From left to right: DFT calculations of the band structure of single layer, bilayer and bulk MoS_2 in the LDA (thin dashed lines) and in the G_0W_0 approximation. [7]

with TMDC, the band gap value is highly tunable, however it remains direct at the Γ point of the Brillouin zone independent of the number of layers.

Recently, new studies have demonstrated anisotropic optical properties also in TMDCs such as rhenium disulfide (ReS_2) [8] whose reduced crystalline symmetry results in such properties from the bulk down to the limit of monolayer.

The two-dimensional characteristic of these materials suggests an intensification of the Coulomb interaction between electrons and holes, or between charge carriers and impurities. In fact, excitons binding energies (electron-hole pairs) in two-dimensional lamellar materials are found experimentally, for example, of the order of 0.32 eV, and 0.4 eV, for WS_2 and black phosphorus monolayers, respectively. [5, 9] A strong electron-hole interaction gives the possibility of observing excited states of excitons, which follow an unusual non-hydrogenic Rydberg series. [9] In addition, the energies of trions (excitons charged with an extra electron or hole) and biexcitons (pairs of excitons) of the order of tens of meV [10, 11, 12, 13] are found experimentally, which is unprecedented in either bulk semiconductors or III-V and II-VI semiconductor heterostructures, and finds parallel only in carbon nanotubes and some layered perovskites in the semiconductor physics literature.

High binding energies stabilize excitons and trions despite thermic fluctuations and

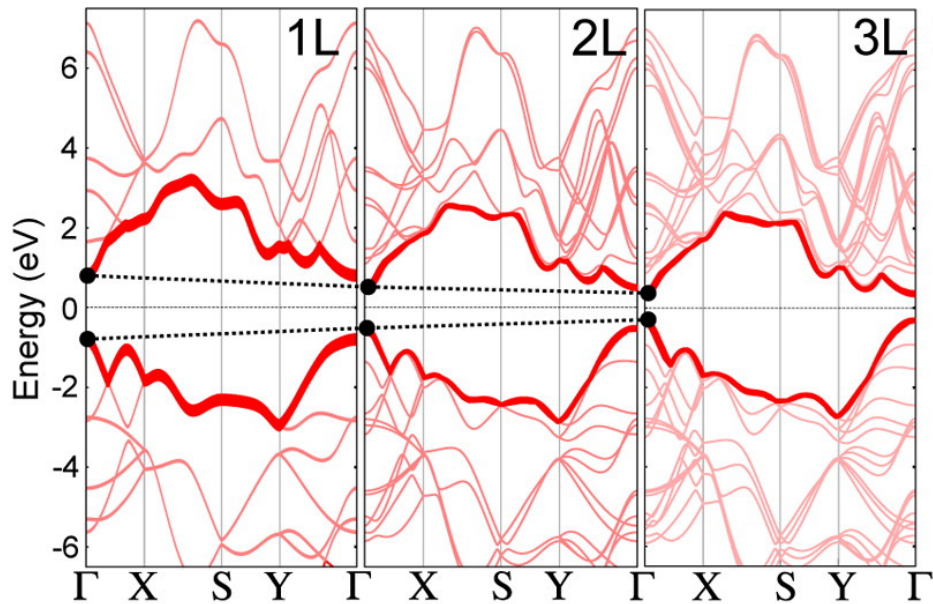


Figure 1.3: From left to right: DFT calculations of the band structure of single layer, bilayer and trilayer BP. [5]

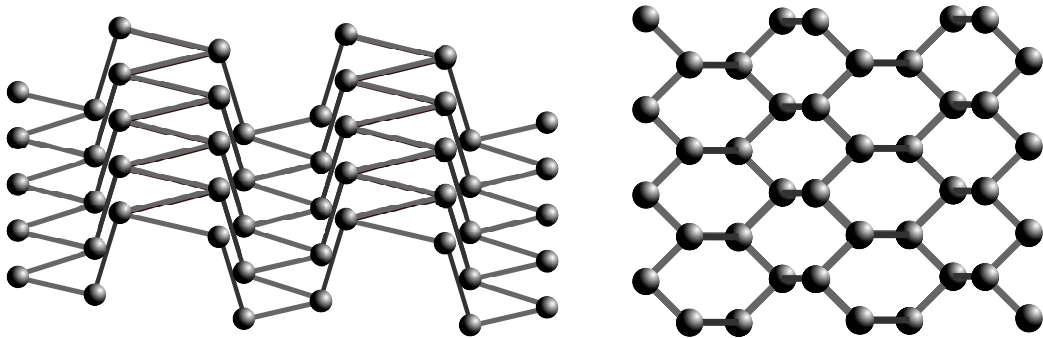


Figure 1.4: Side and top view of phosphorene.

increase the lifetime of these quasi-particles, making future applications possible in light transport by trions and in quantum computers with optical operation. The need to understand the dependence of these excitonic interactions as well as the interaction between light and these materials on the number of layers, dielectric medium, stacking order, etc., is necessary at the moment for these types of materials.

From the technological point of view, recent studies have suggested these materials as the basis for future electronic and optoelectronics devices, including field-effect transistors (FET) [4] and sensors (for a review on the subject, see [14]). As an example, the potential application of a WSe_2 monolayer acting as a p-n junction diode in efficient solar cells was recently demonstrated [15]. Possible applications of TMDCs as photodetectors were also demonstrated experimentally in Refs. [16, 17], and theoretical predictions have indicated potential applications in spintronics and valleytronics. [18]

Current advanced experimental techniques have allowed even the manufacture of compounds formed by the stacking of layers of different lamellar materials, which have been

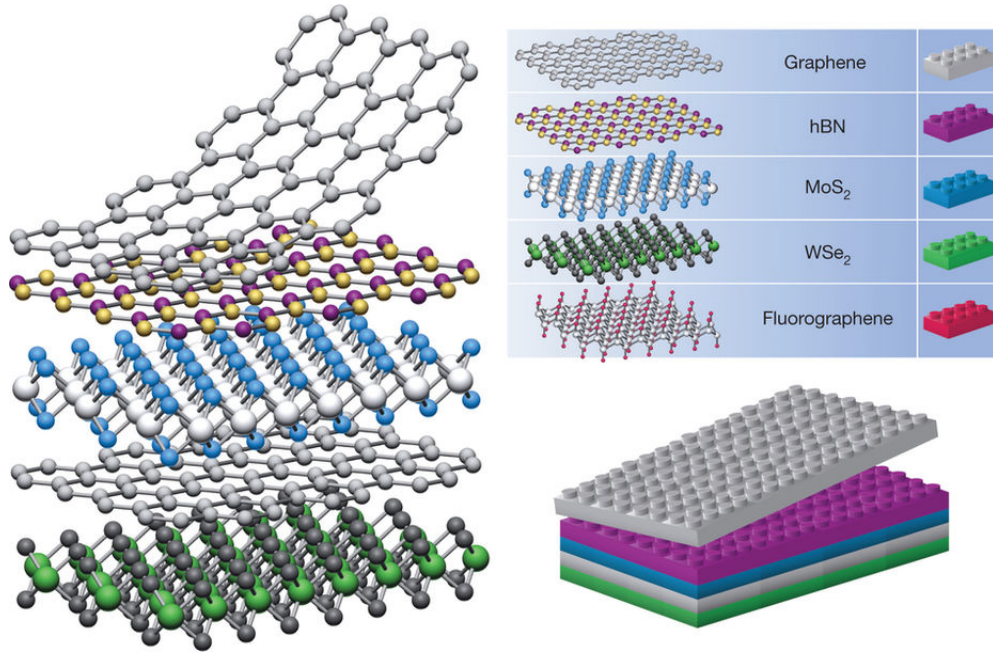


Figure 1.5: Building van der Waals heterostructures. If one considers 2D crystals to be analogous to Lego blocks (right panel), the construction of a huge variety of layered structures becomes possible. [19]

called "van der Waals heterostructures" [19], illustrated in Fig. 1.5. Artificially created van der Waals (vdW) heterostructures composed of stacked two-dimensional (2D) crystals have opened new possibilities for designing complex layered materials with chemical compositions and electronic properties sharply defined on a sub-nanometer length scale. A number of novel materials, devices, and physical phenomena based on this concept have already been demonstrated. These include light emitting diodes in band structure engineered hBN/graphene/MoS₂ structures [20], ultrafast photo detectors made of few-layer WSe₂ stacks [21], atomically thin solar cells based on MoS₂/WSe₂ heterobilayers [16], vertical tunneling transistors [22, 23], atomically thin quantum wells of stacked MoS₂ with infrared light emission [24], Mott insulating and unconventional superconducting states in twisted bilayer graphene [25, 26], and much more. In addition, encapsulation in atomically flat hBN has become a standard method to improve the electronic properties of active 2D layers by minimizing interactions with the environment [27]. Hence, the electronic properties and observed physical phenomena in these materials can differ from those found in their isolated components. With that, a recent experimental work has demonstrated the existence of an extra peak in the photoluminescence of a MoSe₂/WSe₂ heterostructure [28], which was assigned to an indirect exciton, that is, an electron-hole pair separated spatially by the junction. Several experimental works have been done recently in search of this type of exciton, which would allow a much longer recombination time (due to the spatial separation) and, with this, the detection of interesting phenomena as Bose-Einstein condensation of excitons. [29]

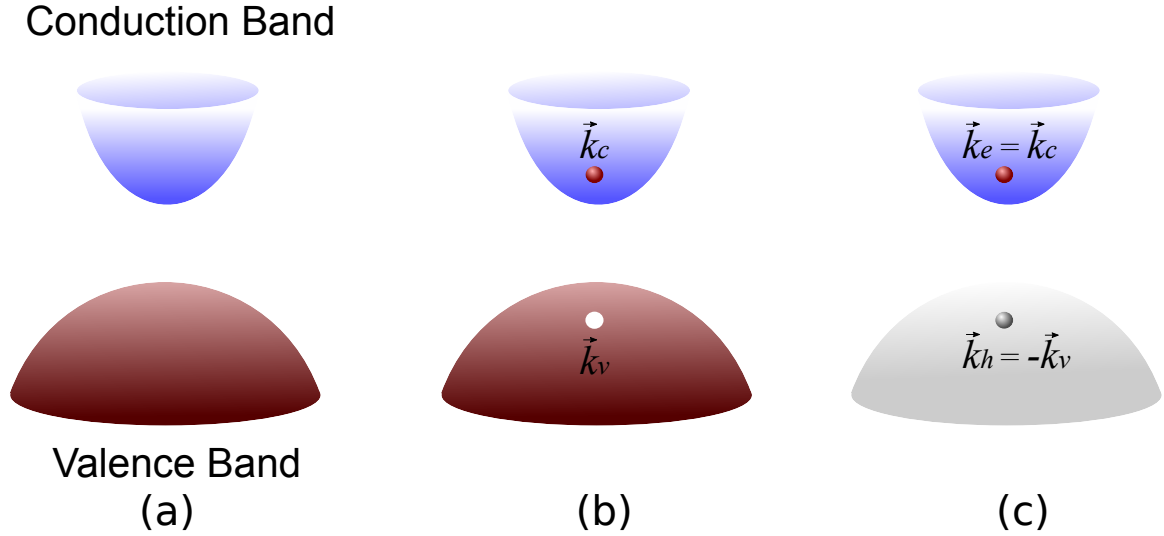


Figure 1.6: (a) In semiconductor crystals, the upper full band is called valence band and the lowest empty one is called conduction band. (b) An electron is removed from valence and placed at conduction band leaving an empty state. (c) The valence band states behave as a particle with positive charge called hole that has momentum with opposite sign. Adapted Fig. from Ref.[30]

1.2 Exciton

Firstly, in order to investigate interactions of electrons with other particles in many body systems, it can be useful to simplify the problem by comparing it to a quasi-particle that has the same charge as an electron but with a different mass. Such mass contains all the information of interactions in the former problem and, in that way, can be treated as a free particle (for a complete discussion about the effective mass model please refer to appendix A). In general, it is possible to approximate the system energy band extrema to quadratic functions, and the effective electron mass is related to the inverse of the band curvature.

In semiconductor crystals, the electronic states form bands due to lattice periodicity according to Bloch theorem. Such bands can be completely full or empty in the ground state. The upper full band is called valence band, where the highest level is called Fermi level; and the lowest empty band is called conduction band. When crystals are excited with energies greater than the gap between valence and conduction, their excited electronic states are formed by removing one electron from a state below Fermi level and placing it in a state above as we can see in Fig 1.6.

So the concept of hole consists of replacing the full valence band that has an empty electronic state with a "anti-particle" called hole. Since the hole represents the removal of an electron from a band it must reduce energy which can be represented by a negative energy. Also, the total momentum of a full band is equal to zero due to the geometrical symmetry of the Brillouin zone. In that way, this "anti-particle" has the opposite momentum of the missing electron, $\mathbf{k}_v = -\mathbf{k}_h$, considering $\hbar = 1$, which gives

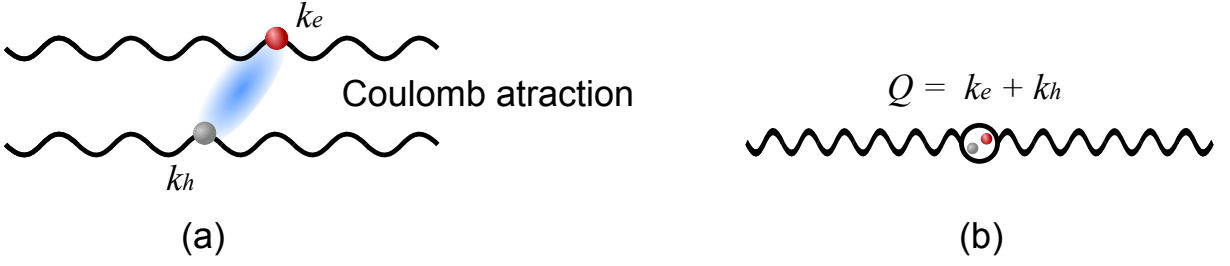


Figure 1.7: (a) Free electron in the conduction band \mathbf{k}_e interacts with a free valence hole \mathbf{k}_h via attractive Coulomb processes. (b) Bound state with momentum $\mathbf{Q} = \mathbf{k}_e + \mathbf{k}_h$ called Exciton. Adapted Fig. from [30]

$$E_h = -E_v = -\frac{\mathbf{k}_v^2}{2m_v} = \frac{\mathbf{k}_h^2}{2m_h}, \quad (1.1)$$

where the hole effective mass has the opposite sign of the electron in the valence band. In the valence extreme, the band curvature is negative, hence the effective mass is negative, which results in a positive hole mass.

Another important hole characteristic is the mean velocity. The mean velocity of an electron in a Bloch level n is given by [31]

$$\mathbf{v}_e = \frac{1}{\hbar} \frac{\partial E_n(\mathbf{k})}{\partial \mathbf{k}}, \quad (1.2)$$

consequently the hole velocity given by the necessary substitutions ($\mathbf{k}_v = -\mathbf{k}_h$ and $E_v = -E_h$) follows the relation $\mathbf{v}_e = \mathbf{v}_h$.

These properties applied to the following electron equation of motion end up with one of a positively charged particle.

$$\hbar \frac{d\mathbf{k}_e}{dt} = -e \left(\mathbf{E} + \frac{1}{c} \mathbf{v}_e \times \mathbf{B} \right) \quad \begin{matrix} \mathbf{k}_h = -\mathbf{k}_e \\ \mathbf{v}_h = \mathbf{v}_e \end{matrix} \rightarrow \hbar \frac{d\mathbf{k}_h}{dt} = e \left(\mathbf{E} + \frac{1}{c} \mathbf{v}_h \times \mathbf{B} \right) \quad (1.3)$$

As we can see, excitations in semiconductor have a hydrogen type of structure where the electron in the conduction band interacts with the valence hole via attractive Coulomb processes. The localization of the electron close to the hole forms a quasi-particle called *exciton* with momentum $\mathbf{Q} = \mathbf{k}_e + \mathbf{k}_h$ as represented in Fig 1.7.

If this excitation pair is tightly bound being localized in a single ion, it is called a *Frenkel exciton*[32]. As any atom in a perfect crystal has the same probability of being excited, the exciton can hop from one atom to the other forming a propagating wave. It is likely to be found in materials that have small dielectric constants which allows stronger interactions. For example, solid rare gases have excitons that are of this type. On the other hand, *Wannier-Mott excitons*[33] are weakly bound whose radius of interaction is in the order of several lattice constants. They are commonly found in semiconductors that have a higher dielectric constant. Experiments in Cu_2O [34, 35, 36] demonstrated that this type of exciton has a hydrogen-like spectrum due to the possibility of fitting the exciton levels, found through the optical absorption, with a Rydberg equation. The

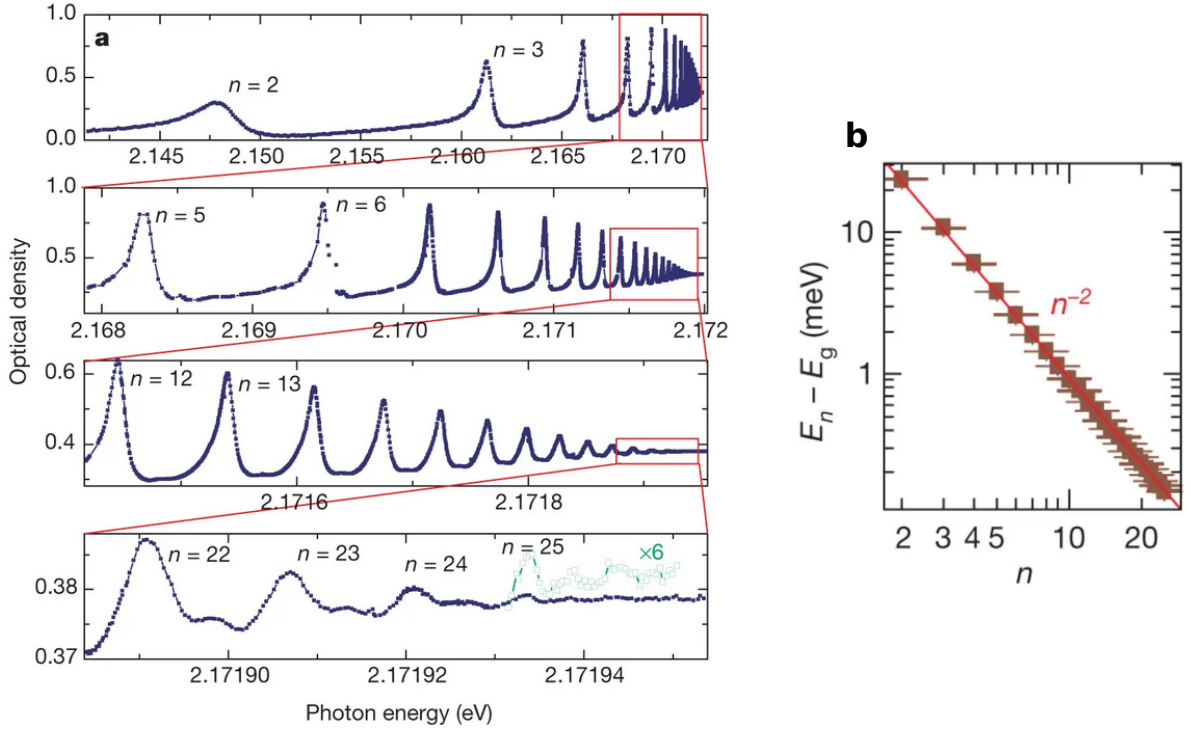


Figure 1.8: (a) Cu_2O spectra measured with a single-frequency laser. Peaks are related to the principal quantum number n . The inferior panels show the close-up for higher values of n . (b) Exciton binding energies with dependence of n . The energies follow the Rydberg formula as they are fitted with a n^{-2} dependency.[36]

absorption spectra of this material is presented in Fig. 1.8(a). It shows the exciton peaks related to the principal quantum number n with great precision up to 25 which can be seen in the close-ups in the lower panels. In Fig. 1.8(b), the exciton binding energies are fitted to a function with n^{-2} dependency which demonstrates the validity of the Rydberg formula in this type of exciton. With the hydrogen analogy in mind, we define the exciton energy and radius for a bulk semiconductor

$$E_X(n) = -\frac{\mu}{m_0\epsilon^2} Ry \cdot \frac{1}{n^2} \equiv -\frac{R_X}{n^2}, \quad (1.4)$$

$$r_X(n) = \left(\frac{m_0\epsilon a_0}{\mu} \right) \equiv a_X n^2, \quad (1.5)$$

where μ is the exciton reduced mass ($1/\mu = 1/m_e + 1/m_h$), m_0 is the free electron mass, ϵ is the dielectric constant, Ry is the Rydberg constant of energy and a_0 is the Bohr radius.

Only poorly localized excitons can be described within the parabolic approximation of the effective mass model. The reason is that due to the uncertainty principle, they can be described with a small region of the Brillouin which can be generally approximated to a parabola. In contrast, highly localized particles need a large range of the Brillouin zone to be described which does not have in general a parabolic approximation. Thus, this thesis will focus on the Wannier-Mott type of exciton.

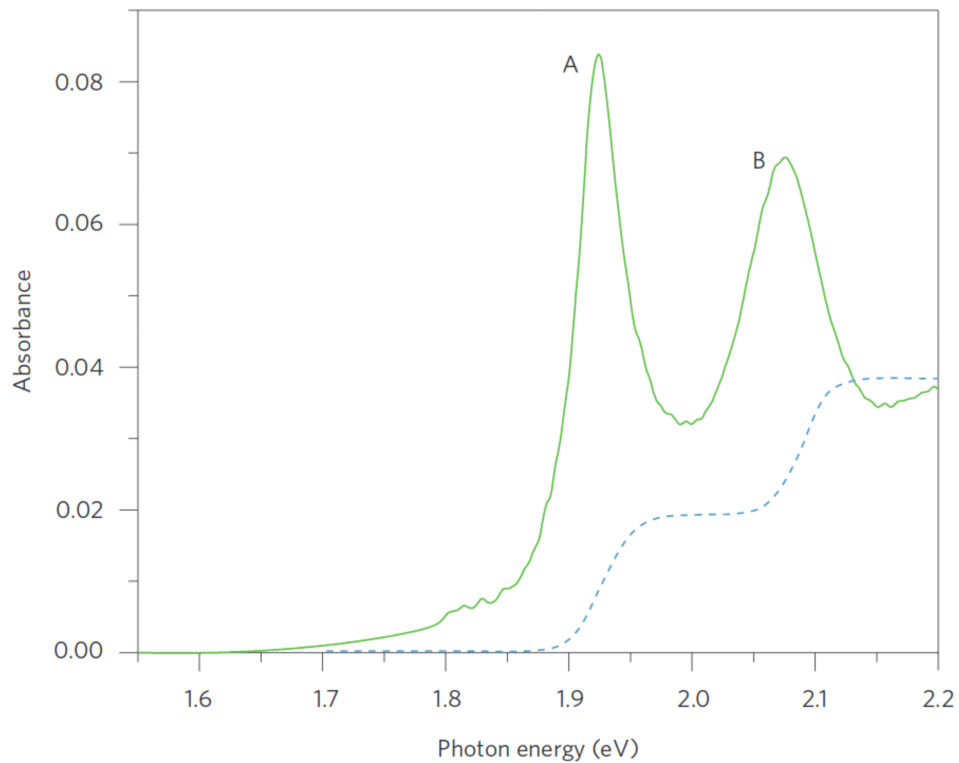


Figure 1.9: Absorption spectrum of monolayer MoS_2 at 10 K (solid green line) [38]. A and B are exciton resonances corresponding to transitions from the two spin-split valence bands to the conduction bands. The blue dashed line shows the absorbance (arbitrary units) if excitonic effects were absent. The inset illustrates the possible transitions considering spin orbit coupling, forming bound excitons. Adapted Fig. from [37].

In order to understand the role played by excitons in the optoelectronic properties of bidimensional systems, we can refer to the experimental result [37] represented in Fig. 1.9. In this case, the absorption spectrum of a monolayer of MoS_2 is calculated. As seen in the green solid line, there are two absorption peaks A and B which are excitonic resonances related to two transitions from valence band to conduction band considering spin orbit coupling. In contrast, the blue dashed line represents a numerical result derived from an energy-independent density-of-states and parabolic band approximation where we obtain only a step absorption spectrum as excitonic effects are not considered.

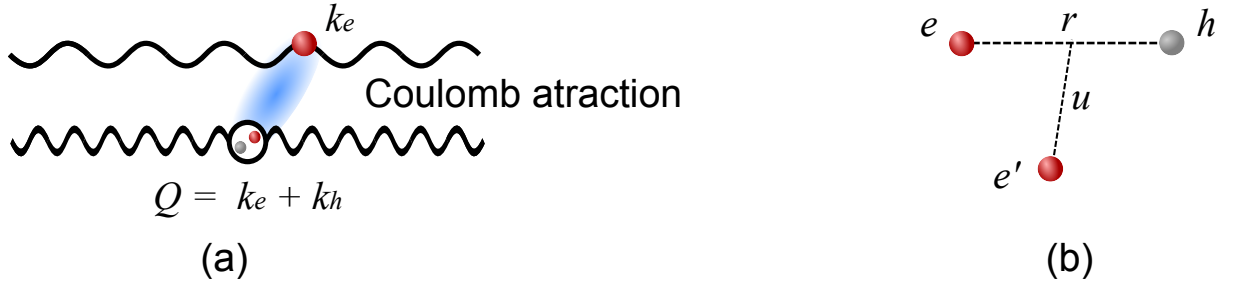


Figure 1.10: (a) Free electron in the conduction band \mathbf{k}_e interacts with an exciton $\mathbf{Q} = \mathbf{k}_e + \mathbf{k}_h$ via attractive Coulomb processes. (b) Set of relevant coordinates for the relative motion of an χ^- trion.

1.3 Trion

Trions are quasiparticles that describe the interaction of excitons with electrons or holes. A negatively charged exciton (χ^-) is composed of two electrons of mass m_e located at r_e and $r_{e'}$, and a hole of mass m_h located at r_h as illustrated in Fig. 1.10. In the other hand, χ^+ is composed of two holes and a single electron.

These quasiparticles are useful in the study of doped systems whose optoelectronic properties are dominated by the effects of charged excitons. This can be inferred from the experimental result [38] presented in Fig. 1.11 where the absorption spectrum of a MoS₂ monolayer is calculated considering the effect of an electric field. As the electric field increases from -80 V, which corresponds to the undoped system, due to substrate interactions and layer defects, to 70 V with a doping density of 10^3 cm^{-2} , we can see that the absorption peak A that is related to excitonic resonances becomes suppressed and a new peak A⁻ dominates the spectrum. This new feature can be understood as the role played by trions in the absorption spectrum as the charge carrier density increases and excitons become charged. Similarly, the photoluminescence spectra show the decrease in the excitonic peak A due to the increase of doping in the system.

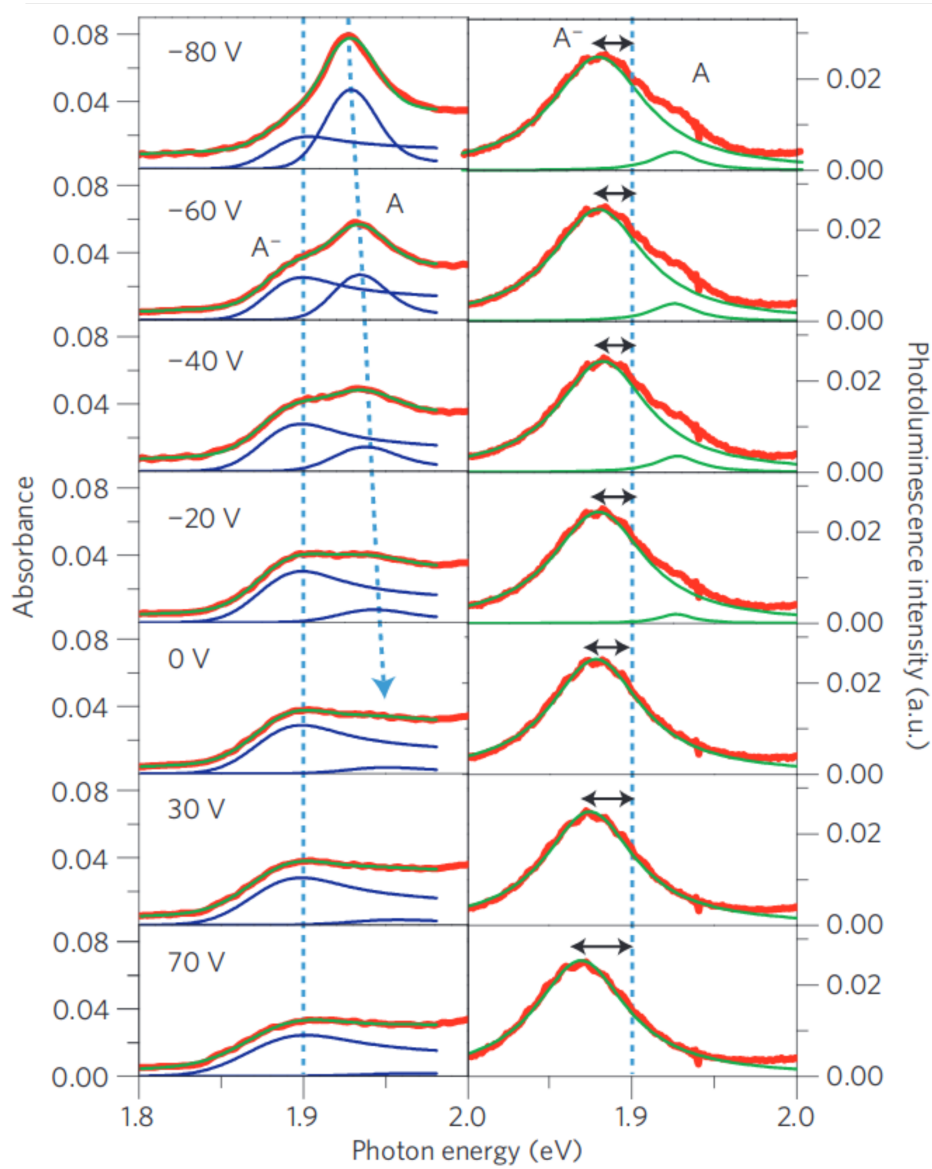


Figure 1.11: Absorption and photoluminescence spectra (red lines) in the range of 1.8 - 2.0 eV for the indicated back-gate voltages. The exciton (A) and trion (A^-) resonances behave differently with gate voltage. Left: Absorption spectra, with the dashed blue lines as a guide to the eye for the threshold energies of A and A^- features. The green lines are power-law fits to the experimental results with the A and A^- components shown as the blue lines. Right: The photoluminescence spectra of the A and A^- features are fit to Lorentzians (green lines). The dashed blue line indicates the absorption peak of the A^- resonance and the arrows show the doping-dependent Stokes shift of the trion photoluminescence.[38]

1.4 Plasmon

Collective excitations of the electron gas, plasma, are called *plasmons*. In a classical view, plasmons are collective oscillations of electronic density. When plasmons are coupled to an external electromagnetic field produced by a light source, photons, they are called *plasmon-polaritons*. These quasiparticles play an important role in the optoelectronic properties of doped semiconductors as they describe the screening effect of free electrons in the conduction band due to an applied electric field of light. In that case, the electrons move to the opposite direction of the electric field which creates an internal field that screens the external interaction. The electrons then respond to the external field through a collective oscillation. If the light frequency is greater than the plasma frequency, which is related to the Fermi energy, the electrons will be excited into electron-hole pairs damping the plasmon-polaritons.

In a dielectric material, the bound charges react to an applied electric field \mathbf{E} in the following way

$$\mathbf{D} = \epsilon_0 \mathbf{E} + \mathbf{P}, \quad (1.6)$$

where \mathbf{D} is electric displacement field, ϵ_0 , the vacuum permittivity, and \mathbf{P} , the polarization density. In the case of a linear response of the polarization in respect to the electric field ($\mathbf{P} = \epsilon_0 \chi \mathbf{E}$), we obtain

$$\mathbf{D} = \epsilon_0(1 + \chi) \mathbf{E} = \epsilon \mathbf{E}, \quad (1.7)$$

in which χ is the electric susceptibility, or density response function, and ϵ is the dielectric function. So, in order to obtain the plasma oscillation eigenmodes (plasmons), we have that the conduction electrons in the material screen \mathbf{E} making the effective electric field inside the dielectric to be equal to zero. As \mathbf{E} is non-trivial, the only solution to Eq. 1.7 is ¹

$$\epsilon(\mathbf{q}, \omega) = 0, \quad (1.8)$$

which dependence in the momentum and frequency were made explicit.

Now, lets calculate the dielectric function of a electron plasma considering many body interactions. We start with the single particle hamiltonian

$$H = \sum_{\mathbf{k}} E_k a_{\mathbf{k}}^\dagger a_{\mathbf{k}} + \sum_{\mathbf{p}} V_{eff}(p) \sum_{\mathbf{k}} E_k a_{\mathbf{k}+\mathbf{p}}^\dagger a_{\mathbf{k}}, \quad (1.9)$$

¹Another way to reach this solution comes from the Maxwell's equations. We can write a vector equation for the electric field as $\frac{\omega^2}{c^2} \epsilon(\mathbf{q}, \omega) \mathbf{E}(\mathbf{q}, \omega) = \mathbf{k}[\mathbf{k} \cdot \mathbf{E}(\mathbf{q}, \omega)] - k^2 \mathbf{E}(\mathbf{q}, \omega)$. So, for longitudinal modes, we find the same result as in Eq. 1.8.

where the effective interaction is given by the sum of the Coulomb potential of a test charge and the induced potential of the screened particles

$$V_{eff}(p) = V_p + V_{ind}(p). \quad (1.10)$$

With that, the equation of motion for the density charge operator ($\hat{\rho}_{e,\mathbf{q}} = -\frac{|e|}{L^3} \sum_{\mathbf{k}} a_{\mathbf{k}-\mathbf{q}}^\dagger a_{\mathbf{k}}$) is derived

$$\begin{aligned} \frac{d}{dt} a_{\mathbf{k}-\mathbf{q}}^\dagger a_{\mathbf{k}} &= \frac{i}{\hbar} \left[H, a_{\mathbf{k}-\mathbf{q}}^\dagger a_{\mathbf{k}} \right] \\ &= i(E_{k-q} - E_k) a_{\mathbf{k}-\mathbf{q}}^\dagger a_{\mathbf{k}} \\ &\quad - \frac{i}{\hbar} \sum_{\mathbf{p}} V_{eff}(p) (a_{\mathbf{k}-\mathbf{q}}^\dagger a_{\mathbf{k}-\mathbf{p}} - a_{\mathbf{k}+\mathbf{p}-\mathbf{q}}^\dagger a_{\mathbf{k}}). \end{aligned} \quad (1.11)$$

Through the random phase approximation, we choose a specific combination of wave numbers which in this case is $\mathbf{p} = \mathbf{q}$ and ignore all other contributions. This approximation yields the following equation taking the expectation value

$$\frac{d}{dt} \langle a_{\mathbf{k}-\mathbf{q}}^\dagger a_{\mathbf{k}} \rangle = i(E_{k-q} - E_k) \langle a_{\mathbf{k}-\mathbf{q}}^\dagger a_{\mathbf{k}} \rangle - \frac{iV_{eff}(q)}{\hbar} (f_{\mathbf{k}-\mathbf{q}} - f_{\mathbf{k}}), \quad (1.12)$$

in which $\langle a_{\mathbf{k}}^\dagger a_{\mathbf{k}} \rangle = f_{\mathbf{k}}$.

Considering that the test charge depends on time as $\exp(-i(\omega + i\delta)t)$, we obtain

$$\hbar(\omega + i\delta + E_{k-q} - E_k) \langle a_{\mathbf{k}-\mathbf{q}}^\dagger a_{\mathbf{k}} \rangle = V_{eff}(q) (f_{\mathbf{k}-\mathbf{q}} - f_{\mathbf{k}}), \quad (1.13)$$

therefore

$$\langle \rho_q \rangle = -\frac{|e|}{L^3} V_{eff}(q) P(q, \omega), \quad (1.14)$$

where the polarization functions is

$$P(q, \omega) = \sum_{\mathbf{k}} \frac{f_{\mathbf{k}-\mathbf{q}} - f_{\mathbf{k}}}{\hbar(\omega + i\delta + E_{k-q} - E_k)}. \quad (1.15)$$

Finally, taking in consideration the definition for the potential of the screened particles

$$\begin{aligned} V_{ind}(q) &= -\frac{4\pi|e|}{\epsilon_0 q^2} \rho_q = \frac{4\pi e^2}{\epsilon_0 q^2 L^3} V_{eff}(q) P(q, \omega) \\ &= V_q V_{eff}(q) P(q, \omega), \end{aligned} \quad (1.16)$$

and Eq. 1.10, we obtain

$$V_{eff}(q) = \frac{V_q}{[1 - V_{eff}(q) P(q, \omega)]} = \frac{V_q}{\epsilon(q, \omega)}. \quad (1.17)$$

Thus, the dynamic dielectric function is given by

$$\epsilon(q, \omega) = 1 - V_q \sum_{\mathbf{k}} \frac{f_{\mathbf{k}-\mathbf{q}} - f_{\mathbf{k}}}{\hbar(\omega + i\delta + E_{\mathbf{k}-\mathbf{q}} - E_{\mathbf{k}})}, \quad (1.18)$$

which is known as the *Lindhard* formula. This formula was derived for 3D but is also valid for 2D. To fully understand the Lindhard result, it is important to investigate some limiting cases of the dynamic dielectric function. For the purpose of this thesis, we shall analyse the long wave-length limit ($q \rightarrow 0$) for a 2D system. The two needed approximations

$$E_{\mathbf{k}-\mathbf{q}} - E_{\mathbf{k}} = \frac{\hbar^2}{2m}(k^2 - 2\mathbf{k} \cdot \mathbf{q} + q^2) - \frac{\hbar^2 k^2}{2m} \simeq -\frac{\hbar^2 \mathbf{k} \cdot \mathbf{q}}{m}, \quad (1.19)$$

and

$$f_{\mathbf{k}-\mathbf{q}} - f_{\mathbf{k}} = f_{\mathbf{k}} - \mathbf{q} \cdot \nabla_{\mathbf{k}} f_{\mathbf{k}} + \dots - f_{\mathbf{k}} \simeq -\mathbf{q} \cdot \nabla_{\mathbf{k}} f_{\mathbf{k}}, \quad (1.20)$$

applied to Eq. 1.18 yield

$$\begin{aligned} \epsilon(q \rightarrow 0, \omega) &\simeq 1 - V_q \sum_{\mathbf{k}, i} \frac{q_i \frac{\partial f}{\partial k_i}}{\hbar\omega - \hbar^2 \mathbf{k} \cdot \mathbf{q}/m} \\ &\simeq 1 - \frac{V_q}{\hbar\omega} \sum_{\mathbf{k}, i} q_i \frac{\partial f}{\partial k_i} \left(1 + \frac{\hbar \mathbf{k} \cdot \mathbf{q}}{m\omega} \right). \end{aligned} \quad (1.21)$$

The first term inside the parenthesis vanishes after the summation since it is proportional to the Fermi-Dirac distribution when $k \rightarrow \infty$. So, considering a factor of 2 due to the spin, we have

$$\epsilon(q \rightarrow 0, \omega) \simeq 1 - V_q \frac{L^2}{m\omega^2} 2 \int \frac{d^2 k}{(2\pi)^2} \sum_{i,j} q_i q_j k_j \frac{\partial f_{\mathbf{k}}}{\partial k_i}, \quad (1.22)$$

that can be solved with the following partial integration

$$2 \int \frac{d^2 k}{(2\pi)^2} k_j \frac{\partial f_{\mathbf{k}}}{\partial k_i} = -2 \int \frac{d^2 k}{(2\pi)^2} f_{\mathbf{k}} \frac{\partial k_k}{\partial k_i} = -n \delta_{ij}. \quad (1.23)$$

Hence, using the definition of the Coulomb interaction in 2D $V_q = 2\pi/\epsilon_0 q$, the result is

$$\epsilon(q \rightarrow 0, \omega) = 1 - \frac{\omega_{pl}^2(q)}{\omega^2}, \quad (1.24)$$

where $\omega_{pl}^2(q)$ is the 2D plasma frequency given by

$$\omega_{pl}(q) = \sqrt{\frac{2\pi e^2 n}{\epsilon_0 m} q}. \quad (1.25)$$

Hence, the plasmon energy in the long wave-length limit has a squared root dependence to the momentum. However, if we consider that this system interacts with another electron gas, or in the case of two interacting semiconductor layers, then another important feature arises. Charges of opposite sign will be induced in the two plasma whose densities will oscillate with two distinct fashions: in phase and out of phase. These correspond respectively to two plasmon modes that are called *optical* (higher frequency) and *acoustic* (lower frequency) which will result in two branches in the dispersion relation with the following trends [39]

$$\omega_{pl}^{op}(q) \propto \sqrt{q}, \quad \omega_{pl}^{ac}(q) \propto q. \quad (1.26)$$

A common way to probe the optoelectronics properties of the materials with the dispersion and damping of plasmons is by the determination of the *loss function* which is defined as follows

$$\mathcal{L} = -\text{Im}\{\epsilon^{-1}(q, w)\}, \quad (1.27)$$

whose peaks correspond to the poles of $\epsilon^{-1}(q, w)$ describing the plasmons accordingly to Eq. 1.8.

1.5 Scope of the thesis

In the following chapters, we apply the concepts introduced here in the study of excitonic complexes and plasmonic effects in two-dimensional vdW heterostructures. In chapter 2, we focus on the effect of dielectric screening on electron-hole interactions in vdW heterostructures investigating the solution of Poisson's equation for the system slabs. We verify the results found in this chapter through various comparisons with the literature which include an *ab initio* method called Quantum Electrostatic Heterostructure (QEH). In chapter 3, with the intent of describing excitons and plasmons more realistically, we extend the QEH method by including the contribution from infrared active phonons of the 2D layers to the dielectric function. Moreover, we make possible to include screening from bulk substrates and intraband transitions from free carriers in doped semiconducting layers. In chapter 4, we employ the QEH method to investigate the doping effect of MoSSe Janus layers, caused by the intrinsic electric dipole, on graphene plasmons. We study the limits of plasmon energies without the need of any external sources and the possibility of quenching certain modes. Furthermore, we address the expected improvements of choosing other Janus TMDs. In chapter 5, we do a theoretical study of the effect of an external in-plane field on charged exciton states. We obtain polarizabilities of excitons from the parabolicity of numerically calculated Stark shifts. Also, we investigate the possibility of a hyperpolarizability of trions in 2D materials. Finally, in Chapter 6, we summarize our findings and provide our concluding remarks.

Electrostatics of electron-hole interactions in van der Waals heterostructures

2.1 Motivation

The physics of excitons and other electron-hole complexes in atomically thin materials [37, 40, 41, 42, 43, 44] has attracted great attention in the past few years, in part due to the high electron-hole binding energies observed in these systems, which are approximately ten times higher than those of conventional semiconductors, such as III-V and II-VI compounds, even when the latter are structured in quantum dots, wires or wells. [43, 45, 46, 47] Excitons in 2D materials are strongly confined to a plane, so that the screening from their surrounding dielectric environment is reduced, thus increasing the exciton binding energies. [9, 48] Excitonic Rydberg spectra of WS₂ [9] and WSe₂ [49] have been measured in recent absorption experiments, where one can verify up to 3 excited states. These series, however, differ from that expected for a hydrogen-like electron-hole pair. Two-photon absorption measurements have also been used to investigate excitonic states with *p*-symmetry, where a slight degeneracy break with respect to *s*-states is expected.[49] These features suggest that the electron-hole interaction potential in this system is not Coulombic: indeed, due to the lack of screening by the environment above the material layer, the interaction is expected to acquire a different form, as discussed decades ago [50, 51] in the context of thin semiconductor films.

The effective electron-hole interaction potential is straightforwardly found by analytically solving the Poisson equation for a dielectric slab surrounded by two media with different dielectric constants. This approach clearly provides a fully classical electrostatic description of the problem. It is far from guaranteed, however, that such a classical approach provides reasonable results in the limit of atomically thin materials, where quantum and dynamical effects may be sizeable. Using a classical effective potential to calculate exciton eigenenergies leads to a reasonable agreement between theory and experiment,[9] but only if additional screening due to the SiO₂ substrate in the experiment is taken into account. A more recently developed approach, [52, 53, 54] involving quantum mechanical effects via ab initio calculations, is expected to provide better agreement in few layer

cases, which has been confirmed by comparison to the same experimental results of Ref. [9]. In this approach, known as the quantum electrostatic heterostructure (QEH) model, as well as the simple classical effective potential approach, the main effects of the environment on the electron-hole interactions are all included in the form of a static ($\omega = 0$) dielectric function. Dielectric functions for both approaches match for low wave vectors, but strongly disagree as k increases, thus suggesting the QEH model captures important contributions to the dielectric function which are not captured by the simple classical effective model.

It is important to point out that despite the limitations of classical effective potential approaches [50, 51] for describing atomically thin materials, they are a physical and efficient way of obtaining the electron-hole potential in the limit of a large number of layers. It is thus worthwhile to investigate how this approach compares to the QEH model as the number of layers increases, in order to obtain a deeper understanding of the limitations of this simple approach. In the same spirit, it is important to compare both approximations for the case where substrate screening is important, as well as in the presence of layers of different materials, i.e. in van der Waals heterostructures. [19]

In this chapter, we explore the effective electron-hole interaction potential, suitable for charged particles in a N -layer vdW stack. This is accomplished by solving the Poisson equation for the potential experienced by a charged particle in a given layer due to a test charge placed in the same or any other layer. We demonstrate that such a classical electrostatic approach provides a very fast and computationally efficient means of achieving results which are surprisingly accurate when compared to those obtained from more sophisticated and expensive approaches based on ab initio calculations. Our results for the binding energy of inter-layer excitons in hetero-bilayers, as well as for intra-layer excitons in the presence of additional graphene capping layers, [55] are discussed in light of recently reported experimental PL and absorption data for these systems. In addition, a detailed comparison is made with the recently developed QEH approach. [52]

2.2 Theoretical framework

Theoretical approaches available in the literature for investigating electron-hole interactions in low dimensional systems surrounded by different dielectric media are usually based either on (i) classical electrostatics, where the interaction potential is obtained, e.g., by solving the Poisson equation for a stack of dielectric slabs, [50, 51] or (ii) via direct or parametrized first principles calculations, the latter of which forms the basis of the recently proposed quantum electrostatic heterostructure approach, [52] where the effective dielectric function of the vdW stack is obtained with the aid of ab initio-obtained density response functions of the separated layers that compose the heterostructure. In what follows, these two approaches are discussed in greater detail.

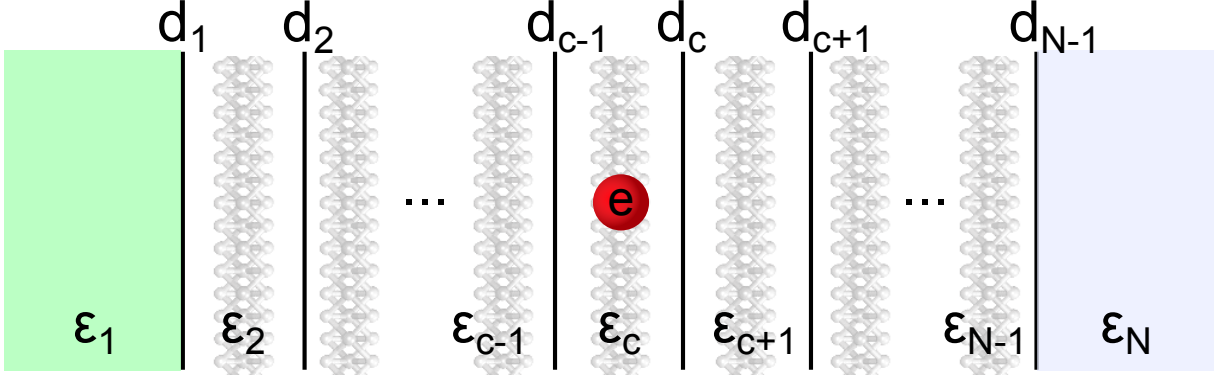


Figure 2.1: (Color online) Sketch of the series of interfaces between slabs with dielectric constants ε_n describing each material layer. The charge (e) placed at the c -th slab generates a screened Coulomb potential at each layer, that obeys the Poisson equation with a space-dependent dielectric constant.

2.2.1 Electrostatic transfer matrix method

Let us assume a series of N stacked layers along the z -direction, each with dielectric screening ε_n ($n = 1, 2, \dots, N$), separated by interfaces at $z = d_n$ ($n = 1, \dots, N - 1$), as sketched in Fig. 1. We take the origin as the center of the c -th layer, where the source charge is placed. Our aim is to calculate the potential at the t -th layer, where test charge is. For instance, spatially direct (indirect) excitons would have $c = t$ ($c \neq t$). For the n -th layer, the Poisson equation reads

$$\varepsilon_n^{\parallel} \nabla_{\rho, \theta}^2 \Phi_{n,c} + \varepsilon_n^{\perp} \frac{\partial^2 \Phi_{n,c}}{\partial z^2} = q_n, \quad (2.1)$$

where $q_n = -e\delta_{n,c}\delta(\vec{r})$ is the point charge at this layer (which is non-zero only at the c -th layer). The negative sign implies we are assuming the source charge to be an electron.

The solution for the electrostatic potential at any layer n is written in the form

$$\Phi_{n,c}(\rho, z) = \frac{e}{4\pi\varepsilon_c\varepsilon_0} \int_0^{\infty} \{J_0(k\rho) [A_n(k)e^{kz} + B_n(k)e^{-kz} + e^{-k|z|}\delta_{n,c}]\} dk. \quad (2.2)$$

The electron-hole interaction potential $V_{eh}^{t,c} = e\Phi_{t,c}$ is more conveniently re-written as

$$V_{eh}^{t,c}(\rho) = \frac{e^2}{4\pi\varepsilon_0} \int_0^{\infty} \frac{J_0(k\rho)}{\varepsilon_{t,c}(k)} dk, \quad (2.3)$$

where the effective dielectric screening function for a hole in the t -th layer, at a distance z_t from the point charge, is $\varepsilon_{t,c}(k) = \varepsilon_c [A_t(k)e^{kz_t} + B_t(k)e^{-kz_t} + \delta_{t,c}]^{-1}$. Notice that this expression covers both the direct ($z_t = 0$) and indirect exciton cases. We shall now look for a means of calculating $A_t(k)$ and $B_t(k)$.

Boundary conditions are imposed so that $B_1 \equiv 0$ and $A_N \equiv 0$, in order to avoid divergence as $z \rightarrow \pm\infty$. In addition, boundary conditions at each of the $N - 1$ interfaces require continuity of the potential and its derivative, thus leading to a system of $2(N - 1)$ equations. Alternatively, one can represent each pair of equations for each interface in a

matrix form

$$M_n \begin{pmatrix} A_{n+1} \\ B_{n+1} \end{pmatrix} = \bar{M}_n \begin{pmatrix} A_n \\ B_n \end{pmatrix} - \begin{pmatrix} e^{kd_{c-1}} \\ \varepsilon_c e^{kd_{c-1}} \end{pmatrix} \delta_{n,c-1} + \begin{pmatrix} e^{-kd_c} \\ -\varepsilon_c e^{-kd_c} \end{pmatrix} \delta_{n,c}, \quad (2.4)$$

where

$$\bar{M}_n = \begin{pmatrix} e^{kd_n} & e^{-kd_n} \\ \varepsilon_n e^{kd_n} & -\varepsilon_n e^{-kd_n} \end{pmatrix}, \quad M_n = \begin{pmatrix} e^{kd_n} & e^{-kd_n} \\ \varepsilon_{n+1} e^{kd_n} & -\varepsilon_{n+1} e^{-kd_n} \end{pmatrix}. \quad (2.5)$$

Combining all boundary conditions together yields

$$\begin{pmatrix} 0 \\ B_N \end{pmatrix} = \mathcal{M} \begin{pmatrix} A_1 \\ 0 \end{pmatrix} - \mathcal{M}' \begin{pmatrix} e^{kd_{c-1}} \\ \varepsilon_c e^{kd_{c-1}} \end{pmatrix} + \mathcal{M}'' \begin{pmatrix} e^{-kd_c} \\ -\varepsilon_c e^{-kd_c} \end{pmatrix}, \quad (2.6)$$

where $\mathcal{M} = M_{N-1}^{-1} \bar{M}_{N-1} \dots M_1^{-1} \bar{M}_1$, $\mathcal{M}' = M_{N-1}^{-1} \bar{M}_{N-1} \dots M_c^{-1} \bar{M}_c M_{c-1}^{-1}$, and $\mathcal{M}'' = M_{N-1}^{-1} \bar{M}_{N-1} \dots M_{c+1}^{-1} \bar{M}_{c+1} M_c^{-1}$ can be seen as electrostatic transfer matrices (ETM). This allows us to solve for A_1 as

$$A_1 = \frac{(\mathcal{M}'_{11} + \varepsilon_c \mathcal{M}'_{12}) e^{kd_{c-1}} - (\mathcal{M}''_{11} - \mathcal{M}''_{12} \varepsilon_c) e^{-kd_c}}{\mathcal{M}_{11}}. \quad (2.7)$$

Finally, once A_1 is obtained from the transfer matrices, $A_t(k)$ and $B_t(k)$ are calculated simply by applying the appropriate transfer matrices on $(A_1 \ 0)^T$, according to Eq. (2.4).

2.2.2 Quantum Electrostatic Heterostructure Model

For the sake of completeness, here we briefly discuss the Quantum Electrostatic Heterostructure model for calculating the effective dielectric function in vdW stacks. More details concerning the derivation of this method are found in Ref. [52].

The QEH model uses in-plane averaged density response functions $\chi_i(k, \omega)$ that are obtained from ab initio calculations for each of the materials composing a van der Waals stack of layers. With a Dyson-like equation that couples the building blocks together via the Coulomb interaction, it is possible to calculate a full density response function $\chi_{ia,jb}$ that gives the magnitude of the monopole (dipole) density induced in the i th layer by a constant (linear) potential applied in the j th layer. Hence, the inverse dielectric matrix is obtained as

$$\epsilon_{ia,jb}^{-1}(k, \omega) = \delta_{ia,jb} + \sum_{lc} V_{ia,lc}(k) \chi_{lc,jb}(k, \omega), \quad (2.8)$$

where indices i, j, l label the layers and $a, b, c = 0, 1$ correspond to monopole (0) and dipole (1) contributions. The Coulomb matrix is obtained from the potential $\Phi_{lc}(z, k)$ associated with the induced potential $\rho_{ia}(z, k)$, which is solution of a 1D Poisson equation, averaged over the thickness of the slab,

$$V_{ia,lc}(k) = \int \rho_{ia}(z, k) \Phi_{lc}(z, k) dz. \quad (2.9)$$

Finally, an inverse Fourier transform of the potential,

$$V(k) = \sum_{ia,jb,lc} \rho_{ia}^e(k) \epsilon_{ia,jb}(k)^{-1} V_{jb,lc}(k) \rho_{lc}^h(k), \quad (2.10)$$

results in the electron-hole potential in real space.

2.2.3 Wannier-Mott Model

Once the electron-hole potential is obtained from the methods described in the previous subsections, exciton eigenstates can be calculated within the Wannier-Mott model. [56] The exciton Hamiltonian in this approach is given by

$$H = -\frac{1}{\mu_{ij}} \nabla_{2D}^2 - V_{eh}^{t,c}(\vec{\rho}), \quad (2.11)$$

where $\mu_{ij} = (1/m_e^i + 1/m_h^j)^{-1}$ is the reduced effective mass of the electron-hole pair, with an electron (hole) confined in the i -th (j -th) layer, $\vec{\rho} = \vec{\rho}_e - \vec{\rho}_h$ is the relative coordinate, and the center-of-mass contribution to the kinetic energy is taken to be zero. $V_{eh}^{t,c}(\vec{\rho})$ is the in-plane electron-hole interaction potential, calculated either by the QEH or the ETM methods. Energies and spatial coordinates are written in units of the Rydberg energy R_y and the Bohr radius a_0 , respectively.

In the case of vdW heterostructures of transition metal dichalcogenides (TMDCs), which will be discussed in the following sections, the band offsets between the layers are finite, and thus the particles are able to tunnel between layers. Therefore, one should in principle consider, for each carrier, wave functions that are distributed across all layers, although with a much smaller probability in cases where band-offsets are large. The problem can then be treated as coupled quantum wells, described by a Hamiltonian matrix where the diagonal terms contain band offsets and in-plane potentials, whereas off-diagonal terms are hopping parameters. [57, 58, 59] However, for the sake of simplification, we will assume the off-diagonal contributions to be small and the problem is then approximated by electrons and holes completely confined in individual layers. This approximation is reasonable, as demonstrated by the fact that recent DFT calculations [57, 60, 61] for vdW heterostructures show that their band structures at K (where the direct gap takes place and, consequently, the exciton is expected to be) is not significantly different from a superposition of the bands of their composing monolayer materials. This suggests that a quasi-particle Hamiltonian matrix for conduction and valence bands could be simply described each by a 2×2 diagonal matrix, whose diagonal elements are just the monolayer bands, within a basis of completely layer-localized states. This situation supports the Hamiltonian in the form proposed in Eq. (2.11), which is then numerically diagonalized in order to provide the exciton binding energies shown in the following Sections.

It is worth to point out that a more accurate description of the excitonic properties of vdW heterostructures should take into account the effect of the stacking order and

even the relative inter-layer rotation on the band structure. [62, 63, 64] However, binding energies calculated in the following Section involve only electrons and holes in the vicinity of the K (K') point of the Brillouin zone, whereas recent experimental and theoretical papers [57, 65, 66, 67] systematically demonstrate that the electronic band structure of a MoS₂ bilayer around the K (K') does not significantly depend either on the stacking order or inter-layer twist. We thus assume, as an approximation, that these corrections are also negligible in the case of hetero-bilayers of TMDC investigated in what follows.

2.3 Results and discussion

2.3.1 Classical limits

Let us first investigate the limits of the effective dielectric functions of stacks of the same material, thus interpolating from the monolayer towards the bulk limit of a homogeneous system. An example is shown in Fig. 2.2(a), where results obtained by the QEH method for the macroscopic dielectric function [52] of MoS₂ with $N = 1, 3, 5, 10, 20, 30$, and 40 layers are illustrated. All curves exhibit a maximum ε_{max} , that increases with N until it converges to a fixed value, as shown by (red) squares in Fig. 2.2(b), left scale. A fitting function for this maximum, $F(N) = A + Be^{-N/n_1} + Ce^{-N/n_2}$ is shown as a (red) solid curve, with $A = 12.96\varepsilon_0$, $B = -4.13\varepsilon_0$, $C = -5.42\varepsilon_0$, $n_1 = 13.2$ and $n_2 = 1.9$. Despite such proposed exponential fitting being inspired only by the form of the numerically obtained curve, one can still obtain a physically meaningful parameter from it, namely A , which illustrates that for bulk MoS₂ (i.e. as $N \rightarrow \infty$), the maximum of the dielectric function approaches $\varepsilon \approx 12.96\varepsilon_0$. In addition, we expect that the low k part of the dielectric function, which is an increasing function of k for a finite number of layers, becomes negligibly small as the bulk limit is approached. In fact, the derivative of ε_m at $k = 0$, shown as a function of N as (black) squares (right scale) in Fig. 2.2(b), goes to infinity as $N \rightarrow \infty$. Both analyses suggest a dielectric function that converges to a dielectric constant $\varepsilon = 12.96\varepsilon_0$ as the bulk limit is reached, which agrees well with the dielectric constant of bulk MoS₂, $\varepsilon \approx 13\varepsilon_0 - 15\varepsilon_0$, found in the literature. [47] The same procedure was done for other TMDCs, where we obtain the dielectric constants for bulk MoSe₂ ($\varepsilon = 14.83\varepsilon_0$), WS₂ ($\varepsilon = 11.74\varepsilon_0$), and WSe₂ ($\varepsilon = 13.47\varepsilon_0$). This information will be used further in this Section for the ETM calculations of the electron-hole potential in vdW heterostructures.

As for the verification of the expected limits of the ETM method, let us use it to revisit the problem of a monolayer surrounded by two semi-infinite media, i.e. $N = 3$. This problem was analytically solved by N. S. Rytova [50] and, later, by L. V. Keldysh, [51] within some approximations, namely $\varepsilon_2 \gg \varepsilon_{1,3}$ and $d_2 - d_1 = d \ll a_0$. [51] These approximations are such that for a charge in layer $c = 2$, the potential at layer $t = 2$ is

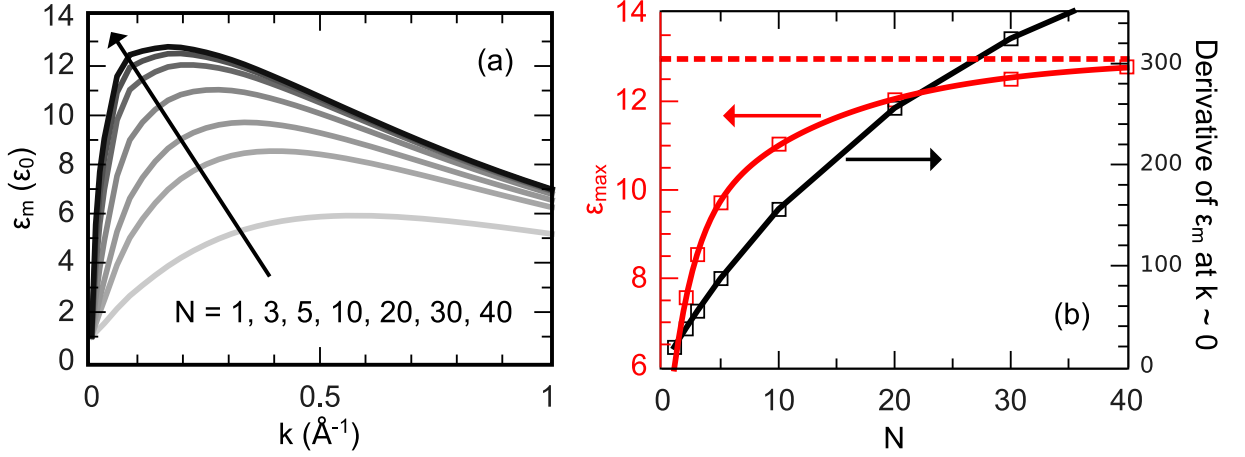


Figure 2.2: (Color online) (a) Average dielectric function for MoS₂ as calculated by QE model for increasing number of layers. (b) Maximum value (red, left scale) of the curves shown in (a), along with their derivatives at $k = 0$ (black, right scale) as a function of the number of layers. Numerical results are shown as symbols. The curve on top of the ϵ_{max} (red) symbols is a fitting function (see text), whereas the one on top of the derivative results (black) is a guide to the eyes.

given by

$$\begin{aligned} V_{eh}^{R-K} &= \frac{e^2}{2\pi\epsilon_0\epsilon_2d} \int_0^\infty \frac{J_0(k\rho)}{1 + \frac{\epsilon_2d}{\epsilon_1+\epsilon_3}k} dk \\ &= \frac{e^2}{4\pi\epsilon_0(\epsilon_1 + \epsilon_3)\rho_0} \left[H_0\left(\frac{\rho}{\rho_0}\right) - Y_0\left(\frac{\rho}{\rho_0}\right) \right], \end{aligned} \quad (2.12)$$

with $\rho_0 = \epsilon_2d/(\epsilon_1 + \epsilon_3)$, which is equivalent to Eq.(2.3) with an effective dielectric function

$$\epsilon^{R-K}(k) = \frac{\epsilon_1 + \epsilon_3}{2} \left(1 + \frac{d\epsilon_2}{\epsilon_1 + \epsilon_3}k \right). \quad (2.13)$$

In fact, for $N = 3$, after some algebra, our model yields

$$\epsilon(k) = \frac{\epsilon_1 + \epsilon_3 + (1 + \frac{\epsilon_1\epsilon_3}{\epsilon_2^2})\epsilon_2 \tanh(dk)}{\left(1 + \frac{\epsilon_1\epsilon_3}{\epsilon_2^2}\right) + \left(1 - \frac{\epsilon_1\epsilon_3}{\epsilon_2^2}\right) \text{sech}(dk) + \frac{\epsilon_1+\epsilon_3}{\epsilon_2} \tanh(dk)} \quad (2.14)$$

One can straightforwardly verify that Eq. (2.13) is the $dk \rightarrow 0$, $\epsilon_{1,3}/\epsilon_2 \rightarrow 0$ limit of Eq. (2.14), as expected. Our model, thus, extends the classical approximation [50, 51] to any value of dielectric constant and slab width, although the approximated linear dielectric function $\epsilon^{R-K}(k)$ can still be seen as a low k limit of $\epsilon(k)$.

The agreement between the effective dielectric functions of suspended monolayer MoS₂ obtained from the theory of Rytova and Keldysh and the ETM approach for low k is verified in Fig. 2.3(a), which also shows the results obtained by the QE method, illustrating somewhat worse agreement with these simpler approaches. Nevertheless, the effective interaction potential for both the suspended case (b) and for MoS₂ over a BN substrate (c), exhibit excellent agreement between all methods, including even the linear (Rytova-Keldysh) approximation for the dielectric function. For these calculations, we

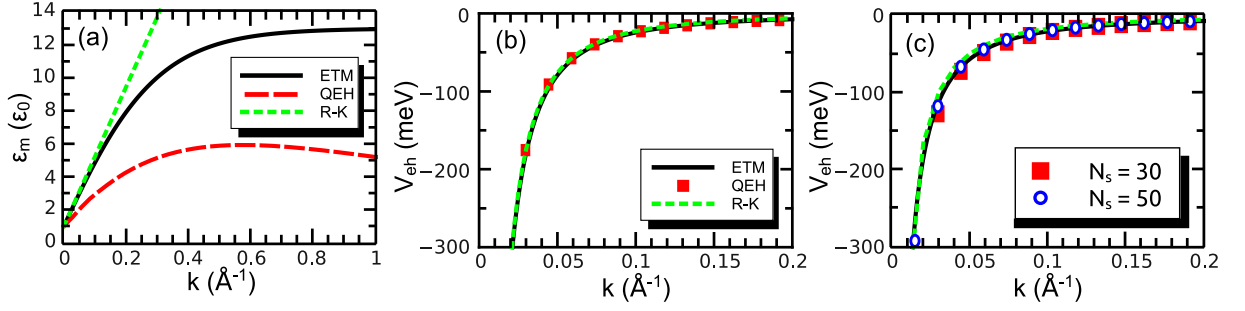


Figure 2.3: (Color online) (a) Effective dielectric function of a suspended monolayer MoS₂ as obtained by ETM and QE methods, as well as with the Rytova-Keldysh effective potential approach. The effective interaction potential between electron and hole, as obtained by these methods, is shown in (b) and (c), for monolayer MoS₂ in the suspended case and over N_s layers of BN substrate, respectively.

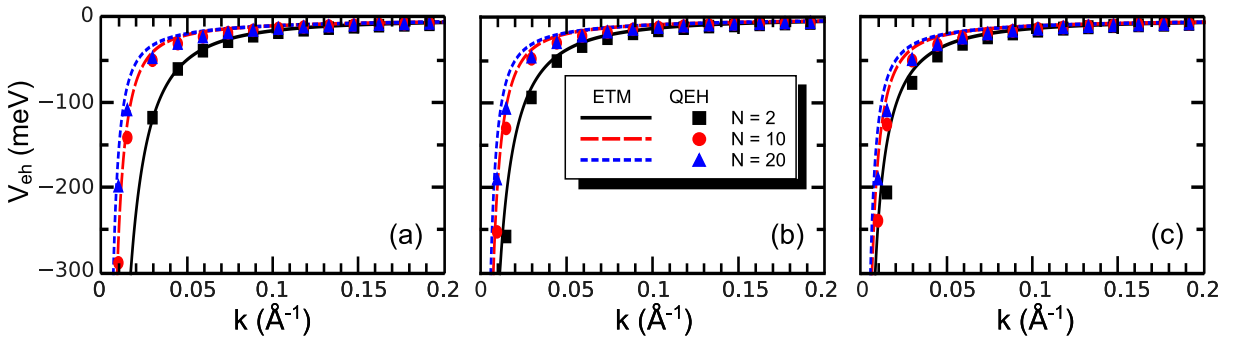


Figure 2.4: (Color online) Screened interaction potential between electron and hole, as obtained by QE (symbols) and ETM (curves) methods, for N -layer MoS₂ (a) in the suspended case, (b) over a BN substrate, and (c) encapsulated by a BN substrate and a BN capping medium.

have assumed $\epsilon_1 = 4\epsilon_0$ (BN substrate), $\epsilon_2 = 12.96\epsilon_0$ (MoS₂) and $\epsilon_3 = 1\epsilon_0$ (vacuum), with $d_1 = -d_2 = 3.15 \text{ \AA}$. Results for other TMDCs are qualitatively the same, and thus we will investigate only MoS₂ in what follows, unless otherwise explicitly stated. In addition, BN is chosen as the substrate (and in some cases capping) material because (i) of the similarity between its static dielectric constant and that of SiO₂, which has been commonly used as substrate in actual experiments, (ii) it is a layered material, which makes it suitable for the QE calculations (although the ETM method allows for use of any kind of material, layered or not, as substrate or capping material), and (iii) because it has been used as capping material in some recent experiments. [59, 27] Increasing the number of layers involved in the QE calculations requires more computational memory, therefore one needs to limit the number of BN layers in the substrate. The QE-obtained potential for MoS₂ over a BN substrate is shown as symbols in Fig. 2.3(c) for $N_s = 30$ (red squares) and 50 (blue circles) BN layers. Indeed, increasing the number of BN layers renders the QE-obtained potential closer to that of the ETM (black solid) one.

The dependence of the screened electron-hole interaction potential on the number of MoS₂ layers is illustrated in Fig. 2.4, for (a) the suspended case, as well as for few layer MoS₂ (b) over a BN substrate, and (c) encapsulated by BN. In all cases, increasing the number of MoS₂ layers produces qualitatively the same effect in both QE (symbols) and

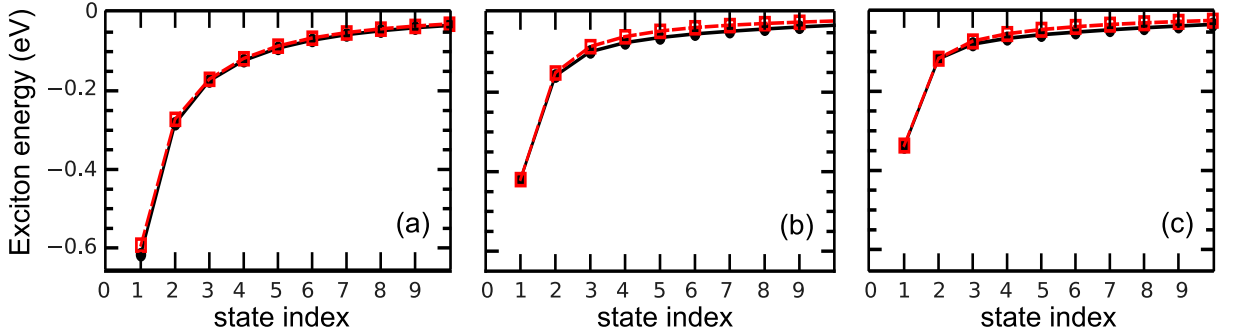


Figure 2.5: (Color online) Exciton energy states, as obtained by ETM (black full circles) and QEH (red open squares) methods, for monolayer MoS₂ (a) in the suspended case, (b) over a BN substrate, and (c) encapsulated by BN. Curves are guides to the eye.

ETM (curves) methods. However, quantitative agreement between results from these two methods becomes somewhat worse as the number of layers increases. In the case of multi-layer MoS₂ over or encapsulated by BN, the lack of quantitative agreement is partially due to the small number of BN layers in the substrate and capping layers employed in our QEH calculations, which are taken as $N_s = 30$ in the former case and $N_s = 15$ (with 15 more BN capping layers) in the latter case. A larger number of BN layers, which would improve this agreement as previously discussed, is found to be very memory intensive when a large number of MoS₂ layers are considered, as in the $N = 20$ case.

The good agreement between these two methods for the monolayer case, especially for high values of k , suggests that low-lying exciton energy states, whose wave functions are narrower (wider) in real (reciprocal) space, as calculated by both approaches will also exhibit similar results. This is indeed verified in Fig. 2.5, which shows the exciton state energies as obtained by ETM (black full circles) and QEH (red open squares) methods for (a) suspended monolayer MoS₂, as well as for this material (b) over a BN substrate and (c) encapsulated by BN. Ground state binding energies are found to be 0.616 eV in the suspended case, in good agreement with previous calculations, [52, 47], whereas in the presence of a BN substrate, this energy is reduced to 0.419 eV and, when encapsulated by BN, it is further reduced to 0.336 eV, due to the additional dielectric screening by the surrounding environment. The difference between the two methods is almost zero for the ground state, but it reaches $\approx 13\%$ for the 8th excited state of suspended MoS₂. Nevertheless, for all cases studied here, the highest energy difference found was ≈ 0.01 eV for highly excited states, which is within the accuracy limitations of usual experimental measurements of these states.

In order to investigate the practical consequences of the observed difference between curves obtained with the ETM and QEH methods in the $N > 1$ case (see Fig. 2.4), we calculate the binding energy of a bound state composed of a positive and a negative charge in N -layer MoS₂. Notice that quantum effects are taken into account only in the QEH method, therefore, this comparison allows us to investigate how strong are these effects on the binding energies, especially for very thin samples, where quantum effects

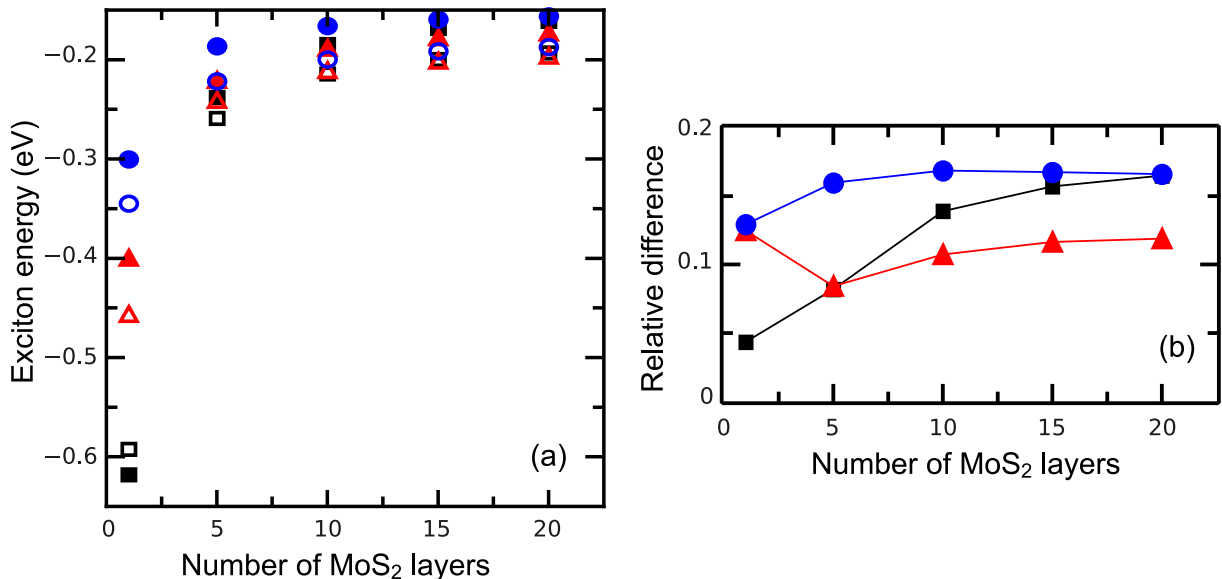


Figure 2.6: (Color online) (a) Exciton ground state energy as a function of the number of MoS₂ layers, as obtained by ETM (full symbols) and QEH (open symbols) methods, in the suspended case (black squares), over a BN substrate (red triangles), and encapsulated by BN (blue circles). (b) Relative difference between results obtained with the ETM and QEH methods. Lines are guides to the eye.

are expected to play a significant role. As this material acquires an indirect gap for $N \geq 2$, the bound state proposed here is not relevant for excitonics, although it can still be used as a measure of the strength of the effective screened Coulomb interaction in the system which is relevant, e.g., for a charge-impurity bound state. Ground state binding energies are shown in Fig. 2.6(a) as a function of the number of MoS₂ layers in the suspended case (black squares), as well as for layers deposited on (red triangles) or encapsulated by BN (blue circles), as obtained by ETM (full symbols) and QEH (open symbols). Differences between methods (relative to the QEH results) are shown in Fig. 2.6(b) to be restricted to a range between 5% and 17%. We point out that as the number of layers increases towards the bulk limit, the ETM method leads to the correct interaction potential. Nevertheless, both methods are demonstrated to agree to a good extent for any number of layers.

We now investigate how the ETM approach performs for an electron-hole interaction potential in two cases recently experimentally investigated, namely, a hetero-bilayer, i.e. a bilayer composed by two different TMDCs,[19, 28, 68, 69, 70, 71, 72, 73, 74] and a TMDC monolayer with extra dielectric screening due to a graphene capping layer. [55]

2.3.2 Inter layer excitons in hetero-bilayers

We have applied the theoretical model described in Sec. II to calculate exciton binding energies in vdW heterostructures consisting of the most common combinations of TMDCs experimentally investigated to date. Since a major focus in these systems is the study of inter-layer excitons, here we consider only heterostructures that exhibit a type-II band alignment, where this kind of exciton is energetically favorable. As part of the search

for Bose-Einstein condensation of spatially polarized (inter-layer) excitons, recent studies [75, 76, 77] have investigated the binding energy of excitonic complexes in TMDCs double layers. In order to provide control of the inter-layer separation, the use of a few-layer BN spacer between the TMDCs that compose the vdW heterostructure has been proposed. [19]

Previous calculations of excitonic complexes in these systems were mostly made under the approximation of a pure Coulomb interaction between electrons in one layer and holes in the other. The interaction potential in this case is given by $V_{Coulomb}(\rho) = -1/\epsilon_s \sqrt{\rho^2 + d_z^2}$, where d_z is the distance between the center of the TMDC layers (where the charges are confined) and ϵ_s is the effective dielectric constant of the surrounding environment. In Fourier space, this potential is given by the expression $V_{Coulomb}(k) = -2\pi e^{-kd_z}/\epsilon_s k$. A comparison between this approximation and the actual potential obtained from solution of the Poisson equation by the ETM method for this combination of dielectric slabs is shown in Fig. 2.7. We consider a MoS₂/WS₂ heterostructure with a BN substrate, a BN capping medium, and a N_s -layer BN spacer between the TMDCs ($\epsilon_r = 4.4 \epsilon_0$), to provide control of the distance between them. We point out that this encapsulation with BN is not necessary for actual heterostructures, but we consider it to enable the comparison with the same situation described by the recent use of the Coulomb approximation, where the possible difference between the dielectric constants of the inter-layer spacer, substrate and capping media has not been taken into account. We observe that interaction potentials obtained from the ETM (solid curves) assuming no BN spacer (i.e. $N_s = 0$, black curves) are not well described by the Coulomb approximation (dashed curves). As the number of layers in the spacer increases to 5 (red), 10 (blue) and 30 (green), the results from these two approaches become more similar. This is reasonable, as the TMDCs layer thickness becomes less significant as compared to the BN media surrounding these layers.

The ETM method and Coulomb approximation are both classical approaches for the inter-layer exciton problem. It is then important to compare the ETM results with the more sophisticated, ab initio based QEH method. Notice that calculations assuming BN as a surrounding environment and spacer would require a very large number of layers in QEH, which makes these calculations computationally expensive. We therefore investigate only the sample case of a suspended MoS₂/WS₂ hetero-bilayer with no BN spacer. Results for this case are shown in the inset of Fig. 2.7, where the ETM (QEH) obtained potential is shown as a black solid curve (red symbols). Potentials from both methods agree very well, and this is true for all combinations of TMDCs we investigated. As a measure of the consequences of the small difference between methods, we compare the exciton binding energies for MoS₂/WS₂, MoS₂/WSe₂, MoSe₂/WS₂ and MoSe₂/WSe₂. We obtain from the QEH method $E_b^{MoS_2/WS_2} = 281$ meV, $E_b^{MoS_2/WSe_2} = 271$ meV, $E_b^{MoSe_2/WS_2} = 279$ meV, and $E_b^{MoSe_2/WSe_2} = 264$ meV, while ETM results overestimate these values by only 4%, 8%, 8% and 7%, respectively. For the sake of simplicity, reduced effective masses are kept

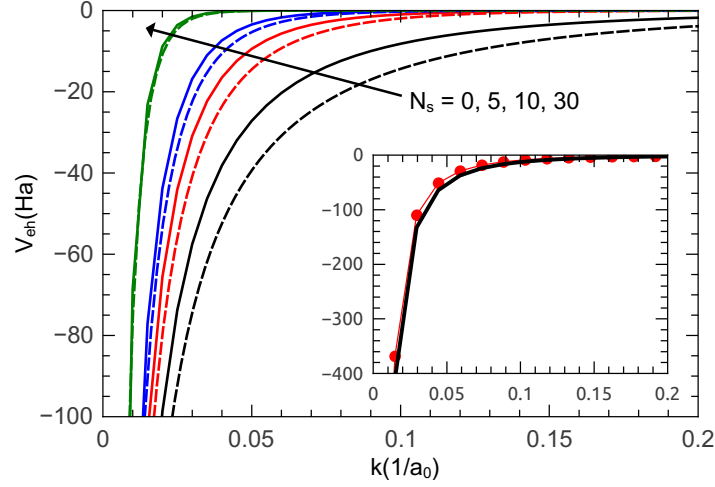


Figure 2.7: (Color online) Comparison between inter-layer electron-hole interaction potentials obtained by the ETM (solid) and the standard Coulomb form (dashed), for a MoS₂/WS₂ heterostructure encapsulated by BN and with a N_s -layer BN spacer between the TMDCs, for $N_s = 0$ (black), 5 (red), 10 (blue) and 30 (green). Inset: comparison between inter-layer electron-hole interaction potentials for suspended MoS₂/WS₂ hetero-bilayer, as obtained by ETM (black solid) and QE (red symbols) methods.

as $0.27m_0$ for all combinations, but numerical results will differ only by a few meV if the true values are considered. One conclusion is immediately drawn from these results: the inter-layer exciton binding energy for all combinations of TMDCs is of the order of ≈ 250 - 300 meV, which is consistent with previous reports in the literature. [53, 60, 78] This is important for the interpretation of experimentally observed photoluminescence peaks for vdW heterostructures. In order to substantiate that a given spectral peak observed in these experiments arises from such fully polarized inter-layer excitons, the energy of this peak needs to be consistent with the inter-layer quasi-particle gap, deduced by a binding energy of the appropriate order of magnitude. Nevertheless, we emphasize that our calculations were done assuming full electron-hole polarization, i.e. with each charge carrier confined exactly at a single layer, with no wave function projection on the other layer. This is expected to be the case for K-to-K point transitions in TMDCs hetero-bilayers. Recent experiments, [57] however, suggest the presence of indirect (in reciprocal space) excitons associated with K-to- Γ transitions, where holes are distributed across both layers, which naturally significantly increases the binding energy of these inter-layer excitons.

Since the ETM provides a realistic inter-layer exciton potential at a low computational cost, it would be interesting to use this improved potential to revisit the problem of inter-layer excitons, trions and biexcitons discussed in the literature.[75, 76, 77] This is, however, outside of the scope of this work and is left as a goal for future work.

2.3.3 Dielectric screening due to a graphene capping layer

In a recent experiment, [55] capping a WS_2 monolayer with multi-layer graphene has been proposed as a way to provide control of the optical gap in the TMDC by engineering of the dielectric screening of the Coulomb interaction. It has been shown that the extra screening due to the graphene capping layer reduces the exciton binding energy, which is verified by the reduction of the energy difference between 1s and 2s states, observed as peaks in the reflectance spectrum around the A-exciton energy range. Although the optical gap of WS_2 is *redshifted* after it is covered with graphene, we point out that the optical gap is comprised of a combination of this binding energy with the quasi-particle gap, which is also renormalized (reduced) via the change in the dielectric environment due to this graphene deposition. The separation between 1s and 2s peaks, however, is unaffected by the quasi-particle gap renormalization, therefore, its reduction after deposition of graphene is a measure of the enhanced dielectric screening of the electron-hole interactions in the WS_2 exciton state.

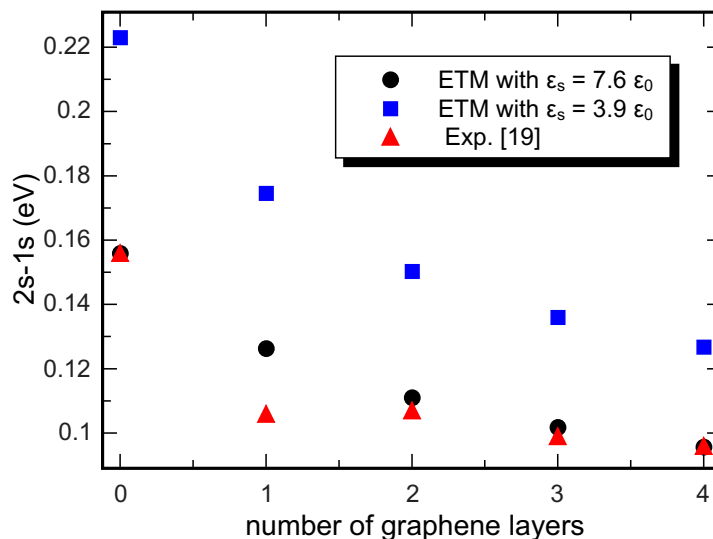


Figure 2.8: (Color online) Difference between ground (1s) and first excited (2s) exciton states in WS_2 as calculated by ETM (black circles), assuming substrate dielectric constants $\epsilon_s = 7.6\epsilon_0$ and $3.9\epsilon_0$. Experimental values for this system [55] are shown as red triangles.

Figure 2.8 shows the 2s-1s separation for exciton states of monolayer WS_2 , as a function of the number of deposited graphene layers. In order to obtain the correct 2s-1s separation for bare WS_2 as compared to the experiment, we had to assume a substrate with dielectric constant around $7.6\epsilon_0$, which is higher than that of SiO_2 , the actual substrate in the sample [55]. The need for such an adjusted dielectric constant for the substrate may be due to imperfections on the interface between WS_2 and the substrate, which are effectively accounted for in the modified constant. In fact, assuming the actual dielectric constant $\epsilon_s = 3.9\epsilon_0$ for the substrate (blue squares), the separation is found ≈ 0.22 eV, which is higher than the experimentally observed ≈ 0.16 eV (red triangles). We assume each

deposited graphene layer to have a 3.36 \AA thickness and the same dielectric constant as graphite ($\epsilon_g = 10\epsilon_0$), as required by the ETM method. As the number of graphene layers increases, the numerically obtained 2s-1s separation decreases, which qualitatively agrees with the experimental data, but theoretical results in the $\epsilon_s = 3.9\epsilon_0$ case are still significantly higher than the experimental ones. On the other hand, numerical results with the adjusted dielectric constant $7.6\epsilon_0$ (black circles) are found with an approximately rigid down shift, thus showing a very good *quantitative* agreement with the experimental data (red triangles). These results validate the ETM method as a powerful tool to investigate the tuning of exciton peaks in Coulomb-engineered systems.

Efficient ab-initio based modeling of dielectric screening in 2D heterostructures

3.1 Motivation

In determining a material's response to electromagnetic fields and for calculating electronic excitations, such as plasmons, excitons, and quasiparticles, the dielectric function, $\epsilon(\mathbf{r}, \mathbf{r}', \omega)$, is of fundamental importance[79]. Due to the long range nature of the Coulomb interaction and the weak intrinsic screening in 2D materials, their dielectric properties are generally highly sensitive to the environment, e.g. embedding layers or substrates.[46, 80, 55] This makes the determination of the dielectric function of embedded or supported 2D materials a critical prerequisite for a realistic description of their electronic and optical properties. However, conventional first-principles schemes are challenged by the incommensurable nature of most 2D/2D or 2D/substrate heterointerfaces. Due to the weak inter-layer interactions, the crystal structure at such heterointerfaces can be highly complex, with either no or very large periodicity due to in-plane lattice mismatch or rotational misalignment. For all but the simplest heterostructures, this implies the use of supercells with many hundreds or thousands of atoms,[25, 26, 81, 82] which makes the problem completely intractable by standard first-principles methods.

The previously introduced quantum electrostatic heterostructure (QEH) model [52] overcomes the problem of large interface supercells and enables an efficient calculation of the dielectric function of general vdW structures containing hundreds of layers. The only assumption behind the scheme is that interlayer hybridization can be neglected when it comes to dielectric screening – an approximation that has proved to be surprisingly good. In a nutshell, the QEH model takes as input a low-dimensional representation of the density response function $\chi(\mathbf{r}, \mathbf{r}', \omega)$ for each isolated 2D layer of the heterostructure. We refer to these as the dielectric building blocks (DBB). The density response function and dielectric function of the entire vdW heterostructure are subsequently calculated by solving a Dyson-like equation which couples the DBBs via the Coulomb interaction.

In the original QEH model, the dielectric building blocks were calculated from first

principles density functional theory (DFT) including screening from electronic transitions. In this work, we extend the model in three important ways. First, we include the contributions from optical phonons into the DBBs. The screening response from phonons govern the dielectric response of polar crystals in the infrared frequency regime. This new feature thus extends the applicability of the QEH model to a new type of materials and frequency regime. Our implementation uses an analytical model for the dielectric function that depends on the optical phonon frequencies and the Born charges of the atoms. Secondly, we added the possibility of accounting for screening from a bulk substrate. This is a rather simple but highly useful feature, as most experiments on 2D materials are performed on bulk substrates, such as quartz, fused silica, or SiO₂. The implementation uses the method of image charges and takes the (local) frequency dependent dielectric constant of the substrate as input. Finally, while the original QEH model only accounts for screening due to interband transitions in semiconductors, the new model includes screening from intraband transitions due to free carriers in the conduction or valence band. This feature is also highly useful, since many 2D semiconductors, when explored experimentally, are doped (intentionally or unintentionally). This method is implemented using a temperature dependent random phase approximation (RPA) model for the dielectric function of free carriers with effective masses obtained from DFT.

Here we outline the theory and implementation of the new feature of the QEH model and illustrate its use by a number of examples. In particular we demonstrate the hybridization of polar phonons in hBN multilayers stacks and how they couple to plasmons in graphene sheets leading to a complex spectrum of hybrid plasmon-phonon excitations.

3.2 Theoretical framework

3.2.1 Basics of the QEH model

We begin by summarizing the main idea behind the QEH model. More details can be found in Ref. [52] and the associated supplementary material. In general, the (inverse) dielectric function is related to the interacting density response function, χ , via

$$\epsilon^{-1}(\mathbf{r}, \mathbf{r}', \omega) = \delta(\mathbf{r} - \mathbf{r}') + \int \frac{1}{|\mathbf{r} - \bar{\mathbf{r}}|} \chi(\bar{\mathbf{r}}, \mathbf{r}', \omega) d\bar{\mathbf{r}}. \quad (3.1)$$

The QEH model calculates the density- and dielectric response functions of the heterostructure in two steps. First, the in-plane averaged density response function of each isolated 2D layer of the heterostructure, $\chi_i(z, z', \mathbf{q}_{\parallel}, \omega)$ (i is the layer index), is calculated. For the electronic response we use the random phase approximation (RPA) with DFT-PBE orbitals and energies, but this is not essential. From χ_i we can obtain the density induced by an external potential of the form

$$\phi(z, \mathbf{q}_{\parallel}, \omega) = f(z) \exp(i\mathbf{r}_{\parallel} \cdot \mathbf{q}_{\parallel}) \exp(i\omega t), \quad (3.2)$$

In the QEH model we specialize to potentials of the form $f_\alpha(z) = (z - z_0)^\alpha$ where z_0 is the center of the layer and $\alpha = 0, 1$. The corresponding induced densities becomes

$$\rho_{i\alpha}(z, \mathbf{q}_\parallel, \omega) = \int \chi_i(z, \bar{z}, \mathbf{q}_\parallel, \omega) \bar{z}^\alpha dz \bar{z}. \quad (3.3)$$

Projecting out the (out-of-plane) monopole and dipole components of the density induced by f_α , we arrive at the basic response functions,

$$\chi_{i\alpha}(\mathbf{q}_\parallel, \omega) = \int z^\alpha \chi_i(z, \bar{z}, \mathbf{q}_\parallel, \omega) \bar{z}^\alpha dz d\bar{z}. \quad (3.4)$$

According to our experience, $\chi_{i\alpha}$, typically exhibits a strong frequency dependence while $\rho_{i\alpha}$ is largely frequency independent. The data set $\{\chi_{i\alpha}(\mathbf{q}_\parallel, \omega), \rho_{i\alpha}(\mathbf{q}_\parallel, \omega = 0)\}$ with $\alpha = 0, 1$ constitutes the dielectric building block (DBB) of layer i . For 2D materials with in-plane anisotropy, \mathbf{q}_\parallel is sampled along two orthogonal directions in the Brillouin zone (BZ). It should be clear that the DBB allows us to compute the induced density due to an external potential of the form 3.2 by performing a first order Taylor expansion of f around the center of the layer.

In the second step, the density response function of the vdWH is obtained by solving a Dyson equation that couples the DBBs together via the Coulomb interaction. The Dyson equation for the density response function of the heterostructure reads (omitting the \mathbf{q}_\parallel and ω variables for simplicity):

$$\chi_{i\alpha, j\beta} = \chi_{i\alpha} \delta_{i\alpha, j\beta} + \chi_{i\alpha} \sum_{k \neq i, \gamma} V_{i\alpha, k\gamma} \chi_{k\gamma, j\beta} \quad (3.5)$$

where the Coulomb matrices are defined as

$$V_{i\alpha, k\gamma}(\mathbf{q}_\parallel) = \int \rho_{i\alpha}(z, \mathbf{q}_\parallel) \Phi_{k\gamma}(z, \mathbf{q}_\parallel) dz \quad (3.6)$$

and $\Phi_{k\gamma}$ is the potential associated with the induced density, $\rho_{k\gamma}$. We obtain $\Phi_{k\gamma}$ by solving a 1D Poisson equation with open boundary conditions. Note that we leave out the self-interaction terms in Eq. (3.5) since the intralayer Coulomb interaction is already accounted for in $\chi_{i\alpha}$. Finally, the (inverse) dielectric function of Eq. (3.1) in the monopole/dipole basis becomes

$$\epsilon_{i\alpha, j\beta}^{-1}(\mathbf{q}_\parallel, \omega) = \delta_{i\alpha, j\beta} + \sum_{k\gamma} V_{i\alpha, k\gamma}(\mathbf{q}_\parallel) \chi_{k\gamma, j\beta}(\mathbf{q}_\parallel, \omega). \quad (3.7)$$

We emphasize that the calculated heterostructure response function is that of an isolated heterostructure (or a heterostructure on a substrate - see later). In particular, we do not apply periodic boundary conditions in the out-of-plane direction when solving the Dyson equation (3.7). Therefore, there is no need to correct for interactions with periodically repeated images as required in supercell approaches. This is, however, important to consider when calculating the response function, $\chi_{i\alpha}$, of the isolated 2D layers[83, 84].

Since we use periodic supercell calculations to obtain the latter we employ an out-of-plane truncated Coulomb interaction to avoid the interaction with periodic images[52].

The QEH method has been benchmarked against experimental exciton binding energies in the original paper[52]. Furthermore, the method has been used to compute EELS spectra of multilayer MoS2 obtaining good agreement with experiments both for excitons and plasmons[85]. This concludes our summary of the original implementation of the QEH model. A description of the various extensions to the QEH model now follows.

3.2.2 Lattice polarization

¹ In addition to the electronic response (corresponding to frozen nuclei), polar materials also respond to external fields via lattice deformations. The contribution from the lattice polarization can be significant for frequencies below or comparable to the optical phonons of the system and can lead to non-trivial effects when coupled to electronic transitions in the same frequency regime. The QEH model has been extended to include this effect.

The lattice contribution to the DBB is obtained from the Born effective charges and Γ -point phonon modes of the isolated 2D material. The Born charges are defined as derivatives of the macroscopic polarization density, $\mathbf{P}(\mathbf{E}, \{\mathbf{u}^a\})$, with respect to atomic displacements under the condition of vanishing macroscopic electric field, \mathbf{E} , (defined as the total electric field averaged over a unit cell of the material).[86, 87] The latter condition ensures that the electron system remains in the ground state during the atomic displacement and is automatically satisfied in a calculation with periodic boundary conditions on the unit cell. When a cell of in-plane area A_{cell} is used to represent the 2D layer, the expression for the Born charges becomes

$$Z_{i,aj} = \frac{e}{A_{\text{cell}}} \left. \frac{\partial P_i}{\partial u_{aj}} \right|_{E=0}$$

where a denotes an atom and ij are cartesian coordinates. The 2D polarization density, P_i , is obtained following the Berry phase formalism of the modern theory of polarization[86, 87] using a finite difference evaluation of the derivative. We have implemented the method in the open source electronic structure code GPAW[88] and used it to compute the Born charges of all the 2D materials in the Computational 2D Materials Database (C2DB)[89] with a finite band gap (around 1000 monolayers).

The lattice polarizability of a 2D material in the optical limit ($\mathbf{q} = \mathbf{0}$) takes the form (see appendix for a derivation)

$$\alpha_{ij}^{\text{lat}}(\omega) = \frac{e^2}{A_{\text{cell}}} \sum_{ak,bl} Z_{i,ak} [(\mathbf{C} - \mathbf{M}(\omega^2 - i\gamma\omega))^{-1}]_{ak,bl} Z_{j,bl}. \quad (3.8)$$

where \mathbf{C} is the force constant matrix in the optical limit, \mathbf{M} is a diagonal matrix containing the atomic masses, and γ is a relaxation rate. We emphasise that the polarizability in

¹This subsection was written by M. N. Gjerding in a published collaboration. See Appendix F

Eq. (3.8) is *local*, i.e. \mathbf{q}_{\parallel} -independent. In general we expect this to be an excellent approximation due to a rather weak \mathbf{q}_{\parallel} -dependence of optical phonons (note that the dispersion of the phonon-*polaritons* in Fig. 3.1 is driven by the macroscopic polarization field in the absence of which the phonons show no dispersion in the considered wave vector range).

To make contact to the QEH formalism we must consider the polarization (per area) induced by a potential, ϕ , of the form (3.2). Writing $\mathbf{E} = \nabla\phi$ and using that $\nabla \cdot \mathbf{P}$ equals the induced electron density, we can obtain the total monopole and dipole components of the DBB of layer i ,

$$\chi_{i0}^{\text{tot}}(\mathbf{q}_{\parallel}, \omega) = \chi_{i0}^{\text{el}}(\mathbf{q}_{\parallel}, \omega) - q_{\parallel}^2 \alpha_{\parallel}^{\text{lat}}(\omega) \quad (3.9)$$

$$\chi_{i1}^{\text{tot}}(\mathbf{q}_{\parallel}, \omega) = \chi_{i1}^{\text{el}}(\mathbf{q}_{\parallel}, \omega) - \alpha_{zz}^{\text{lat}}(\omega) \quad (3.10)$$

where $\alpha_{\parallel}^{\text{lat}}$ denotes the 2×2 in-plane submatrix of α^{lat} . When these DBBs are used in Eqs. (3.5) and (3.7) we obtain the dielectric response function of the vdWH including both electron and phonon contributions.

In addition to the Born charges we have calculated the Γ -point phonon modes (including the dynamical matrix \underline{C}) for all materials in the C2DB. From these data sets it is straightforward to obtain the lattice polarizability in Eq. 3.8. We have compiled the full DBBs for a set of 34 semiconducting transition metal dichalcogenides, graphene, phosphorene, and hexagonal boron-nitride, based on data from the C2DB. These DBBs are also freely available and can be found in Ref. [90]. Compared to the lattice part, the electronic DBB is computationally more demanding as it requires *ab-initio* linear response calculations as function of q_{\parallel} and ω .

3.2.3 Bulk substrates

The inclusion of substrate screening is implemented by the method of image charges. In the absence of a substrate we obtain the potential generated by an induced density layer i by solving the 1D Poisson equation (ω - and \mathbf{q}_{\parallel} -variables omitted)

$$\frac{\partial^2}{\partial z^2} \Phi_{i\alpha}(z) - q_{\parallel}^2 \Phi_{i\alpha}(z) = -4\pi \rho_{i\alpha}(z). \quad (3.11)$$

with open boundary conditions (as usual α denotes the monopole/dipole index). In the presence of a substrate, situated a distance d below the layer, we must add the potential from the image charge distribution (see supplementary material). The latter is given by[91]

$$\rho_{i\alpha}^{\text{image}}(z) = -\frac{\epsilon^{\text{sub}} - \epsilon_0}{\epsilon^{\text{sub}} + \epsilon_0} \rho_{i\alpha}(-z - 2d), \quad (3.12)$$

where ϵ^{sub} is the frequency-dependent (but wave vector independent) bulk dielectric constant of the substrate. The potential corresponding to $\rho_{i\alpha}^{\text{image}}$ is obtained by a similar scaling/reflection operation on $\Phi_{i\alpha}$.

3.2.4 Doped graphene

It is well known that electronic properties of (doped) graphene are extremely difficult to describe accurately by pure *ab-initio* methods because of its highly dispersive linear bands[92] that require exceedingly dense k -point grids. To overcome this problem, we construct a DBB for graphene by complementing the *ab-initio* calculated induced density profiles Eq. (3.3) (which are not k -point sensitive) by an analytical model of the density response function.

Within the Dirac model the non-interacting 2D dynamical polarizability of a graphene sheet with a finite doping level reads,[93]

$$\chi_0(\mathbf{q}, \omega) = \frac{1}{\pi^2} \int d^2\mathbf{k} \sum_{\nu, \nu'=\pm 1} F_{\nu, \nu'}(\mathbf{k}, \mathbf{q}) \frac{f_{\nu}(k) - f_{\nu'}(|\mathbf{k} + \mathbf{q}|)}{\hbar\omega + E_{\nu}(k) - E_{\nu'}(|\mathbf{k} + \mathbf{q}|) + i\eta}, \quad (3.13)$$

where $E_{\pm}(k) = \pm\hbar v_F k - E_F$ and $f_{\nu}(k)$ is the Fermi-Dirac distribution. The prefactor,

$$F_{\nu, \nu'}(\mathbf{k}, \mathbf{q}) = \frac{1}{2} \left(1 + \nu\nu' \frac{k^2 + kq \cos \theta}{k|\mathbf{k} + \mathbf{q}|} \right) \quad (3.14)$$

is defined by the overlap of the wave functions.

Life-time limiting scattering processes are taken into account by the relaxation time (RT) approximation [94, 95],

$$\chi_0^{\tau}(\mathbf{q}, \omega) = \frac{(1 - i\omega\tau)\chi_0(\mathbf{q}, 0)\chi_0(\mathbf{q}, \omega + i/\tau)}{\chi_0(\mathbf{q}, \omega + i/\tau) - i\omega\tau\chi_0(\mathbf{q}, 0)}, \quad (3.15)$$

where τ is a phenomenological scattering time. Finally, the full interacting density response function is obtained in the RPA[96, 97, 98]

$$\chi(\mathbf{q}, \omega) = \frac{\chi_0^{\tau}(\mathbf{q}, \omega)}{1 - \chi_0^{\tau}(\mathbf{q}, \omega)V_c(\mathbf{q})}. \quad (3.16)$$

where $V_c = 1/q$ denotes the 2D Coulomb interaction.

We construct a hybrid graphene DBB by combining the analytical result for the density response function with the induced density obtained from the *ab-initio* response function, see Eq. (3.3). The latter is well defined even for relatively coarse k -point grids and can easily be interpolated to an arbitrarily fine q -point grid. The above considerations apply to the monopole component of the DBB. As it turns out, the dipole component is not very sensitive to the employed k -point grid and does not require special treatment. The calculations for the plasmon-phonon coupling in graphene/hBN heterostructures presented in subsection 3.3.2 employed a hybrid graphene DBB.

3.2.5 Doped 2D semi-conductors

Finally, the QEH model has been extended to account for doping in 2D semi-conductors. Dielectric building blocks for intrinsic 2D semiconductors can be generated straightforwardly from the *ab-initio* response function as described in the original paper[52]. To

extent the theory to doped 2D semiconductors we must add the contributions from intraband transitions due to the free carriers in the conduction band (for n-type doping) or valence band (for p-type doping). In the zero temperature limit, and for sufficiently low doping where the effective mass approximation holds, the intraband contribution can be modeled by the response function of a 2D electron gas,[99]

$$\chi_0^{2\text{DEG}}(\mathbf{q}, \omega, \mu, T = 0) = \frac{1}{2\pi^2} \int_0^{\sqrt{2m^*\mu}} d^2\mathbf{k} \frac{f_0(k) - f_0(|\mathbf{k} + \mathbf{q}|)}{\hbar\omega + E(k) - E(|\mathbf{k} + \mathbf{q}|) + i\eta}, \quad (3.17)$$

where

$$\mu(T = 0) = \frac{\hbar^2 k_F^2}{2m^*}, \quad (3.18)$$

and m^* is the carrier effective mass. The expression can be generalized to finite temperatures, [100]

$$\chi_0^{2\text{DEG}}(\mathbf{q}, \omega, \mu, T) = \int_0^\infty d\mu' \frac{\chi_0(\mathbf{q}, \omega, \mu', T = 0)}{4T \cosh^2[(\mu - \mu')/2T]}, \quad (3.19)$$

where the chemical potential is defined a

$$\mu(T) = k_B T \ln [\exp(\epsilon_F/k_B T) - 1]. \quad (3.20)$$

Finally, the interacting response function of the free carrier gas, $\chi^{2\text{DEG}}$, is calculated in the RPA from Eq. (3.16).

A complete DBB for the doped semiconductor is constructed by adding $\chi^{2\text{DEG}}$ to the monopole component of the DBB of the intrinsic semiconductor (Eq. (3.4) with $\alpha = 0$). We do not include the effect of free carriers in the dipole component.

3.3 Results and Discussion

3.3.1 Phonon polaritons in hBN multilayers

As an initial example we consider the hybridization of the longitudinal optical (LO) phonons in a 10-layer film of hBN. It is well known that the dielectric function exhibits poles in the (complex) ω -plane at the excitation energies of the system. To unravel the excitation spectrum we calculate the loss function[101]

$$S(\mathbf{q}_{\parallel}, \omega) = -\text{Im}(\text{Tr}\epsilon^{-1}(\mathbf{q}_{\parallel}, \omega)) \quad (3.21)$$

where ϵ^{-1} is the dielectric matrix defined by Eq. 3.7. The loss function of the hBN slab is shown in Fig. 3.1(a). The intensity of the spectral peaks is a measure for how strongly the excitation couples to a local potential of the form (3.2). Due to the large band gap of hBN, the electronic contribution to the dielectric function reduces to a real constant, ϵ^∞ , over the considered frequency regime, and consequently the dielectric response is governed solely by the lattice vibrations. We focus on the energy range of the optical in-plane phonon modes (the dipole carrying out-of-plane optical modes appear in the spectrum

just below 100 meV, see flat yellow line in Fig. 3.2(b-d)). There are ten in-plane TO modes and ten in-plane LO modes. The TO modes are all degenerate with energy, $\hbar\omega_{\text{TO}}$ and show no dispersion (see discussion below). We note that these modes are not seen in the spectrum because they do not couple to fields of the form (3.2).

In polar bulk crystals the longitudinal- and transverse optical phonon modes (LO and TO) will be split for $q_{\parallel} \rightarrow 0$ due to the finite macroscopic polarization of the LO mode. However, in a 2D material the LO-TO splitting vanishes for $q_{\parallel} \rightarrow 0$ because the electric field produced by the finite macroscopic polarization vanishes in this limit[102]. This effect is clearly seen in Figure 3.1. At finite q_{\parallel} , however, the electric field produced by the polar LO phonons leads to significant coupling between them, resulting in the formation of phonon-polaritons subbands. The standing wave profile of the subband modes is sketched in Fig. 3.1(b).

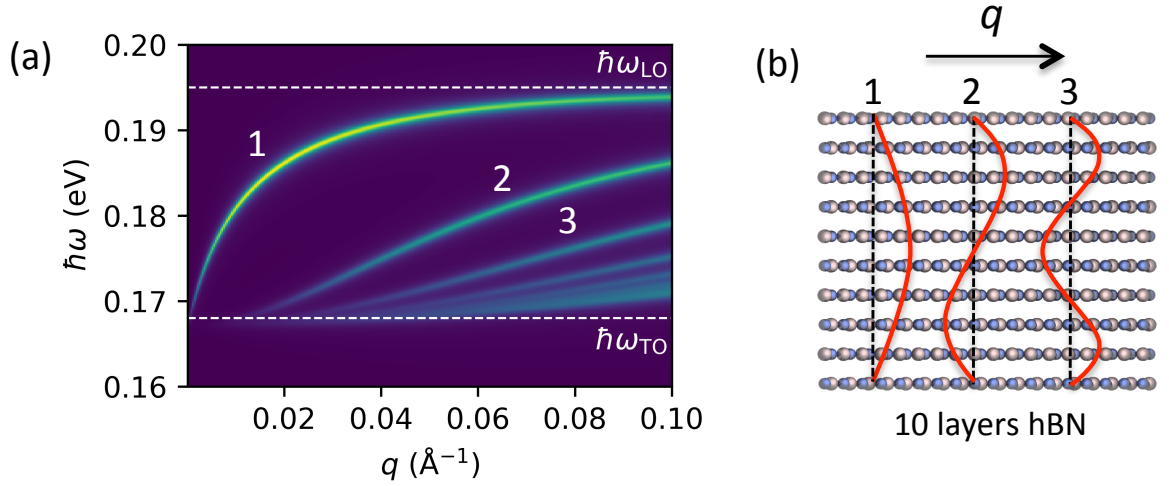


Figure 3.1: Loss function (3.21) of a 10-layer hBN stack reveals the formation of subbands of longitudinal in-plane phonon-polaritons. The white dashed lines correspond to the in-plane TO and LO frequencies of bulk hBN. The well known breakdown of the LO-TO splitting in the $q \rightarrow 0$ for 2D materials is clearly seen. The strong hybridization of the LO sheet phonons leading to the subband formation is due to electrostatic interactions captured by the QEJ model.

It should be stressed that the observed hybridization of phonon modes is an effect of the macroscopic electric field set up by the polar lattice vibrations. It would therefore *not* be captured by a conventional DFT phonon calculation that does not explicitly include macroscopic electric field, which would yield ten degenerate pairs of LO-TO phonon modes, because sheet phonons are able to couple via short-range electrostatics (that is, compatible with the periodic boundary conditions of the super-cell of the phonon calculation) and quantum mechanical interlayer hybridization, thus neglecting any macroscopic effects. On the other hand, short-range electrostatics and the quantum mechanical interlayer hybridization is not accounted for by the QEJ model (just like the effect of interlayer wave function hybridization is neglected in the electronic response). Fortunately, this type of short-range interlayer phonon coupling is usually very weak in vdW

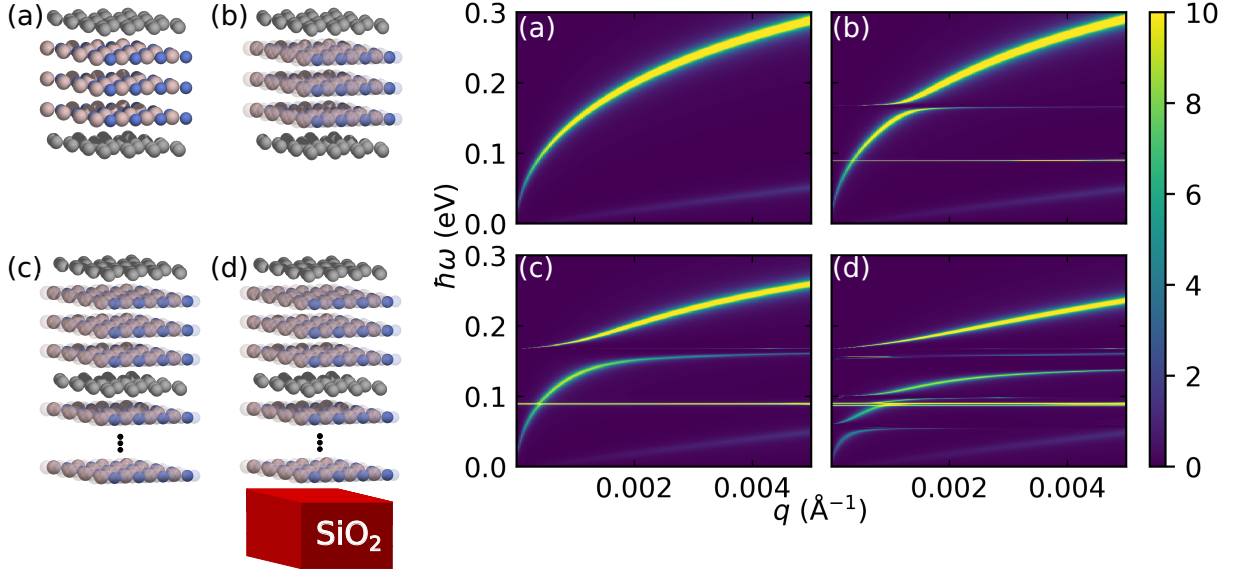


Figure 3.2: Loss function (3.21) of freestanding and supported graphene/hBN heterostructures. (a) Two doped graphene sheets separated by 3 layers of hBN. Only the electronic response is included in the dielectric building blocks. (b) Same as (a) but with the phonon contribution included in the hBN building blocks as indicated by a blurring of the atoms. (c) Same as (b) but with 18 layers of hBN added below the heterostructure. (d) Same as (c) but with the entire heterostructure placed on a SiO₂ substrate. Screening from the substrate is described by the dielectric function in Eq. (3.22) with $\epsilon_\infty = 2.4\epsilon_0$, $f_j = (0.7514, 0.1503, 0.6011)$ and $\omega_{\text{TO},j} = (0.055, 0.098, 0.140)$ eV.

bonded materials[103] and can be safely ignored for the purpose of modeling the dielectric properties.

3.3.2 Plasmon-phonon coupling in graphene/hBN

As another example we consider the coupling of graphene plasmons with the optical phonons in hBN. Experiments have reported that the strong coupling between graphene plasmons and polar phonons can create new hybrid modes with significantly altered dispersion curves.[104, 105, 106, 107, 108]. The effect has been reproduced theoretically using semi-classical models[109]. In contrast, the approach presented here is fully *ab-initio* subject to the approximations underlying the QEH model; in particular, it is completely parameter free.

In Fig. 3.2 we show the calculated loss function (3.21) of four different graphene/hBN heterostructures. For all structures the graphene sheets are n-doped with a carrier concentration corresponding to $E_F = 0.4$ eV and relaxation rate of $\hbar\omega = 1$ meV (to obtain an accurate description of the plasmon in the doped graphene layer we employ a hybrid analytical/*ab-initio* DBB as described in Sec. 3.2.4). Panel 3.2(a) refers to a structure composed by two graphene sheets separated by 3 layers of hBN. For this case phonons are *not* included in the DBB of the hBN layers. The plasmon dispersion presents two branches, corresponding to out-of-plane symmetric and anti-symmetric combinations of the graphene sheet plasmons.

In panel 3.2(b), the phonon contribution is included in the hBN building block. This leads to an anti-crossing where the symmetric plasmon intersects the hBN in-plane LO phonon. The faint line just below 100 meV represents the optical out-of-plane phonons of the hBN sheet. The out-of-plane phonons also couple to the plasmon, but the anti-crossing is very weak and can hardly be seen on this scale. In panel 3.2(c), we added 18 layers of hBN below the heterostructure. This leads to a stronger phonon response, and consequently an enhancement of the anti-crossings with the plasmon. Finally, we place the entire structure on top of a SiO₂ substrate. Despite the fact that the graphene sheets are separated from the substrate by an 18-layer thick hBN film, there is a significant effect on the loss spectrum. In particular, new regions of anti-crossings appear where the plasmon dispersion intersects the three SiO₂ phonon resonances at 55 meV, 98 meV, and 140 meV, respectively.

In these calculations, the effect of the substrate is included via the dielectric function[31, 110, 95]

$$\epsilon_{\text{SiO}_2}(\omega) = \epsilon_\infty + \sum_{j=1}^3 f_j \frac{\omega_{\text{TO},j}^2}{\omega_{\text{TO},j}^2 - \omega^2}, \quad (3.22)$$

where ϵ_∞ is the electronic dielectric constant and $\omega_{\text{TO},j}$ is the frequency of the j th transverse optical phonon. Comparing to Eq. (3.8), the dimensionless term f_j can be interpreted as the Born charge of the j th mode.

3.3.3 Substrate screening of excitons in MoS₂

As another illustration of the importance of substrate screening, we consider a monolayer of MoS₂ placed on top of an hBN substrate. We compare two different models: In model 1, the substrate is represented by 100 layers of hBN building blocks. In model 2, the substrate is represented as a homogeneous bulk dielectric using the method of image charges as described above. The two models are sketched in Fig. 3.3(a). To account for the anisotropy of the hBN substrate, we use the geometric mean of the in- and out-of-plane dielectric constants $\epsilon(\omega) = \sqrt{\epsilon_z(\omega)\epsilon_{\parallel}(\omega)}$. [111] The bulk dielectric constants are obtained from RPA calculations employing the same parameter settings as used for the DBBs. We stress that we do not include phonons in these calculations even though it would be straightforward to do so. The image plane of the bulk substrate is set at $-d$ relative to the center of the MoS₂ layer, where d denotes the interlayer spacing in bulk MoS₂.

In Fig. 3.3(b) we compare the dielectric function of the supported MoS₂ obtained with the two substrate models, which shows good agreement for large $q > 0.1 \text{ \AA}^{-1}$. For $q > 0.005 \text{ \AA}^{-1}$ (see inset) the two models show good agreement except for a constant offset of about 5% most likely originating from the inclusion of hybridization in the bulk RPA calculation. For small $q < 0.005 \text{ \AA}^{-1}$ (see inset) model 1 reproduces the 2D limit $\epsilon(q = 0) = 1$ because the substrate is in fact a 2D film (albeit not atomically thin).[46]

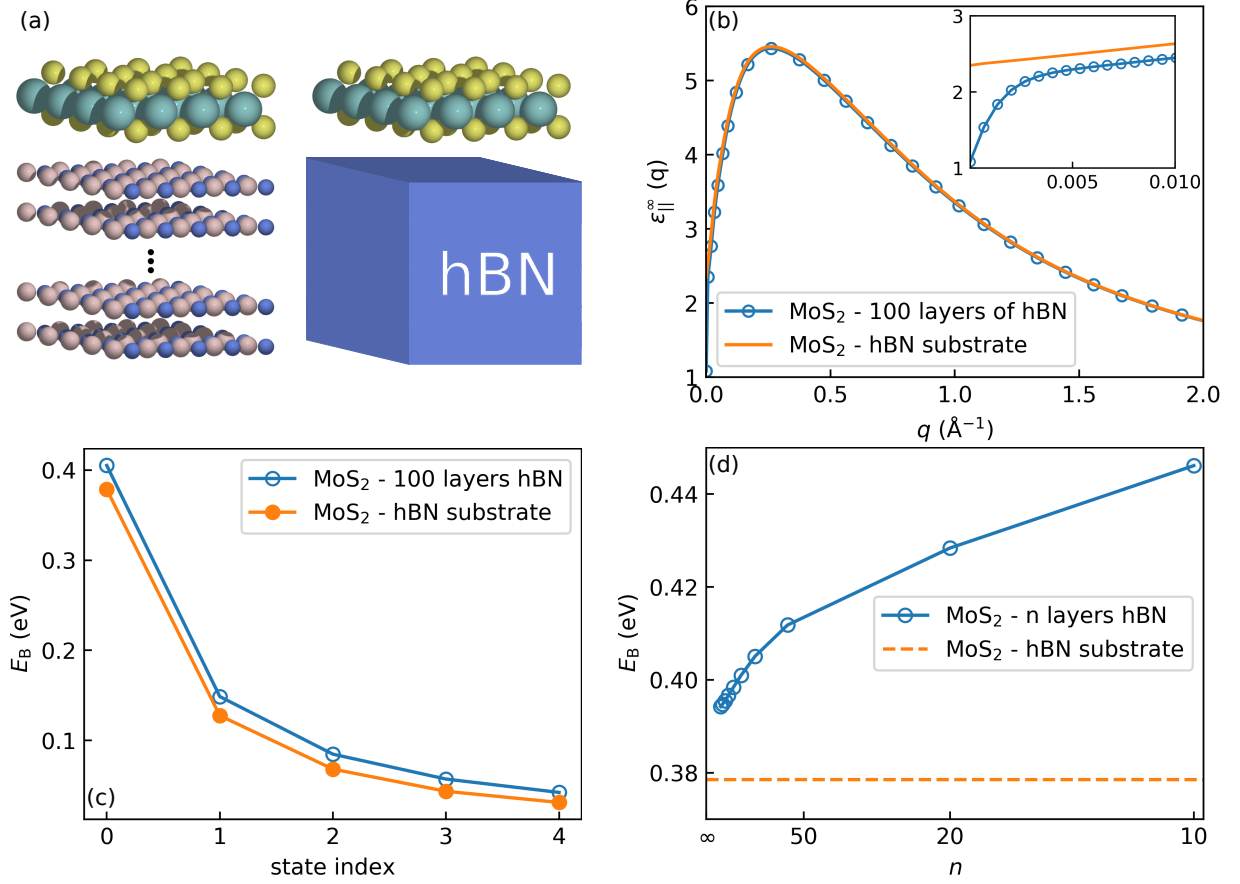


Figure 3.3: Effect of substrate screening on excitons in MoS₂. (a) We consider two different models for the substrate, namely n layers of hBN dielectric building blocks (model 1) and a homogeneous bulk dielectric (model 2). (b) Comparison of the dielectric function of the supported MoS₂ layer obtained with the two different substrate models. The dielectric function of freestanding MoS₂ is shown for comparison. Note that model 1 reproduces the 2D limit $\epsilon(q) \rightarrow 1$ for $q \rightarrow 0$ because the substrate has finite thickness. (c) Binding energies of the lowest five s excitons in MoS₂. (d) Exciton binding energies for the lowest exciton in MoS₂ as function of the number of hBN layers included in model 1.

In contrast, with a bulk substrate the dielectric function converges to $(1 + \epsilon_{\text{hBN,bulk}})/2$ for $q \rightarrow 0$.

In Fig. 3.3(c) we compare the binding energies of the lowest bright exciton in the MoS₂ layer obtained with the two different substrate models calculated within the static approximation. The exciton energies were calculated from the Mott-Wannier model as described in [53]. Again, the two models are generally in good agreement. The small difference between the binding energies calculated with model 1 and model 2 originates from the 5% difference in dielectric functions and is not essential. The inclusion of a substrate predicts lower binding energies compared to free standing MoS₂, also in agreement with literature[45]. Increasing the number of hBN layers in the thin film substrate (model 1), the exciton binding energies converge towards a value very close to that obtained with the bulk substrate (model 2), see Fig. 3.3(d).

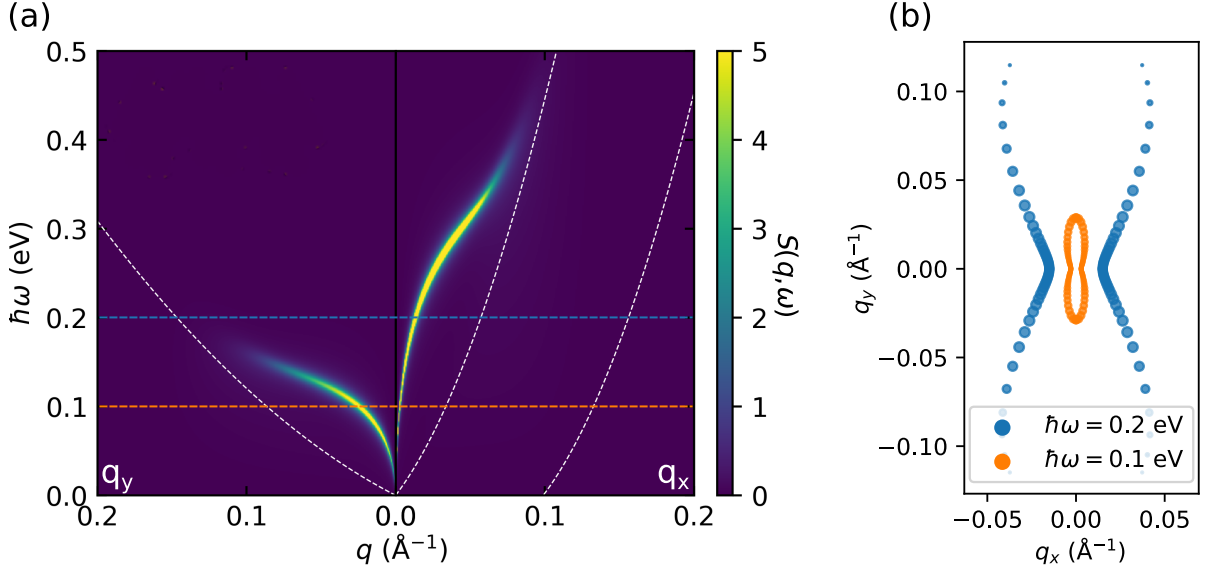


Figure 3.4: (a) Loss function of n-doped monolayer black phosphorus. The in-plane structural anisotropy is reflected by the different plasmon dispersion curves in the x and y directions. Dashed white lines indicate the Landau damped regions. (b) Isofrequency contours evaluated for $\hbar\omega = 0.1\text{eV}$ and $\hbar\omega = 0.2\text{eV}$ corresponding to the normal and hyperbolic frequency regimes, respectively.

3.3.4 Hyperbolic plasmons in doped phosphorene

As a final example of the new implementation, we calculate the loss function of a single layer black phosphorus, see Fig. 3.4. It is well-known that the in-plane structural anisotropy of phosphorene is significantly reflected in the electronic and optical properties[112, 113], meaning that the employed effective mass would be anisotropic as well (see appendix C for details). The calculations employed a DBB with the effect of the free carriers described by the 2DEG response function with a doping concentration corresponding to $E_F = 0.05\text{ eV}$, relaxation rate of $\hbar\omega = 1\text{ meV}$, temperature of 300 K, and effective masses $m_y^* = 0.17m_0$ and $m_x^* = 1.12m_0$. The anisotropy is clearly seen in Fig. 3.4(a) where the different effective masses lead to different plasmon dispersion relations in the x and y directions, respectively. The white dashed lines indicate the limits of the Landau damping regions where the plasmons decay into electron-hole pairs.

The anisotropy of phosphorene leads to hyperbolic isofrequency contours[114, 115] as shown in Figure 3.4(b). The isofrequency contours are plotted at two frequencies that lie inside and outside the hyperbolic frequency regime of $0.15\text{ eV} < \hbar\omega < 0.35\text{ eV}$, respectively. In these plots the size of the markers indicate the normalized plasmon propagation lengths (appendix D) showing that larger losses appear for the high momentum modes as they approach the Landau damped regions. Crucially, the inclusion of spatial non-locality limits the extend of the asymptotes, which would otherwise extend infinitely, and renormalizes the plasmonic density of states. An equivalent effect is observed in bulk metamaterials [116].

3.4 QEH Python package

The QEH model is now available as a standalone package written entirely in Python and is published on the Python Package Index (PyPI) at <https://pypi.org/project/qeh> and is documented at <https://qeh.readthedocs.io>.

For convenience the QEH package also includes an internal library of 2D material thicknesses and effective masses (see appendix E). 2D material thicknesses are available only for those 2D materials which have a bulk counterpart present in the inorganic crystal structure database (ICSD) which amounts to 17 2D materials. The layer thicknesses are then simply given by the unit cell height of the bulk material divided by the number of layers in the unit cell. Effective masses are obtained from the C2DB for 44 2D materials (appendix E).

Enhancing and Controlling Plasmons in Janus MoSSe-Graphene Based van der Waals Heterostructures

4.1 Motivation

Van der Waals heterostructures [19] (vdWHs) open the possibility to combine various properties of layered materials to achieve new applications [55, 42, 117, 118, 119, 120, 121, 122, 123, 124, 125]. An interesting combination is the one between graphene, which presents Dirac cones in the low energy range of its band structure [92], and transition metal dichalcogenides (TMDs), which exhibit a direct band gap in monolayer form [2].

Graphene is a carbon based two-dimensional (2D) material composed by a single layer of atoms arranged in a hexagonal lattice. On the other hand, TMDs have MX_2 form, with a metal (M) layer sandwiched by two layers of a chalcogen (X) [126]. Recently, a new prototype of TMDs called Janus structures [127] have attracted considerable attention [128, 129, 130, 131]. In this structure, the TMD reflection symmetry in the out-of-plane (z -)direction is broken by changing one layer of chalcogens X in MX_2 by a layer of another chalcogen Y, thus leading to MXY . This results in different electronegativity for each side, which induces an out-of-plane dipole that is intrinsic to the system. This feature, in combination with the stacking of semimetallic electrodes (such as graphene), creates new possibilities for applications as p-n junctions that are doped without the need of any external interaction [132]. Knowing the energy difference across the Janus structure, it is possible to easily control the graphene doping by changing the number of Janus TMDs layers stacked in the system.

In this work, we investigate the effect of stacking MoSSe layers (our Janus TMDs of choice) intercalated with graphene layers, on their plasmonic states [133, 134, 135, 136, 137, 138, 139]. The choice of MoSSe as a Janus material is motivated by its recent experimental synthesis, starting from MoS_2 [127] or MoSe_2 [140]. Several properties of this monolayer, including optical and magnetic properties, have already been studied in the literature [141, 142]. Our results show that, by means of structure engineering, plasmon

energies can be controlled, reaching values up to 0.5 eV. Furthermore, we demonstrate that it is possible to selectively quench certain branches of the plasmon dispersion. Finally, we investigate other Janus TMDs candidates that could improve the effects discussed here, by adjusting the relation between the dipole shift and band gap.

4.2 Computational Methods

The quantum-electrostatic heterostructure (QEH) [52] model is employed to calculate the plasmonic properties in different graphene-MoSSe heterostructures. Within this model, the dielectric response of the component layers is calculated independently with density functional theory (DFT) and the total response of the heterostructure is then built by coupling the monolayers together by the Coulomb interaction. Using this model, one can efficiently calculate the dielectric properties of vdWHs with ab initio precision.

However, resolving the low energy linearly dispersive bands of graphene introduces a practical problem for DFT calculations, namely, that a high density of k points is necessary to properly describe its physical properties, and this greatly increases the computational costs. To overcome this problem, we used an analytical solution for the doped graphene density response function. We start by calculating the non-interacting 2D polarizability [93] for a finite doping, and then we express it within the relaxation-time (RT) approximation to take into account possible extrinsic processes [143]. Finally, using the Random Phase Approximation (RPA), we derive the full interacting density response function. We combine the analytical solution of the density response function with the DFT results for the induced density, that is well-defined even for a low density of k points, thus creating a hybrid graphene dielectric building block for QEH calculations.

4.3 Results and Discussion

Let us first study a system composed by MoSSe layers encapsulated by graphene, as illustrated in the inset in Fig. 4.1. As discussed in the Introduction, the intrinsic dipole created by the asymmetry in electronegativity between the S and the Se atoms of the MoSSe layer induces an electric field that creates n- and p-type doping on the top and bottom graphene layers, respectively. This system resembles a capacitor and, in what follows, we demonstrate that the dependence of its doping level on the number of MoSSe layers can be described by a simple model that requires only a few material-specific parameters.

The total electric field, $\mathbf{E} = \mathbf{E}_{\text{MoSSe}} + \mathbf{E}_{\text{depol}}$, is defined as the sum of the electric field created by the intrinsic dipole of the MoSSe layers

$$\mathbf{E}_{\text{MoSSe}} = \frac{\Delta\epsilon_{\text{MoSSe}}}{t} \hat{\mathbf{z}}, \quad (4.1)$$

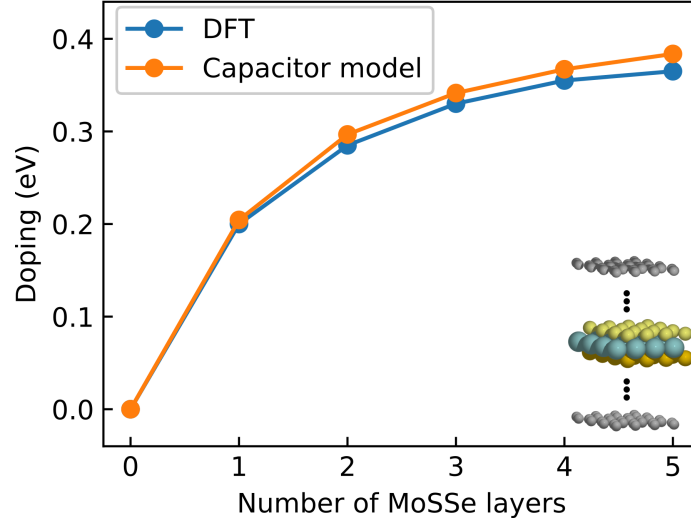


Figure 4.1: Graphene doping level as a function of the number of MoSSe layers, for the structure illustrated in the inset, as calculated using DFT (blue) and the capacitor model (orange), with $t = 6.4 \text{ \AA}$, $\Delta_{\text{MoSSe}} = 0.51 \text{ eV}$ and $\epsilon = 1.76$.

in which $\Delta\epsilon_{\text{MoSSe}}$ is the energy difference generated by the built-in dipole, also known as the dipole shift, t is the thickness of the MoSSe layer, and the depolarization field generated by the induced density on the graphene layers,

$$\mathbf{E}_{\text{depol}} = -\frac{\sigma}{2\epsilon\epsilon_0}\hat{\mathbf{z}}, \quad (4.2)$$

where σ represents the graphene induced density, given by $\sigma = \epsilon_{\text{F}}^2/\pi\hbar^2v_{\text{F}}^2$ in atomic units. The effective dielectric constant in the z direction in MoSSe is assumed to be $\epsilon = 1+4\pi\alpha_{3\text{D}}$, where $\alpha_{3\text{D}}$ is the average long-wavelength polarizability of bulk MoSSe, which is obtained from its monolayer static polarizability as $\alpha_{3\text{D}} = \alpha_{2\text{D}}/t$.

Hence, modeling the doping in the system by assuming a Fermi energy

$$2\epsilon_{\text{F}} = Ed, \quad (4.3)$$

where d is the distance between the plates of an analogous capacitor, which is simply given by the product of the number of MoSSe layers N and the thickness t , we finally obtain

$$\epsilon_{\text{F}} = \frac{-1 + \sqrt{1 + aN^2\Delta_{\text{MoSSe}}}}{aN}, \quad (4.4)$$

with

$$a = \frac{t}{2\epsilon\epsilon_0\pi\hbar^2v_{\text{F}}^2}. \quad (4.5)$$

In Fig. 4.1, we compare the results from such capacitor model with those from DFT calculations [132] for the dependence of the graphene doping on the number of MoSSe layers, considering the system shown in the inset, assuming $t = 6.4 \text{ \AA}$, $\Delta_{\text{MoSSe}} = 0.51 \text{ eV}$ and $\epsilon = 1.76$. Good agreement between the results is observed even for a high number of layers, where the doping level reaches an upper bound due to the increasing strength of

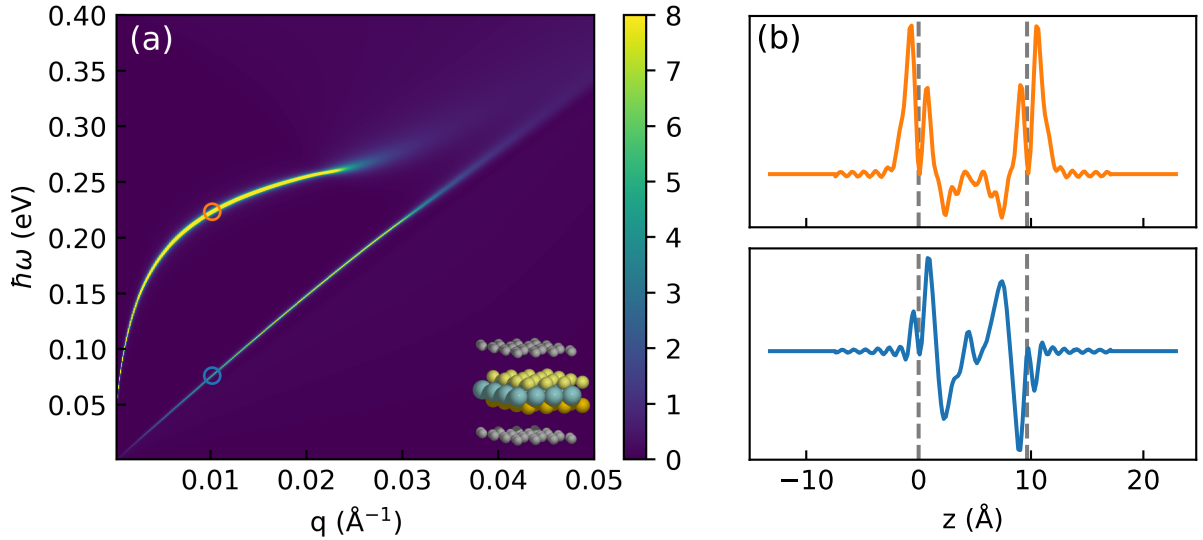


Figure 4.2: (a) Loss function for monolayer of MoSSe encapsulated by graphene, as illustrated in the inset, with $\epsilon_F = 0.2$ eV and relaxation rate of $\hbar\omega = 1$ meV. Induced density presents one symmetric and one antisymmetric mode, as shown in (b) for the higher (top, orange) and lower (bottom, blue) energy branches at $q = 0.01$ \AA^{-1} . The vertical dashed grey lines represent the graphene layers positions.

the depolarization field, which ends up cancelling out the dipole shift of the MoSSe layers. Such good agreement between the results from ab initio and the capacitor model gives us confidence that the latter would also apply in more complex heterostructures, where DFT calculations would be impractical.

In order to demonstrate the effectiveness of the graphene doping achieved by stacking it with MoSSe, we have calculated the loss function $\mathcal{L} = -\text{Im}\{\epsilon_{\text{RPA,RT}}^{-1}(q, \omega)\}$, for a monolayer of MoSSe encapsulated by doped graphene. Results are presented in Fig. 4.2(a), which exhibits two plasmon branches: a symmetric optical plasmon, with higher frequency, and an antisymmetric acoustic plasmon, with lower frequency. The (anti)symmetry across the system is verified by its induced density, in Fig. 4.2(b) for $q = 0.01$ \AA^{-1} .

As a consequence of the previously mentioned compensating depolarization field, increasing the number of MoSSe layers beyond $N \approx 6$ does not lead to a significant increase in the doping level of the graphene layers, which ultimately limits the achievable plasmon energies. In order to circumvent this problem, one could take advantage of the fact that the direction of the intrinsic dipole is defined by the relative ordering of sulfur and selenium atoms in the MoSSe structure, and thus stack more layers with opposite ordering surrounding a middle graphene layer, as represented in the inset of Fig. 4.3. This increases the maximum achievable doping level of the middle graphene layer beyond the threshold of the bilayer graphene-MoSSe heterostructure, as one can see by the higher doping level in the middle graphene layer in Fig. 4.3.

In order to calculate the graphene doping as a function of the number of MoSSe layers for this new type of structure, we again use the capacitor model considering one of the outer graphene layers together with the middle graphene layer. The middle graphene layer

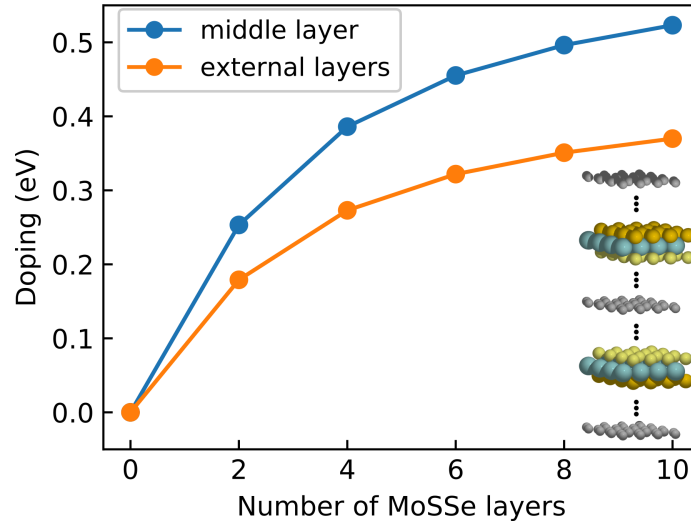


Figure 4.3: Doping level in the middle and external graphene layers of the structure illustrated in the inset, as a function of the number of MoSSe layers, as calculated using the capacitor model.

is expected to support twice the charge density of each of the outer graphene layers, due to charge conservation. Hence, the energy difference between the outer and inner graphene layers, instead of $2\epsilon_F$ in Eq. (4.3), becomes $(1 + \sqrt{2})\epsilon_F$. Consequently, we obtain

$$\epsilon_F = \frac{-1 - \sqrt{2} + \sqrt{3 + 2\sqrt{2} + 4aN^2\Delta_{\text{MoSSe}}}}{2aN}. \quad (4.6)$$

Considering only two layers of MoSSe with opposing dipole orientations, the calculated loss spectrum and the induced densities corresponding to the plasmon excitations are shown Fig. 4.4. There are now three doped graphene layers, which reflect in three branches of the loss function, of which are two symmetric and one antisymmetric for $q = 0.01 \text{ \AA}^{-1}$. Besides the addition of a new acoustic mode in the spectrum, there are no major differences in the plasmon energies in comparison to the first case presented in Fig. 4.2. The reason for this similarity can be understood by noticing that the actual doping level in the inner graphene layer is about 250 meV, which is not significantly larger than the bilayer graphene-MoSSe heterostructure, which exhibits a doping level of $\approx 200 \text{ meV}$.

We now compare the more extreme cases for both bilayer graphene heterostructure with 5 layers of MoSSe and trilayer graphene heterostructures with five layers of MoSSe sandwiched between each of the graphene layer. The results are shown in Fig. 4.5. In the latter, the new symmetric plasmon branch that appears achieves much higher frequencies, namely up to 0.5 eV, without undergoing damping, which is simply a consequence of the increased doping of the middle layer. As indicated in the figure, the highest energy plasmon mode actually extends into the Landau damping regime of the outer graphene layers without suffering losses, which can be explained by the fact that the plasmon is localized in the middle graphene layer and thus cannot excite electron-hole pairs in the outer ones. Furthermore, the upper limit of the achieved plasmon energy is determined mainly by the point where the plasmon branch enters the Landau damping regime that

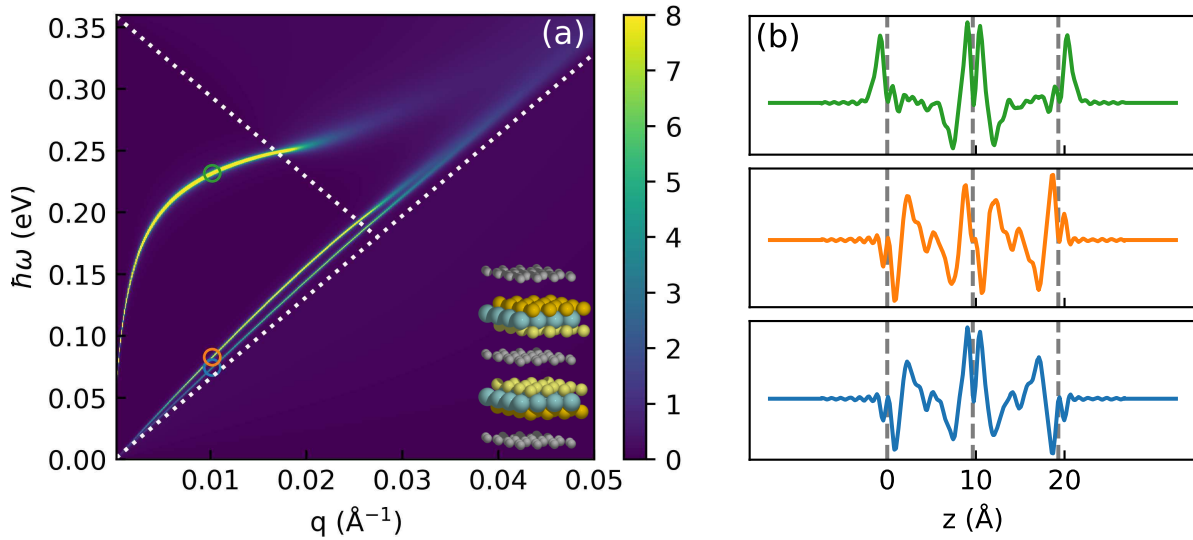


Figure 4.4: (a) Loss function for the heterostructure illustrated in the inset, composed by two external graphene layers ($\epsilon_F = 0.18$ eV), one middle graphene layer ($\epsilon_F = 0.25$ eV) and two layers of MoSSe with opposite orientation with relaxation rate of $\hbar\omega = 1$ meV. White dashed lines delimit the region of Landau damping of the plasmon modes. (b) The induced densities for $q = 0.01$ \AA^{-1} now present three modes: two symmetric and one antisymmetric. The vertical dashed grey lines represent the graphene layers positions.

is directly related to the Fermi energy of the layer where it is localized. The Landau damping region for graphene is defined as the continuum in which plasmons quickly decay into electron-hole pairs. These transitions are of the intraband type, where $v_F q > \omega$, and interband type, $\omega > v_F q$ and $\omega + v_F q > 2k_{F,i}$ in which v_F is the Fermi velocity and $k_{F,i}$ the Fermi momentum of the i 'th graphene layer. The layer dependence of the Fermi momentum originates from the non-uniform doping of the graphene layers which leads to different Landau damping regimes. Therefore, our results show that in such a MoSSe/graphene van der Waals heterostructure, it is possible to obtain plasmon energies that are among the highest ever reported [144, 134, 107, 145], without the need of external doping sources, such as electrostatic gates or chemical functionalization.

A second type of heterostructure, also with three layers of graphene, but assuming all MoSSe layers with the same dipole orientation (see the inset in Fig. 4.6(a)) is now investigated. In this case, only the outer graphene layers become doped, while the middle graphene layer stays undoped. While the structure is, in principle, similar to the previously discussed bilayer graphene-MoSSe heterostructure, the addition of the middle graphene layer adds significant losses in the form of Landau damping for all frequencies and momenta. As a consequence, the optical mode is quenched in contrast to the acoustic mode, which survives. The origin of the difference in losses of the two modes is found in the associated electric fields of the modes: the optical mode is associated with a large in-plane electric field on the middle undoped graphene layer which excites many electron hole pairs, whereas the acoustic mode exhibits an out-of-plane electric field that cannot excite electron-hole pairs and is therefore not susceptible to the losses introduced by the middle

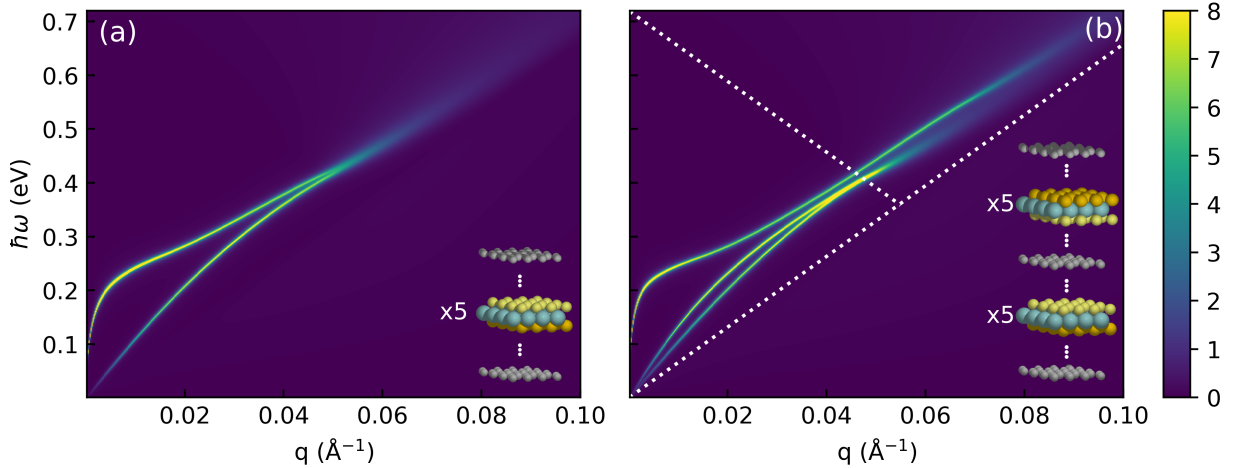


Figure 4.5: Comparison between loss functions of heterostructures composed by (a) five layers of MoSSe encapsulated by two graphene layers ($\epsilon_F = 0.36$ eV, $\hbar\omega = 1$ meV) and (b) ten layers of MoSSe, divided into two stacks of MoSSe with opposite orientations, intercalated and encapsulated by three layers of graphene ($\epsilon_{F,\text{external}} = 0.36$ eV and $\epsilon_{F,\text{middle}} = 0.50$ eV). White dashed lines delimit the Landau damping region of the plasmon modes of the outer graphene layers.

graphene layer. The quenching of the optical mode can be further increased, as verified in Fig. 4.6(b) by adding a second undoped graphene layer to the middle of the heterostructure. These results show that it is possible to selectively engineer the quenching of optical modes in graphene heterostructures, leaving the acoustic modes as the only propagating modes in the structure. Graphene acoustic plasmons have a linear dispersion at long wavelengths and much higher electromagnetic field confinement due to the considerably smaller wavelength if compared to the optical mode[146, 147, 148, 149]. These characteristics are optimal for applications that require ultra sensitivity [150]. Other treatments of acoustic plasmons that go beyond the RPA show that the crossover between collisionless and hydrodynamic regimes can renormalize the plasmon group velocity [151] and as such can be an important effect to include. This, however, goes beyond the scope of our present work.

This work opens new possibilities of engineering plasmons in p-n junctions that are created from the stacking of Janus TMDs using graphene leads. Besides MoSSe, we believe that it is possible to use other Janus TMDs that have greater dipole shifts to create plasmons with even higher energies than those presented here, without any type of external doping. The relation between doping and the optical plasmon energy can be expanded for small momenta to yield (see Supporting Information)

$$\hbar\omega_{\text{opt}} \approx e\sqrt{\frac{N\Delta_{\text{Janus}}}{2\pi\epsilon_0}}\sqrt{q}, \quad (4.7)$$

where the energy of the optical mode is derived in the non-retarded limit ($q \gg \sqrt{\epsilon}\omega/c$) with the Fermi energy defined as in Eq. 4.4 for the structure presented in the inset of Fig. 4.1. One verifies that the optical plasmon energy directly depends on the dipole shift Δ_{Janus} of the Janus TMD that compose the structure, but is not affected by the screening

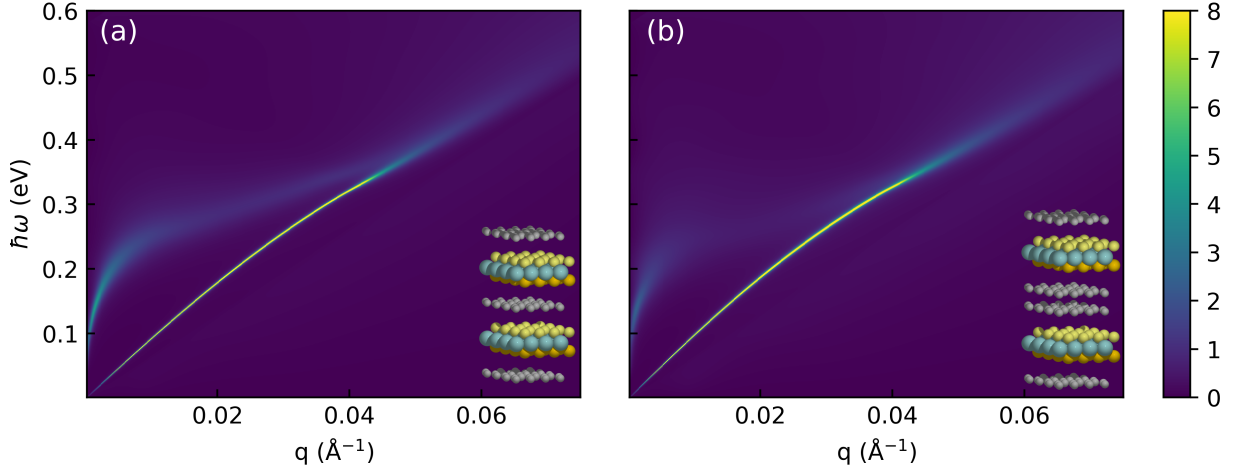


Figure 4.6: Loss function for two MoSSe layers encapsulated by graphene ($\epsilon_F = 0.29$ eV, $\hbar\omega = 1$ meV) where we add one (a) and two (b) layer(s) of graphene in the middle of the heterostructure.

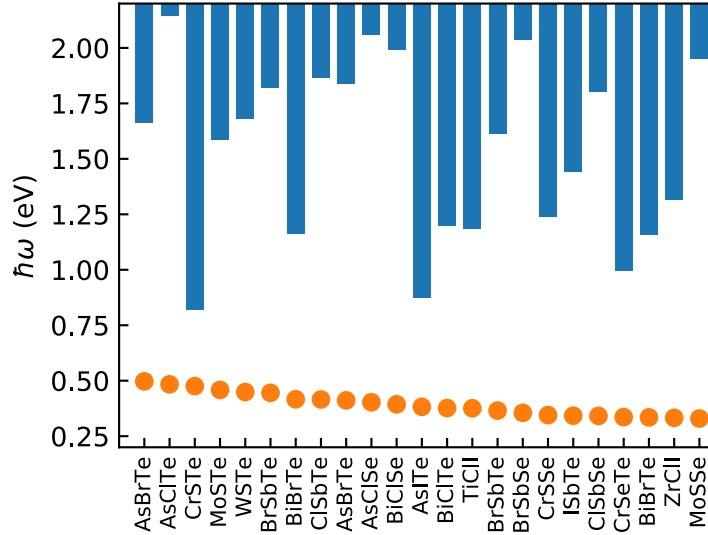


Figure 4.7: Optical plasmon energies (orange circles) for different Janus TMDs composing the structure sketched on the inset of Fig. 4.5 (a), for $q = 0.001$ Å. Electron-hole pair continuum for each material is shown by blue bars.

of the dielectric environment, due to compensating effects between the additional screening and increased charge density in graphene, which also scales with ϵ .

Optical plasmon energies, as calculated with Eq. (4.7) for a heterostructure with five TMD layers encapsulated by graphene (see sketch in Fig. 4.5 (a)) at $q = 0.001$ Å are shown in Fig. 4.7, for several stable Janus materials. All these Janus materials are highly thermodynamically stable, and are dynamically stable with respect to rearrangements of the atoms that preserve the layered character of the material. We stress this because the dynamic stability analysis will not take into account the ability of the materials 'roll up' due to the different sizes of X- and Y- atoms[152]. The Janus materials have higher Δ_{Janus} as compared to MoSSe, [89] which could improve the p-n junction properties by enhancing the plasmon energies. Equation (4.7) is expected to break down when the plasmon energies approach the band gap, which would thus screen and reduce the plasmon energy. In Fig.

(4.7), the band gap and the onset of interband transitions are indicated by blue bars, which shows that, for some materials, the band gap is considerably large as compared to the unscreened plasma frequency. Based on this, we propose Arsenic Tellurium Chloride (AsTeCl) as the most promising Janus few layer system for plasmonics, with a high band gap energy.

Stark shift of excitons and trions in two-dimensional materials

5.1 Motivation

Much of the interest in materials as TMDs and phosphorene lies in their optoelectronic properties, because in contrast with graphene, these materials are naturally semiconductors with highly tunable band structures. One of the most important features ubiquitous to all of these few-layer semiconductors is reduced Coulomb screening, which greatly increases the binding energies of excitons and trions (i.e. charged excitons) [43, 45, 46, 47] when compared to their bulk counterparts. Such strongly bound excitons dominate the photophysical properties and, in principle, enable the investigation of the effect of strong electric fields applied to these systems without intervening electron-hole dissociation.¹ In fact, such tightly bound excitonic complexes in 2D materials have also brought to the fore the possibility of driving a charged exciton with an in-plane field, which would open a new avenue for possible applications in future opto-electronic devices.

The effect of an applied (static) electric field F on the energy states of hydrogen- and helium-like atoms has been known for decades [153]. Such a field modifies the spectrum according to the so-called Stark shift, which for states with s -symmetry, is given by

$$\Delta E = \frac{1}{2}\alpha F^2 + \frac{1}{24}\beta F^4 + \dots \quad (5.1)$$

The $\alpha(\beta)$ factor is known as (hyper)polarizability. Since excitons and trions exhibit hydrogen- and helium ion-like electronic states, respectively, one expects to observe such an energy shift in the optical spectrum when an electric field is applied in semiconductor materials as well. The absorption of excitons with p -symmetry is not optically allowed by selection rules (except in two-photon experiments [154]), therefore, one can use Eq.

¹As a matter of fact, the electric field potential diverges to $-\infty$ as $r \rightarrow \infty$, therefore, any electron-hole pair is expected to eventually dissociate. However, in the cases of strongly bound electrons and holes investigated here, such dissociation is unlikely to occur before the exciton decays, since it would require tunneling through a thick potential barrier, provided by the strong electron-hole interaction potential.

(5.1) for the description of the excitonic Stark effect, where odd-order correction terms are zero due to symmetry. Moreover, corrections with orders higher than F^4 are usually negligibly small. Indeed, this hyperpolarizability correction to the Stark shift is usually neglected in the study of excitons under applied fields. Nevertheless, such fourth order corrections to ΔE have been theoretically investigated by perturbation theory for several atoms and ions, [155] where they are found to be of the order of $10^{-7} \text{ cm}^4/\text{kV}^3$. Hyperpolarizabilities two orders of magnitude higher than this were experimentally observed in highly excited states of the Rydberg series of Ba, Ca and Rb atoms [156, 157, 158]. The tightly bound neutral and charged excitons in 2D materials, where binding energies are much higher than those in previously known cases of excitons in, e.g., heterostructures of III-V and II-VI semiconductors, provides the opportunity to experimentally investigate the (hyper)polarizabilities of e-h complexes.

In this chapter, we theoretically investigate the effect of an applied in-plane electric field on the energy states of excitons and trions in 2D materials, namely, TMDCs and n -layer black phosphorus (n -BP). Energy shifts as a function of the field, as numerically calculated within the effective mass framework and the Wannier-Mott picture, are fitted to the Stark shift expression Eq. (5.1). We consider not only the case of suspended 2D materials, but also the situations where the material is deposited on a substrate, or encapsulated by another material, which are the most studied cases. The effect of the dielectric screening from the environment on the exciton and trion Stark shifts in these three situations is discussed. Trions are found to be robust against applied fields. Particularly, trions in n -BP barely undergo changes in their binding energies and wave functions if the field is applied along the zigzag direction of the black-phosphorus lattice, which supports the idea that even high applied fields may successfully drive charged excitons across the phosphorene plane with no e-h dissociation. Trion Stark shifts in all cases investigated here turn out to be not properly described by the quadratic Stark shift, as is usual for neutral excitons in these materials, but rather by a quartic shift, where hyperpolarizabilities are found to be even higher than those already experimentally observed in excited states of atoms [156, 157, 158], as we will demonstrate in further details in what follows.

5.2 Theoretical model

The exciton Hamiltonian in a system composed by a substrate, a 2D semiconductor layer (where the e-h pair resides), and a capping layer, with dielectric constants ϵ_1 , ϵ_2 and ϵ_3 , respectively, in the presence of an external electric field \vec{F} , has been given in previous papers [159] and is presented here for the sake of completeness:

$$H_{exc} = \frac{p^2}{2\mu} + V_{eh}(r) + e\vec{F} \cdot \vec{r}, \quad (5.2)$$

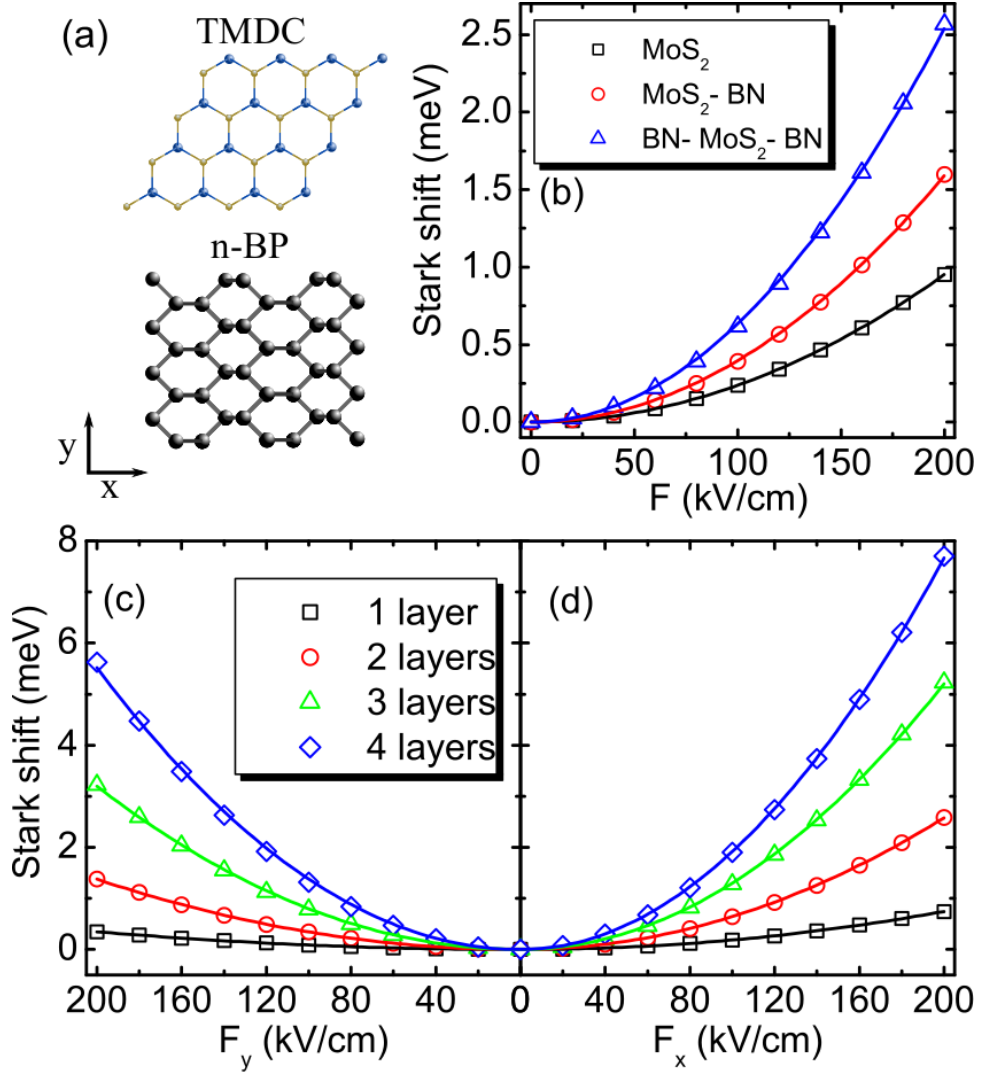


Figure 5.1: (a) Sketch of the top view of the TMDC and BP crystal lattices, along with the direction of F_x and F_y components of the applied field. Stark shift of exciton binding energies in (b) MoS₂, in the suspended, on-substrate, and encapsulated cases, and in (c,d) suspended phosphorene with different numbers of layers. In the latter, results are shown for fields applied in the y - and x -direction respectively (c,d). The values of polarizability (fitting parameters) are presented in Table 5.1.

where $\mu_X^{-1} = m_e^{-1} + m_h^{-1}$, $\vec{r} = \vec{r}_e - \vec{r}_h$ is the e-h relative coordinate, and the interaction potential between particles i and j ($i, j = e$ or h) is assumed to be of the Rytova-Keldysh form [50, 51] which takes account of the screening by the environment surrounding the semiconductor layer

$$V_{ij} = \frac{e^2}{4\pi\epsilon_0(\epsilon_1 + \epsilon_3)\rho_0} \left[H_0 \left(\frac{\rho}{\rho_0} \right) - Y_0 \left(\frac{\rho}{\rho_0} \right) \right] \quad (5.3)$$

with $\rho = |\vec{r}_i - \vec{r}_j|$, $\rho_0 = \epsilon_2 d / (\epsilon_1 + \epsilon_3)$, and d the thickness of the semiconductor layer.

For trions, we will consider only the negatively charged case, since the results for the positively charged case are similar due to the nearly identical electron and hole effective masses. Such a trion is described as two electrons with mass m_e located at \vec{r}_e and $\vec{r}_{e'}$, and a hole with mass m_h located at \vec{r}_h . This six-coordinate system is not easy to implement in

numerical calculations and it is thus necessary to find a new coordinates set in which some coordinates are removed by the use of symmetry arguments [160]. Relevant coordinates for this new system are the trion center-of-mass (CM)

$$\vec{R}_t = \frac{m_e \vec{r}_e + m_e \vec{r}_{e'} + m_h \vec{r}_h}{M}, \quad (5.4)$$

where $M = 2m_e + m_h$, the previously defined relative coordinate for an e-h pair forming an exciton \vec{r} , and the relative coordinate between the CM of this exciton and the extra electron

$$\vec{u} = \vec{r}_{e'} - \frac{m_e \vec{r}_e + m_h \vec{r}_h}{m_e + m_h}. \quad (5.5)$$

Within the coordinates system $(\vec{R}_t, \vec{u}, \vec{r})$, the trion Hamiltonian reads

$$H_t = \frac{p_r^2}{2\mu_X} + \frac{p_u^2}{2\mu_T} - V_{eh}(\vec{r}) + V_{ee'}(\vec{u} - \gamma_h \vec{r}) - V_{e'h}(\vec{u} + \gamma_e \vec{r}) - e\vec{F} \cdot \vec{r} - e\vec{F} \cdot \vec{u}, \quad (5.6)$$

where $\mu_T^{-1} = m_e^{-1} + (m_e + m_h)^{-1}$, and $\gamma_e = 1 - \gamma_h = m_e/(m_e + m_h)$. Since the electron-electron and electron-hole interaction potentials, namely $V_{ee'}(\vec{u} - \gamma_h \vec{r})$, $V_{eh}(\vec{r})$, and $V_{e'h}(\vec{u} + \gamma_e \vec{r})$, respectively, do not depend on the trion CM coordinate \vec{R}_t , this coordinate is completely separable from the Hamiltonian Eq. (5.6), so that the Hamiltonian associated to the trion CM motion due to the applied field $H_{CM} = P_{CM}^2/2M + e\vec{F} \cdot \vec{R}_t$ is left out from H_t . Finally, the Schrödinger equation for the exciton (trion) with Hamiltonian Eq. (5.2) [Eq. (5.6)] is numerically solved by an imaginary time evolution method. [161]

5.3 Results and discussion

We have calculated the electric field dependence of the exciton binding energies for four different TMDCs, namely MoS₂, MoSe₂, WS₂, and WSe₂, as well as for n -BP with up to $n = 4$ layers, for which effective masses and dielectric constants are found in the literature [89, 120, 162]. Results for TMDCs are independent of the field direction, whereas for the anisotropic case of n -BP, we consider fields applied in both x and y directions defined in Fig. 5.1(a). Substrate and capping layers are assumed to be made of BN. The calculated Stark shift for the case of MoS₂ is shown in Fig. 5.1(b). As the system becomes more screened by the environment, the electron-hole interaction weakens and, as a consequence, the Stark shift in the encapsulated case is more pronounced as compared to the others. As for n -BP, a similar screening effect occurs, and it is even more pronounced as the number of layers n increase, as shown for the suspended case in Fig. 5.1(c,d). The Stark shift in n -BP is stronger for fields applied in the x -direction direction, where effective masses are lower. Curves in Fig. 5.1(b-d) are fits of the numerical data (symbols) with the usual expression for Stark shift, which assumes a quadratic dependence on the field, i.e. Eq. (5.1) for $\beta = 0$. Polarizabilities for the four previously mentioned TMDCs and n -BP

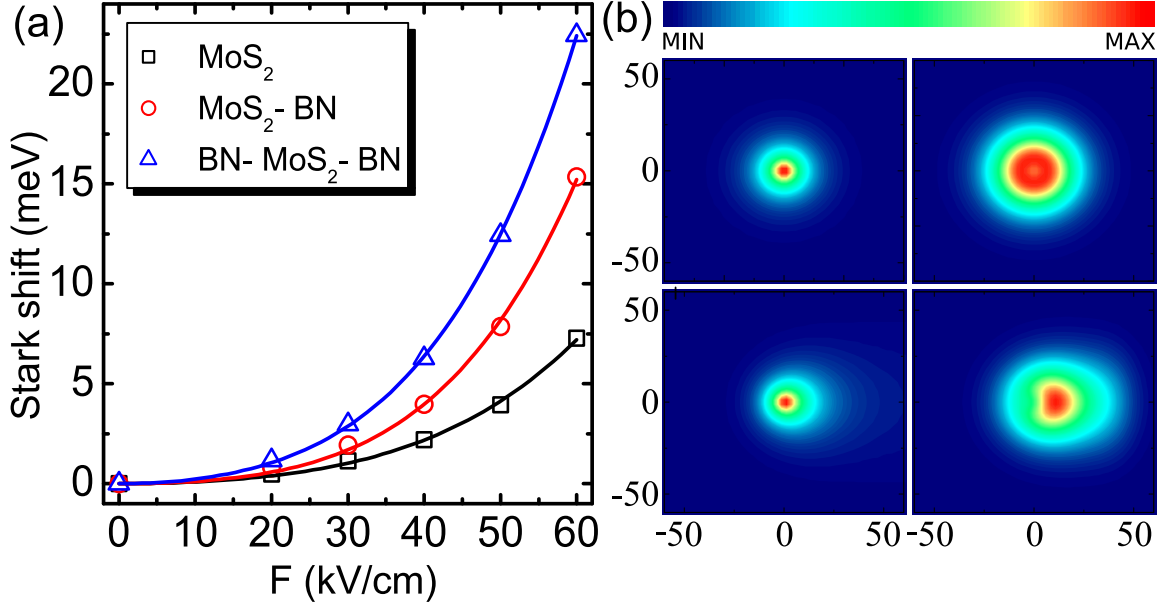


Figure 5.2: (a) Numerically obtained (symbols) field dependence of the trion binding energy E_b in monolayer MoS₂ in the suspended case, on a BN substrate, and encapsulated by BN. The values of polarizability and hyperpolarizability (fitting parameters for the curves) are presented in Table 5.3. (b) Contour map of the square modulus of the trion wave function in suspended MoS₂ with x and y axis in angstrom. The square modulus of the wave function is calculated by an integral in the coordinates that are not variables in each plot. The left (right) column represents the exciton's (trion's) center of mass wave function in the absence of electric field in the first row, and for a $F = 60$ kV/cm field applied in the x -direction in the second row. The colour scale goes from 0 (blue, MIN) to 0.012 (red, MAX).

are summarized in Table 5.1, for all cases of dielectric environment. For the suspended case, they agree well with previously reported values [159, 163, 164, 165], while results presented here extend this data to the supported (on substrate) and encapsulated cases. In fact, the polarizability for encapsulated WSe₂ obtained here is in good agreement with recent experimental results, [166] where it was observed to be $(1 \pm 0.2) \times 10^{-6}$ Dm/V, which, converted to the units used here, yields $\approx 10.393 \times 10^{-5}$ meV cm²/kV², very close to the 10.027×10^{-5} meV cm²/kV² we obtain in our calculations (see Table 5.1).

Trion binding energies in the absence of electric fields for TMDCs and n -BP, as obtained by our numerical method, are summarized in Table 5.2. In fact, results for some TMDCs and few layer BP, in the suspended case and supported by a substrate, have been already reported by different papers in the literature. [43, 47, 160, 167] Our results are in good agreement with these previously reported values and are shown here for completeness. Differences of a few meV are mostly due to the use of slightly different parameters such as effective masses and dielectric constants. Table 5.2 also provides results for the case where these materials are encapsulated by BN. The interest in trions in such encapsulated 2D semiconductors has been recently enhanced by experimental reports [168, 44] showing that such encapsulation renders trion peaks sharper and clearer in photoluminescence experiments.

The trion Stark shift as a function of the applied field in MoS₂ is shown in Fig. 5.2(a),

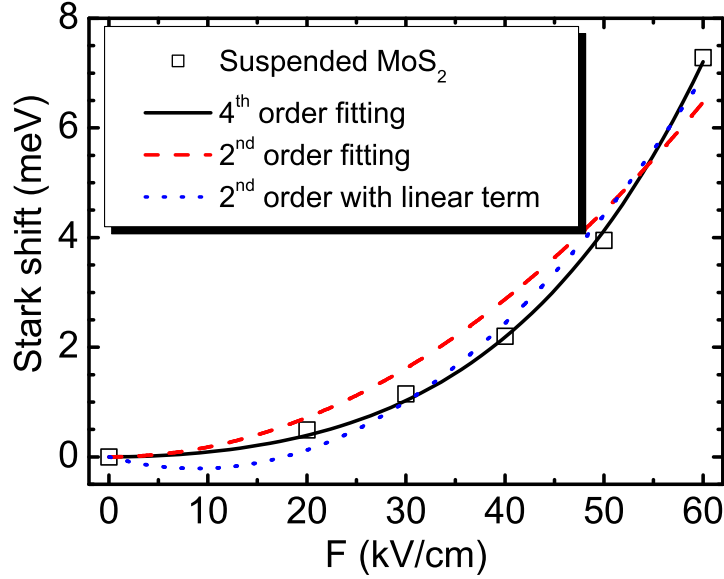


Figure 5.3: Comparison between fitting curves of second and fourth order corrections (lines) to the numerically obtained Stark shift of trions (symbols) in suspended MoS₂. For the former, two cases are considered, namely with and without a first order term in the fitting expression (see manuscript).

assuming the same three cases of dielectric environments as in the previous discussion. Qualitatively similar results are found for the other TMDCs. It becomes evident that for trions, the assumption of a quadratic shift is no longer valid, as reasonable fittings shown by the curves in Fig. 5.2(a) are only obtained if one assumes a significant contribution of the hyperpolarizability (quartic) term, i.e. $\beta \neq 0$ in Eq. (5.1). Moreover, Fig. 5.2 illustrates the robustness of the trion state, where no dissociation is observed even for fields up to 60 kV/cm, as shown by the wave function projections in Fig. 5.2(b), for the suspended MoS₂ case. Notice that, in the absence of fields (top row of panels), the excitonic and trionic components of the wave function are both circularly symmetric, and the latter exhibits a minimum at $r = 0$, as a consequence of electron-electron repulsion. The 60 kV/cm field induces a deformation of these distributions, as observed in the bottom row of panels, but they remain concentrated around the origin, representing the absence of trion dissociation.

Trion binding energies for TMDCs in Table 5.2 are all of similar magnitude, namely ≈ 30 meV in the suspended case. Moreover, in the absence of electric field, their radii are all ≈ 25 Å (see e.g. Fig. 5.2(b), top right panel). With this information, one can estimate the voltage drop at the trion radius, for the highest electric field considered here ($F = 60$ kV/cm), as ≈ 15 meV, which is still around half of the binding energy of the trion. The fact that the voltage drop at the radius of the trion wave function is still smaller than its binding energy explains why the trion is still stable and robust for applied fields up to this value for all TMDC investigated here.

In order to illustrate better the need to fit the trion Stark shift by a fourth (rather than second) order expression, we show the data for suspended MoS₂ in Fig. 5.3 (symbols)

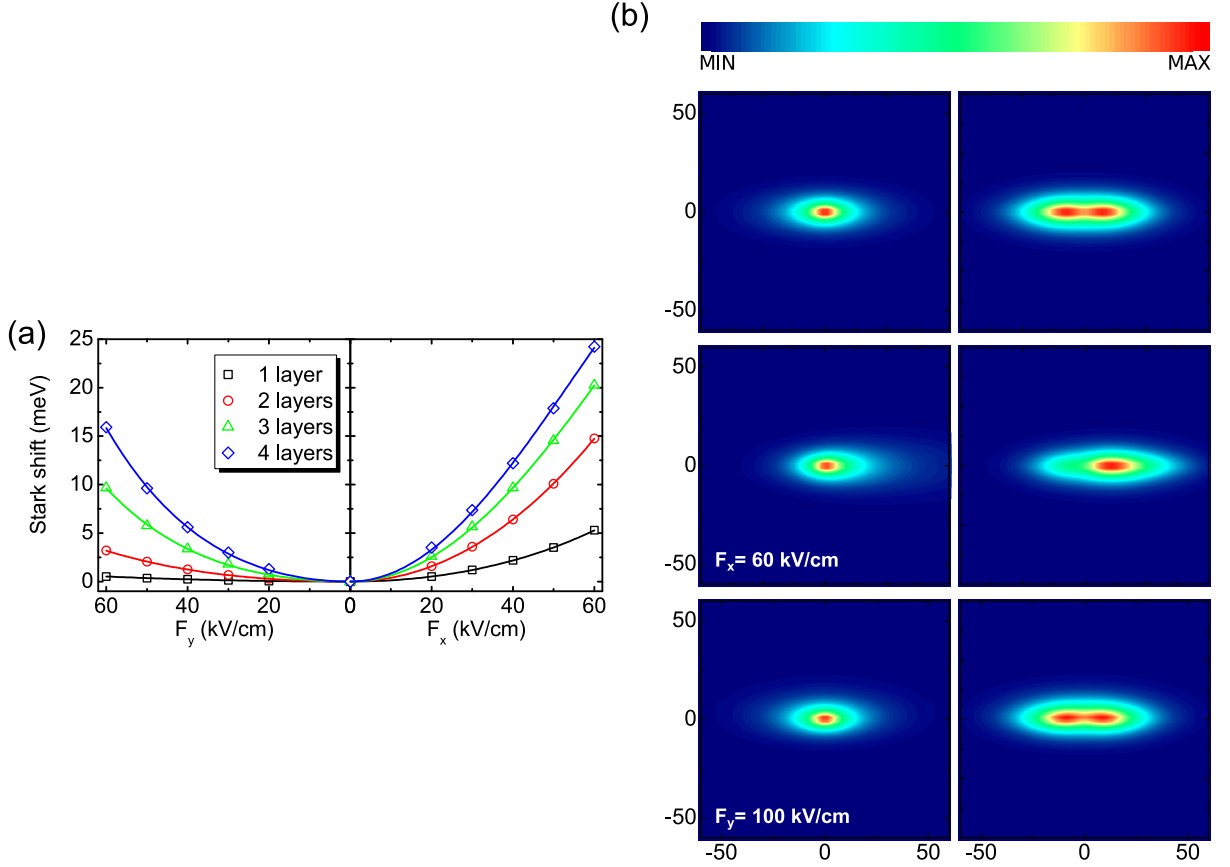


Figure 5.4: (a) Numerically obtained (symbols) electric field dependence of the binding energy E_b for trions in phosphorene with different number of layers for a field applied in the y (left) and x (right) directions. The values of polarizability and hyperpolarizability (fitting parameters for the curves) are presented in Table 5.3. (b) Countour maps of the square modulus of the trion wave function in suspended monolayer BP with x and y axis in angstrom. The left (right) column represents the exciton (trion) center-of-mass wave function in the absence of electric field in the first row, and for a $F = 60$ kV/cm field applied in the x -direction in the second row, and $F = 100$ kV/cm applied in the y -direction in the third row. The colour scale ranges from 0 (blue, MIN) to 0.018 (red, MAX)

along with second and fourth order fitting functions. For the former, we assume two possibilities: a purely quadratic function, i.e. $\Delta E = \frac{1}{2}\alpha F^2$ and a function with an additional linear term (so that the vertex of the parabola is allowed to move away from $F = 0$), $\Delta E = \gamma F + \frac{1}{2}\alpha F^2$. A fitting algorithm, based on damped least-squares method, is used to find the optimal parameters γ and α that fit the numerical data. It is clear that the purely quadratic function (dashed) is off the numerical data. The function with $\gamma \neq 0$ provides better fitting, but still not as good as the quartic one, and it is physically less reasonable, since such a linear correction must come from an intrinsic exciton dipole moment in the direction of application of the field (see e.g. Ref. [169]), which is clearly absent for the ground state excitons discussed here. The best fitting is clearly obtained with the fourth order expression, with a coefficient of determination $R^2 = 0.99996$, which can be compared to the second order expressions with and without the linear term, which

have $R^2 = 0.98166$ and $R^2 = 0.95484$, respectively.² The fact that R^2 in the fourth order fitting is already very close to 1 (with 10^{-5} precision) already suggests that higher order corrections are definitely negligible. Similar results are observed for any other material investigated here.

As for trions in n -BP, Stark shifts for the suspended case are shown in Fig. 5.4(a) for a field applied along the y and x directions. Similar to the TMDC cases, the shift requires a non-zero β in Eq. (5.1) to properly capture the data. Moreover, polarizabilities in this case are direction dependent, as a manifestation of the band structure anisotropy in this material [170, 113]. Hyperpolarizabilities of n -BP, as well as those for TMDCs, are all summarized in Table 5.3.

Most importantly, trions in n -BP are found to be very robust against applied fields, especially in the y (zigzag) direction. The shift observed as F_y reaches 60 kV/cm is negligibly small for suspended monolayer BP (see black squares in Fig. 5.4(a), left panel), and even for higher fields, of the order of 100 kV/cm, the shift still barely reaches ≈ 1 meV. This is a consequence of the fact that, although the trion binding energy in this case is still of the same order of magnitude as those found in TMDC and n -BP, its wave function dramatically spreads along the x -direction but negligibly along the y -direction, due to mass anisotropy, [5, 162, 113] as one verifies in Fig. 5.4(b), top row of panels. If the field is applied along the x -direction, the wave function is clearly deformed, see Fig. 5.4(b), middle row. However, even if a field as high as 100 kV/cm is applied along the y -direction, no significant change is observed in the wave function, as one can see by comparing bottom and top rows in Fig. 5.4(b). In fact, the width of the wave function along y -direction is ≈ 10 Å (see Fig. 5.4(b), top right panel), so that the potential drop at this point with a $F_y = 100$ kV/cm field is still only ≈ 10 meV, much smaller than the trion binding energy. With such a robust trion state, one could use high in-plane electric fields to move the charged exciton across the material plane without dissociating the excitonic complex, which has implications for possible energy transfer applications.

²An exact fit in this algorithm leads to $R^2 = 1$.

Table 5.1: Exciton polarizabilities for monolayer TMDC and n -BP in the suspended, on substrate and encapsulated cases, in units of 10^{-5} meVcm²/kV². Results inside (outside) the brackets for n -BP are for electric fields applied in x and y directions, respectively.

Material	Suspended	Exciton	
		On substrate	Encapsulated
MoS ₂	2.378	4.218	6.340
MoSe ₂	2.679	4.259	6.532
WS ₂	2.916	6.034	9.079
WSe ₂	3.492	6.116	10.027
1-BP	1.861 (0.871)	3.628 (1.575)	6.162 (2.598)
2-BP	6.447 (3.440)	10.045 (5.293)	14.020 (7.632)
3-BP	13.005 (7.992)	17.477 (11.397)	21.670 (15.684)
4-BP	19.169 (13.786)	23.467 (18.947)	27.194 (25.581)

Table 5.2: Trion binding energies (in meV), in the absence of electric fields, for monolayer TMDCs and n -BP in the suspended case, on a BN substrate, and encapsulated by BN, respectively.

Material	Suspended	On substrate	Encapsulated
MoS ₂	32.12	21.59	15.83
MoSe ₂	32.00	22.60	17.18
WS ₂	34.49	23.60	15.94
WSe ₂	33.15	21.93	16.14
1-BP	51.77	32.65	22.82
2-BP	27.99	19.34	14.56
3-BP	19.18	13.97	11.10
4-BP	15.15	11.69	9.80

Table 5.3: Trions polarizabilities / hyperpolarizabilities for monolayer TMDCs and n -BP in the suspended, on substrate and encapsulated cases, in units of 10^{-5} meVcm²/kV² / 10^{-7} meVcm⁴/kV⁴. Results in the middle (bottom) for n -BP are for electric fields applied in x and y directions, respectively.

Material	Suspended	Trion	
		On substrate	Encapsulated
MoS ₂	85.323 / 3.191	109.317 / 8.698	218.286 / 11.227
MoSe ₂	86.599 / 4.291	107.716 / 9.753	204.923 / 12.334
WS ₂	122.784 / 3.210	204.131 / 7.512	376.108 / 7.879
WSe ₂	86.809 / 5.742	234.332 / 8.575	411.367 / 8.480
1-BP	127.649 / 0.531	211.017 / 1.513	320.562 / 1.827
2-BP	393.922 / 0.436	508.718 / -0.0239	621.182 / -1.029
3-BP	639.373 / -2.151	718.239 / -2.863	792.271 / -3.699
4-BP	843.204 / -4.810	884.925 / -5.218	928.280 / -5.724
1-BP	14.128 / 0.0088	23.747 / 0.0637	36.950 / 0.242
2-BP	68.796 / 0.548	90.252 / 1.606	116.473 / 2.967
3-BP	164.476 / 2.863	201.404 / 4.778	250.760 / 6.188
4-BP	278.942 / 4.475	330.894 / 5.836	391.636 / 6.559

Concluding remarks

In chapter 2, we have proposed a classical (electrostatic) model for describing the electron-hole interaction potential in few layer TMDCs and their vdW heterostructures. With its transfer matrix-like structure, the method developed here is easily manipulated to calculate the screened electron-hole interaction potential in any combination of TMDCs layers and substrates for either spatially direct (intra-layer) or indirect (inter-layer) excitons. We verify this method correctly converges to the standard effective potential of Rytova and Keldysh in the limit of small thickness and large differences between dielectric constants. It also yields the ordinary Coulomb potential for an inter-layer electron-hole interaction if the layers in which the charges are confined are separated by a large distance. A comparison between the proposed electrostatic transfer matrix method and the recently developed ab initio-based quantum electrostatic heterostructure (QEH) method [52] is performed, where semi-quantitative agreement between results from both methods is demonstrated. Results from the ETM method are demonstrated to be very accurate for the exciton ground state and reasonably accurate (up to 0.01 eV error) for excited states, in comparison with those from the QEH method. Worse accuracy is observed in the case of inter-layer excitons in hetero-bilayers, where the difference in ground state binding energies may reach 0.02 eV ($\approx 8\%$). Nevertheless, by paying the price of somewhat lower accuracy, the ETM method requires much lower computational overhead and an input based only on the dielectric constants of the bulk parent materials, in contrast to the input required by DFT-based methods. By providing a facile and inexpensive means of obtaining the interaction potential, the ETM proves to be a powerful tool for calculations where interactions between charges need to be computed numerous times, such as in diffusion and variational Monte Carlo based techniques for studying many-particle states, such as trions and biexcitons in 2D materials. [56, 72, 13, 171, 167]

Inter-layer exciton binding energies are found to be around ≈ 250 -300 meV, which is substantially lower than those of intra-layer excitons in monolayer TMDCs, ≈ 550 meV. [47] This result is of importance in the interpretation of photoluminescence peaks in experiments involving vdW heterostructures. We have also successfully applied our method in the modelling of recently observed Coulomb engineered exciton states in WS_2

capped by few-layer graphene. [55]

We believe the fast and highly adjustable method developed here will be of use for verification, interpretation or prediction of excitonic peak positions in future experiments involving light-matter interactions in vdW stacks of layered materials. Work using the ETM approach to investigate excitons in inter-layer situations is currently under way.

In chapter 3, we have introduced an extension of the quantum electrostatic heterostructure (QEH) model for calculating dielectric properties of 2D van der Waals heterostructures. The QEH model combines first-principles derived properties (electronic susceptibilities, phonons, Born charges, effective masses) of the individual 2D layers with an efficient classical scheme to couple the layers via the Coulomb interaction, thereby avoiding the technical issues related to the full quantum mechanical description of lattice mismatched interfaces. The new developments allow for inclusion of screening from (polar) phonons, homogeneous bulk substrates/capping layers, and free carriers in the conduction or valence bands of doped semiconducting layers. The importance of including these screening sources for realistic modeling of plasmons, polar phonons and excitons was illustrated by several examples. The extensions significantly expand the applicability of the QEH model towards more experimentally relevant systems.

The basic structure of the QEH model remains unchanged and the new developments only affect the construction of the dielectric building blocks of the individual layers. The new QEH model is available as a standalone package written entirely in Python and comes with an improved user interface and a library of dielectric building blocks for the most common 2D materials. The QEH code and library is available at <https://pypi.org/project/qeh>.

In chapter 4, we have investigated the effect of the intrinsic electric dipole across a Janus TMD layer on the doping level and plasmonic frequencies of graphene layers within a Janus TMD/graphene van der Waals heterostructure. A strong variation of the doping level in the graphene layers is observed as the number of TMD layers increase, especially for a graphene layer placed in between two Janus TMD stacks with opposite orientation. On the other hand, by aligning the orientation of the two Janus TMD stacks encapsulating a few layer graphene sheet, the graphene optical plasmonic modes become quenched, whereas acousting plasmon states stay visible up to very high energies. These results suggest that stacking Janus TMD layers intercalated with graphene is an efficient way to select graphene plasmon modes and provide strong doping without the need of external sources, such as electrostatic gates and chemical adsorption. Although results are obtained here specifically for the case of MoSSe, a systematic study of several other potentially synthesizable Janus structures indicate that other Janus monolayers, with larger band gaps and larger out-of-plane dipole moments than MoSSe, might be even more efficient for doping and controlling graphene plasmons.

Finally, in chapter 5, we have investigated the effect of an applied in-plane electric field on the binding energies of excitons and trions in TMDCs and few layer BP. Binding

energies and polarizabilities are shown to depend on the dielectric environment, but in all investigated cases, excitons and trions binding energies are high enough to allow for their stability in strong fields. Trions in monolayer BP are demonstrated to be especially robust against fields applied along the zigzag (y , in Fig. 5.1(a)) direction, so that even fields as strong as 100 kV/cm produce Stark shifts of only ≈ 1 meV and no visible effects on the wavefunction. Moreover, the usual quadratic dependence on the field intensity is demonstrated to be insufficient to describe the Stark shift in all materials investigated here. Fitting results with a fourth order function yields hyperpolarizabilities of the same order of magnitude as those observed, e.g., for excited states in Ba, Ca, and Rb atoms [156, 157, 158]. We believe the results found here will stimulate not only future experimental investigations on the hyperpolarizabilities of trions in 2D materials, but also the development of devices based on transport of charged excitons in 2D materials by applied in-plane electric fields in the near future.

Appendices

Effective mass model

To demonstrate that the two situations: (1) an electron interacting with the system and (2) a free electron with an effective mass are equivalent, we study a system under a periodic potential representing a crystalline structure. The eigenfunctions of the Hamiltonian are $\psi(\vec{r}) = e^{i\vec{k}\cdot\vec{r}}u_k(\vec{r})$, where $u_k(\vec{r})$ is the Bloch function and it has the same periodicity as the system. So the *Schrodinger* equation becomes

$$\left(-\frac{\hbar^2}{2m}\nabla^2 + V(\vec{r})\right)e^{i\vec{k}\cdot\vec{r}}u_k(\vec{r}) = \left[\frac{1}{2m}(\vec{p} + \hbar\vec{k})^2 + V(\vec{r})\right]e^{i\vec{k}\cdot\vec{r}}u_k(\vec{r}) = E(\vec{k})e^{i\vec{k}\cdot\vec{r}}u_k(\vec{r}). \quad (\text{A.1})$$

We can use perturbation theory to obtain the eigenvalues of the Hamiltonian

$$(H_0 + H_1)u_k(\vec{r}) = E(\vec{k})u_k(\vec{r}), \quad (\text{A.2})$$

where

$$H_0 = \frac{1}{2m}(\vec{p})^2 + V(\vec{r}), \quad (\text{A.3})$$

and

$$H_1 = \frac{\hbar}{m}\vec{p}\cdot\vec{k} + \frac{\hbar^2 k^2}{2m}. \quad (\text{A.4})$$

in which H_0 is the unperturbed contribution with $u_0^n(\vec{r})$ eigenstates of energy $E^n(0)$.

Therefore, the eigenvalues of the system Hamiltonian up to second order correspond to

$$E^n(\vec{k}) = E^n(0) + \langle u_0^n | H_1 | u_0^n \rangle + \sum_{l \neq n} \frac{|\langle u_0^l | H_1 | u_0^n \rangle|^2}{E^n(0) - E^l(0)}, \quad (\text{A.5})$$

where we make the necessary substitutions

$$E^n(\vec{k}) = E^n(0) + \frac{\hbar^2 k^2}{2m} + \frac{\hbar^2}{m^2} \sum_{l \neq n} \frac{|\vec{k} \cdot \langle u_0^l | \vec{p} | u_0^n \rangle|^2}{E^n(0) - E^l(0)}. \quad (\text{A.6})$$

If we analyse the last equation, it can be written as

$$E^n(\vec{k}) = E^n(0) + \frac{\hbar^2}{2} \vec{k} \cdot \left(\frac{1}{m_{\alpha\beta}^*} \right) \cdot \vec{k}, \quad (\text{A.7})$$

where $m_{\alpha\beta}^*$ is the effective mass tensor that is given by

$$m_{\alpha\beta}^* = \left[\frac{\delta_{\alpha\beta}}{m} + \frac{2}{m^2} \sum_{l \neq n} \frac{\langle u_0^l | p_\alpha | u_0^n \rangle \langle u_0^l | p_\beta | u_0^n \rangle}{E^n(0) - E^l(0)} \right], \quad (\text{A.8})$$

which can be directional dependent to represent different structural directions of the system.

Finally, if we expand an energy band $E_n(\vec{k})$ in Taylor series around $k = 0$,

$$E_n(\vec{k}) = E^n(0) + \sum_{\alpha} \frac{\partial E^n}{\partial k_{\alpha}} k_{\alpha} + \frac{1}{2} \sum_{\alpha, \beta} \frac{\partial^2 E^n}{\partial k_{\alpha} \partial k_{\beta}} k_{\alpha} k_{\beta} \quad (\text{A.9})$$

and compare it to Eq. A.7, we obtain

$$\frac{1}{2} \sum_{\alpha, \beta} \frac{\partial^2 E^n}{\partial k_{\alpha} \partial k_{\beta}} k_{\alpha} k_{\beta} = \frac{1}{2} \vec{k} \cdot \left(\frac{\partial^2 E^n}{\partial k_{\alpha} \partial k_{\beta}} \right) \cdot \vec{k} = \frac{\hbar^2}{2} \vec{k} \cdot \left(\frac{1}{m_{\alpha\beta}^*} \right) \cdot \vec{k}, \quad (\text{A.10})$$

which gives

$$\frac{\partial^2 E^n}{\partial k_{\alpha} \partial k_{\beta}} = \frac{\hbar^2}{m_{\alpha\beta}^*}. \quad (\text{A.11})$$

Hence, the effective mass is a tensor that depends on the \vec{k} direction and its matrix elements are defined by

$$m_{\alpha\beta}^* = \frac{\hbar^2}{\frac{\partial^2 E^n}{\partial k_{\alpha} \partial k_{\beta}}}, \quad (\text{A.12})$$

such that it is possible to obtain the effective mass from the energy band structure of the system.

Lattice polarizability: Derivation

The electrostatic energy of a material with a macroscopic polarization density \mathbf{P} in a macroscopic electric field \mathbf{E} is given by [91]

$$\Phi^{electrostatic} = -\Omega_{\text{cell}} \mathbf{E} \cdot \mathbf{P} = -A_{\text{cell}} \mathbf{E} \cdot \mathbf{P}^{2D} \quad (\text{B.1})$$

where $\mathbf{P}^{2D} = L_{\text{cell}} \mathbf{P}$ is the macroscopic 2D polarization density and Ω_{cell} , A_{cell} , L_{cell} is the volume, area and height of the simulation cell, respectively. The total energy is then given by

$$\Phi = \frac{1}{2} \sum_{ai,bj} U_{ai} C_{ai,bj} U_{bj} - A_{\text{cell}} \mathbf{E} \cdot \mathbf{P}^{2D} \quad (\text{B.2})$$

where $C_{ai,bj}$ is the force constant matrix, U_{ai} is the displacement of an atom a from its equilibrium position along a cartesian direction $i \in \{x, y, z\}$. The resulting equations of motion are

$$m_a \frac{d^2}{dt^2} U_{ai} = -\frac{d\Phi}{dU_{ai}} = -\sum_{bj} C_{ai,bj} U_{bj} + A_{\text{cell}} \mathbf{E} \cdot \frac{d\mathbf{P}^{2D}}{dU_{ai}}. \quad (\text{B.3})$$

The Born charges are defined as

$$Z_{i,aj} = \frac{A_{\text{cell}}}{|e|} \left. \frac{dP_i^{2D}}{dU_{aj}} \right|_{E_j=0} \quad (\text{B.4})$$

where e is the elementary charge. The Born charges are in practice calculated using the formalism of the modern theory of polarization[86, 87]. The polarizability α_{ij} describes the response to a macroscopic electric field

$$\alpha_{ij} = \frac{dP_i^{2D}}{dE_j} \approx \left. \frac{dP_i^{2D}}{dE_j} \right|_{U=0} + \sum_{ak} \left. \frac{\partial P_i^{2D}}{\partial U_{ak}} \right|_{E_j=0} \frac{dU_{ak}}{dE_j} = \alpha_{ij}^{\text{el}} + \alpha_{ij}^{\text{lp}} \quad (\text{B.5})$$

where α_{ij}^{el} and α_{ij}^{lp} are the electronic and lattice polarization contributions to the total polarizability, respectively, and are given by

$$\alpha_{ij}^{\text{el}} = \left. \frac{dP_i^{2\text{D}}}{dE_j} \right|_{U=0} \quad (\text{B.6})$$

$$\alpha_{ij}^{\text{lp}} = \sum_{ak} \left. \frac{\partial P_i^{2\text{D}}}{\partial U_{ak}} \right|_{E_j=0} \frac{dU_{ak}}{dE_j} = \frac{|e|}{A_{\text{cell}}} \sum_k Z_{i,ak} \frac{dU_{ak}}{dE_j}. \quad (\text{B.7})$$

The electronic polarizability is calculated using linear response theory and is converted into a 2D dielectric building block[52]. The lattice polarizability is derived by solving the equation of motion for the atoms Eq. (B.4) and inserting in Eq. (B.7)

$$m_a(-i\omega)^2 U_{ai} = - \sum_{bj} C_{ai,bj} U_{bj} + \sum_j |e| Z_{j,ai} E_j \quad (\text{B.8})$$

$$\Leftrightarrow \frac{dU_{ai}}{dE_j} = \left[|e| (\underline{\underline{C}} - \omega^2 \underline{\underline{M}})^{-1} \underline{\underline{Z}}^T \right]_{ai,j} \quad (\text{B.9})$$

where we have changed to a matrix formalism with $C_{ai,bj} \rightarrow \underline{\underline{C}}$ having dimensions $3N_a \times 3N_a$ by combining indices ai and bj where N_a is the number of atoms in the unit cell and $Z_{i,aj} \rightarrow \underline{\underline{Z}}$ having dimensions $3 \times 3N_a$ by combining indices aj and $\underline{\underline{M}}$ is a $3N_a \times 3N_a$ matrix containing the atomic masses in blocks of 3. The phonon contribution to the lattice polarization become

$$\underline{\underline{\alpha}}^{\text{lp}} = \frac{|e|^2}{A_{\text{cell}}} \underline{\underline{Z}} (\underline{\underline{C}} - \omega^2 \underline{\underline{M}})^{-1} \underline{\underline{Z}}^T. \quad (\text{B.10})$$

In practice to avoid having to calculate a matrix inversion for each frequency we rewrite the expression above

$$(\underline{\underline{C}} - \omega^2 \underline{\underline{M}})^{-1} = \underline{\underline{M}}^{-1/2} (\underline{\underline{D}} - \omega^2)^{-1} \underline{\underline{M}}^{-1/2} \quad (\text{B.11})$$

$$= \underline{\underline{M}}^{-1/2} \left(\sum_i \frac{\mathbf{d}_i \mathbf{d}_i^T}{d_i - \omega^2} \right) \underline{\underline{M}}^{-1/2} \quad (\text{B.12})$$

where $\underline{\underline{D}} = \underline{\underline{M}}^{-1/2} \underline{\underline{C}} \underline{\underline{M}}^{-1/2}$ is the well known dynamical matrix and where we in the last line used to spectral theorem and expanded the dynamical matrix in its eigenrepresentation where \mathbf{d}_i is an eigenvector and d_i is the corresponding eigenvalue. In practice this means that instead of performing a matrix inversion for every single frequency we only have to perform one diagonalization at the start of the calculation. A finite relaxation time due to the presence of scattering mechanisms can be introduced in the above expression by letting $\omega^2 \rightarrow \omega^2 - i\gamma\omega$ ([91], p. 401).

A dielectric building block contains the monopole and dipole moments of the interacting density-density response function and it is therefore necessary to relate these to the polarizability derived above. The out-of-plane polarizability can be directly related to the non-interacting density response function

$$\alpha_{zz} E_z = P_z = \int dz z \delta n_{\text{ind}}(z) = - \int dz dz' z \chi^0(z, z') z' E_z = -\chi_{\text{dipole}}^0 E_z \quad (\text{B.13})$$

where the minus sign arises from the difference between electric potential and potential energy and from which it is clear that $\chi_{\text{dipole}}^0 = -\alpha_{zz}$. The in-plane direction has to be handled differently since the total potential has the form $\phi(x, z) = \phi(z)e^{-iqx}$

$$P_x = \alpha_{xx}E_x \Rightarrow \frac{dP_x}{dx} = \alpha_{xx} \frac{d^2}{dx^2} \phi(x, z) \quad (\text{B.14})$$

$$n_{\text{ind}} = -q^2 \alpha_{xx} \phi \quad (\text{B.15})$$

from which it is clear that $\chi_{\text{monopole}}^0 = -q^2 \alpha_{xx}$.

Since the existing dielectric building block describes the interacting electronic density response function χ_{el} and the phononic polarizability is related to the non-interacting density response function $\chi_{0,\text{lp}}$ it is not possible to directly sum the two. It is necessary first to undo the Dyson equation of the electronic response to get $\chi_{0,\text{el}}$, sum the non interacting density response functions, and solve the Dyson equation again for the fully interacting response function, i.e.

$$\chi_{0,\text{el}} = \frac{\chi_{\text{el}}}{1 + V_q \chi_{\text{el}}} \quad (\text{B.16})$$

$$\chi_{0,\text{tot}} = \chi_{0,\text{el}} + \chi_{0,\text{lp}} \quad (\text{B.17})$$

$$\chi_{\text{tot}} = \frac{\chi_{0,\text{tot}}}{1 - V_q \chi_{0,\text{tot}}} \quad (\text{B.18})$$

where V_q is the Coulomb potential and χ_{tot} is the interacting density response function including both the electronic and phononic contribution. The chosen Coulomb potential depends on whether the monopole or the dipole response is treated. For the monopole we assume that charges are sufficiently localized within the 2D material such that the potential can be described by the well known 2D Coulomb potential $V_q = \frac{2\pi}{q}$ (in atomic units, a.u.). For the dipole we assume that the dipoles are described by an ideal 2D dipole Coulomb potential $V_q = 2\pi$ (a.u.) which would be valid if charges are sufficiently localized in the 2D material. Additionally we also assume that the induced density from the phononic response has the same profile as the electronic induced densities. In practice this is not a serious limitation as the results of the QEH model doesn't depend severely on the actual profile employed.

To summarize, we have shown that the polarizability originating from the lattice polarization in a polar material can be described by

$$\underline{\underline{\alpha}}^{\text{2D,ph}} = \frac{|e|^2}{A_{\text{cell}}} \underline{\underline{Z}}^T \underline{\underline{M}}^{-1/2} \left(\sum_i \frac{\mathbf{d}_i \mathbf{d}_i^T}{d_i - \omega^2 - i\gamma\omega} \right) \underline{\underline{M}}^{-1/2} \underline{\underline{Z}}. \quad (\text{B.19})$$

which can be converted into a density response function and included in the existing dielectric building blocks using a procedure of undoing and solving the Dyson equation.



Doping of anisotropic 2D semi-conductors

The intraband response of a doped anisotropic semi-conductor, such as BP, can be mapped to the calculation of the response of an isotropic material with scaled effective masses and momenta. This can be shown by writing taking the substitutions

$$\begin{aligned} q_x^2 &= \sqrt{\frac{m_x^*}{m_y^*}} \tilde{q}_x^2, & q_y^2 &= \sqrt{\frac{m_y^*}{m_x^*}} \tilde{q}_y^2, \\ k_x^2 &= \sqrt{\frac{m_x^*}{m_y^*}} \tilde{k}_x^2, & k_y^2 &= \sqrt{\frac{m_y^*}{m_x^*}} \tilde{k}_y^2, \end{aligned} \quad (\text{C.1})$$

and inserting into the expression for the density response function

$$\chi_0^{\text{2DEG}}(q_x, q_y, m_x, m_y) = \frac{1}{2\pi^2} \int_0^{E(\mathbf{k}) < E_F} \frac{f_0(E(\mathbf{k})) - f_0(E(\mathbf{k} + \mathbf{q}))}{\hbar\omega + E(\mathbf{k}) - E(|\mathbf{k} + \mathbf{q}|) + i\eta} d^2\mathbf{k}, \quad (\text{C.2})$$

where $E(\mathbf{k}) = \frac{\hbar^2 k_x^2}{2m_x^*} + \frac{\hbar^2 k_y^2}{2m_y^*}$ is the dispersion relation for an anisotropic material. Upon substitution the dispersion relations reads

$$E(\mathbf{k}) = \frac{\hbar^2 \tilde{k}_x^2 + \hbar^2 \tilde{k}_y^2}{2\sqrt{m_x^* m_y^*}} = \frac{\hbar^2 \tilde{k}^2}{2m^*} = E_{\text{iso}}(\tilde{\mathbf{k}}; m^*) \quad (\text{C.3})$$

$$E(\mathbf{k} + \mathbf{q}) = \frac{\hbar^2 (\tilde{k}_x + \tilde{q}_x)^2 + \hbar^2 (\tilde{k}_y + \tilde{q}_y)^2}{2\sqrt{m_x^* m_y^*}} = E_{\text{iso}}(\tilde{\mathbf{k}} + \tilde{\mathbf{q}}; m^*) \quad (\text{C.4})$$

where $E_{\text{iso}}(\tilde{\mathbf{k}}; m^*)$ is the isotropic energy dispersion relation and $m^* = \sqrt{m_x^* m_y^*}$. Inserting into the density response function

$$\chi_0^{\text{2DEG}}(q_x, q_y, m_x, m_y) = \frac{1}{2\pi^2} \int_0^{E_{\text{iso}}(\tilde{\mathbf{k}}; m^*) < E_F} d^2\tilde{\mathbf{k}} \frac{f_0(E_{\text{iso}}(\tilde{\mathbf{k}}; m^*)) - f_0(E_{\text{iso}}(\tilde{\mathbf{k}} + \tilde{\mathbf{q}}; m^*))}{\hbar\omega + E_{\text{iso}}(\tilde{\mathbf{k}}; m^*) - E_{\text{iso}}(\tilde{\mathbf{k}} + \tilde{\mathbf{q}}; m^*) + i\eta} \quad (\text{C.5})$$

$$= \chi_0^{\text{2DEG, isotropic}} \left((m_x^*/m_y^*)^{1/4} q_x, (m_y^*/m_x^*)^{1/4} q_y, m^* \right) \quad (\text{C.6})$$

where we have used that the volume element is invariant with respect to the integral transform i.e. $dk_x dk_y = d\tilde{k}_x d\tilde{k}_y$. From here it is clear that the anisotropic response can be mapped to an isotropic response with an effective mass given by the geometric mean $m^* = \sqrt{m_x^* m_y^*}$ at a scaled momentum $\tilde{\mathbf{q}}$.



Plasmon propagation lengths

Here, we derive an approximate expression for the plasmon propagation length defined as the imaginary part of the plasmons wavenumber. We start from the Poisson equation with a total potential $\phi^{tot} = \phi^{ext} + \phi^{ind}$

$$\nabla^2 \phi^{ind} = -4\pi \rho_{ind} = -4\pi \hat{\chi}_0 \phi^{tot}, \quad (\text{D.1})$$

where $\hat{\chi}_0$ is the non-interacting density response function interpreted as an integral operator. We then use that for self-sustained oscillations $\phi^{ext} = 0 \Rightarrow \phi^{tot} = \phi^{ind}$, which turns the Poisson equation into an eigenvalue problem

$$\nabla^2 \phi^{ind} = -4\pi \hat{\chi}_0 \phi^{ind}. \quad (\text{D.2})$$

Assume a planewave form of the induced potential $\phi^{ind} = \phi_q^{ind}(z)e^{iqx}$ where q is the wave number

$$(-q^2 + \partial_z^2) \phi_q^{ind} = -4\pi \hat{\chi}_q^0 \phi_q^{ind}. \quad (\text{D.3})$$

Now separate q into a real and imaginary part

$$q = q_0 + \delta, \quad (\text{D.4})$$

where $\text{Im}(q_0) = 0$ and $\text{Re}(\delta) = 0$ and assume

$$\begin{aligned} \phi_{q_0+\delta}^{ind} &\approx \phi_{q_0}^{ind} \\ \hat{\chi}_{q_0+\delta}^0 &\approx \hat{\chi}_{q_0}^0, \end{aligned} \quad (\text{D.5})$$

then

$$\begin{aligned} -(q_0 + \delta)^2 + \partial_z^2 \phi_{q_0}^{ind} &= -4\pi \hat{\chi}_{q_0}^0 \phi_{q_0}^{ind} \\ (-\delta^2 - q_0^2 - 2q_0\delta + \partial_z^2) \phi_{q_0}^{ind} &= -4\pi \hat{\chi}_{q_0}^0 \phi_{q_0}^{ind}. \end{aligned} \quad (\text{D.6})$$

Now, realise that $-q_0^2 + \partial_z^2 = -4\pi V_{q_0}^{-1}$ where $V_{q_0}^{-1}$ is the inverse Coulomb kernel evaluated at q_0

$$\begin{aligned}
(-\delta^2 - 2q_0\delta - 4\pi V_{q_0}^{-1})\phi_{q_0}^{ind} &= -4\pi \hat{\chi}_{q_0}^0 \phi_{q_0}^{ind} \\
(-\delta^2 - 2q_0\delta)\phi_{q_0}^{ind} &= 4\pi (V_{q_0}^{-1} - \hat{\chi}_{q_0}^0) \phi_{q_0}^{ind} \\
(-\delta^2 - 2q_0\delta)\phi_{q_0}^{ind} &= 4\pi V_{q_0}^{-1} (1 - V_{q_0} \hat{\chi}_{q_0}^0) \phi_{q_0}^{ind} \\
(4\pi)^{-1}(-\delta^2 - 2q_0\delta)\phi_{q_0}^{ind} &= V_{q_0}^{-1} \hat{\epsilon}_{q_0} \phi_{q_0}^{ind},
\end{aligned} \tag{D.7}$$

where $\hat{\epsilon}_{q_0} = 1 - V_{q_0} \hat{\chi}_{q_0}^0$ is the dielectric function. This equation can be solved for δ by finding eigenvalues λ_{q_0} of the RHS operator

$$\begin{aligned}
V_{q_0}^{-1} \hat{\epsilon}_{q_0} \phi_{q_0}^{ind} &= \lambda_{q_0} \phi_{q_0}^{ind} = (4\pi)^{-1}(-\delta^2 - 2q_0\delta)\phi_{q_0}^{ind} \\
\delta &= q_0 \left(1 \pm \sqrt{1 - \frac{4\pi \lambda_{q_0}}{q_0^2}} \right)
\end{aligned} \tag{D.8}$$

Since $\text{Im}(\lambda) > 0$ and choosing the conventional branch cut of the complex square root $[-\infty, 0]$ we use the negative branch of the solution to ensure an exponentially decaying plane wave

$$\delta = q_0 \left(1 - \sqrt{1 - \frac{4\pi \lambda_{q_0}}{q_0^2}} \right). \tag{D.9}$$

We have to find solutions where $\text{Re}(\delta) = 0$, which will indicate the self-consistent solutions. In practice, this is done by sampling frequencies and momenta on a fine grid and looking for solutions satisfying the $\text{Re}(\delta) = 0$. This allows us to calculate the normalized propagation length of the self-sustained oscillations

$$F = \frac{\text{Re}(q)}{\text{Im}(q)} = \frac{q_0}{\text{Im}(\delta)} = -\frac{1}{\text{Im}\left(\sqrt{1 - \frac{4\pi \lambda_{q_0}}{q_0^2}}\right)} \tag{D.10}$$

which can be interpreted as a figure of merit for polaritonic/plasmonic applications.

Layer thicknesses and effective masses stored in the QEH internal library are tabulated in Table E.1.

Name	Thickness	phonons	e_mass	h_mass
BN	3.33 Å	available		
H-CrO2		available	0.875 m _e	1.442 m _e
H-CrS2		available	0.872 m _e	0.883 m _e
H-CrSe2		available	0.936 m _e	0.955 m _e
H-CrTe2		available	0.855 m _e	0.9 m _e
H-GeO2		available		
H-HfO2		available		
H-HfS2		available	1.255 m _e	2.653 m _e
H-HfSe2		available	1.351 m _e	3.108 m _e
H-HfTe2		available	1.722 m _e	0.612 m _e
H-MoO2		available	0.419 m _e	0.764 m _e
H-MoS2	6.1511 Å	available	0.427 m _e	0.53 m _e
H-MoSe2	6.45 Å	available	0.492 m _e	0.583 m _e
H-MoTe2	6.982 Å	available	0.493 m _e	0.597 m _e
H-SnO2		available	0.282 m _e	7.291 m _e
H-SnS2		available	0.656 m _e	0.482 m _e
H-TiO2		available		
H-TiS2		available	0.0 m _e	2.585 m _e
H-TiSe2		available	0.0 m _e	1.654 m _e
H-TiTe2		available		
H-WO2		available	0.346 m _e	0.781 m _e
H-WS2	6.1615 Å	available	0.328 m _e	0.336 m _e
H-WSe2	6.48 Å	available	0.389 m _e	0.355 m _e
H-ZrO2		available		
H-ZrS2		available	2.881 m _e	2.2 m _e
H-ZrSe2		available	0.0 m _e	1.973 m _e

H-ZrTe2		available	0.0 m _e	1.136 m _e
T-GeO2			0.344 m _e	3.79 m _e
T-GeS2			0.689 m _e	1.289 m _e
T-HfO2			3.18 m _e	2.767 m _e
T-HfS2	5.837 Å		2.372 m _e	0.249 m _e
T-HfSe2	6.159 Å		2.286 m _e	0.159 m _e
T-NiO2			2.007 m _e	0.0 m _e
T-NiS2			0.403 m _e	0.617 m _e
T-NiSe2				
T-PbO2			0.45 m _e	29.088 m _e
T-PbS2			0.895 m _e	4.138 m _e
T-PdO2			3.069 m _e	0.0 m _e
T-PdS2			0.565 m _e	2.247 m _e
T-PdSe2			0.337 m _e	0.635 m _e
T-PdTe2	5.118 Å			
T-PtO2			3.288 m _e	28.946 m _e
T-PtS2	5.0389 Å		0.682 m _e	1.546 m _e
T-PtSe2	5.0813 Å		0.463 m _e	2.893 m _e
T-PtTe2	5.2209 Å		0.251 m _e	0.359 m _e
T-SnO2			0.355 m _e	4.491 m _e
T-SnS2	5.9 Å		0.779 m _e	2.034 m _e
T-SnSe2	6.132 Å		0.744 m _e	0.402 m _e
T-TiO2			1.214 m _e	3.834 m _e
T-ZrO2			1.384 m _e	3.017 m _e
T-ZrS2	5.813 Å		2.04 m _e	0.26 m _e
T-ZrSe2	6.128 Å		1.928 m _e	0.158 m _e
graphene	3.35 Å			

- L. S. R. Cavalcante, A. Chaves, B. Van Duppen, F. M. Peeters, and D. R. Reichman. *Electrostatics of electron-hole interactions in van der Waals heterostructures*. Phys. Rev. B **97**, 125427 (2018). DOI: 10.1103/PhysRevB.97.125427

PHYSICAL REVIEW B **97**, 125427 (2018)

Electrostatics of electron-hole interactions in van der Waals heterostructures

L. S. R. Cavalcante,¹ A. Chaves,^{1,*} B. Van Duppen,² F. M. Peeters,^{1,2} and D. R. Reichman³

¹*Departamento de Física, Universidade Federal do Ceará, Caixa Postal 6030, Campus do Pici, 60455-900 Fortaleza, Ceará, Brazil*

²*Department of Physics, University of Antwerp, Groenenborgerlaan 171, B-2020 Antwerp, Belgium*

³*Department of Chemistry, Columbia University, New York, New York 10027, USA*



(Received 1 November 2017; revised manuscript received 24 February 2018; published 21 March 2018)

The role of dielectric screening of electron-hole interaction in van der Waals heterostructures is theoretically investigated. A comparison between models available in the literature for describing these interactions is made and the limitations of these approaches are discussed. A simple numerical solution of Poisson's equation for a stack of dielectric slabs based on a transfer matrix method is developed, enabling the calculation of the electron-hole interaction potential at very low computational cost and with reasonable accuracy. Using different potential models, direct and indirect exciton binding energies in these systems are calculated within Wannier-Mott theory, and a comparison of theoretical results with recent experiments on excitons in two-dimensional materials is discussed.

DOI: [10.1103/PhysRevB.97.125427](https://doi.org/10.1103/PhysRevB.97.125427)

-
- L. S. R. Cavalcante, D. R. da Costa, G. A. Farias, D. R. Reichman, and A. Chaves. *Stark shift of excitons and trions in two-dimensional materials*. Phys. Rev. B **98**, 245309 (2018). DOI: 10.1103/PhysRevB.98.245309

PHYSICAL REVIEW B **98**, 245309 (2018)

Stark shift of excitons and trions in two-dimensional materials

L. S. R. Cavalcante,^{1,*} D. R. da Costa,¹ G. A. Farias,¹ D. R. Reichman,² and A. Chaves^{1,†}

¹*Departamento de Física, Universidade Federal do Ceará, Caixa Postal 6030, Campus do Pici, 60455-900 Fortaleza, Ceará, Brazil*

²*Department of Chemistry, Columbia University, New York, New York 10027, USA*



(Received 4 July 2018; revised manuscript received 18 November 2018; published 20 December 2018)

The effect of an external in-plane electric field on neutral and charged exciton states in two-dimensional (2D) materials is theoretically investigated. These states are argued to be strongly bound, so that electron-hole dissociation is not observed up to high electric field intensities. Trions in the anisotropic case of monolayer phosphorene are demonstrated to be especially robust under electric fields, so that fields as high as 100 kV/cm yield no significant effect on the trion binding energy or probability density distribution. Polarizabilities of excitons are obtained from the parabolicity of numerically calculated Stark shifts. For trions, a fourth order Stark shift is observed, which enables the experimental verification of hyperpolarizability in 2D materials, as observed in the highly excited states of the Rydberg series of atoms and ions.

DOI: [10.1103/PhysRevB.98.245309](https://doi.org/10.1103/PhysRevB.98.245309)

- Chen, Shao-Yu and Lu, Zhengguang and Goldstein, Thomas and Tong, Jiayue and Chaves, Andrey and Kunstmann, Jens and Cavalcante, L S R and Woźniak, Tomasz and Seifert, Gotthard and Reichman, D R and Taniguchi, Takashi and Watanabe, Kenji and Smirnov, Dmitry and Yan, Jun. *Luminescent Emission of Excited Rydberg Excitons from Monolayer WSe₂*. *Nano Letters* **19**, 4, 2464-2471 (2019). DOI: 10.1021/acs.nanolett.9b00029

Luminescent Emission of Excited Rydberg Excitons from Monolayer WSe₂

Shao-Yu Chen,[†] Zhengguang Lu,^{‡,§} Thomas Goldstein,[†] Jiayue Tong,[†] Andrey Chaves,^{||} Jens Kunstmann,[⊥] L. S. R. Cavalcante,^{||} Tomasz Woźniak,^{⊥,#} Gotthard Seifert,[⊥] D. R. Reichman,[∇] Takashi Taniguchi,[○] Kenji Watanabe,[○] Dmitry Smirnov,[‡] and Jun Yan^{*,†,Ⓢ}

[†]Department of Physics, University of Massachusetts, Amherst, Massachusetts 01003, United States

[‡]National High Magnetic Field Laboratory, Tallahassee, Florida 32310, United States

[§]Department of Physics, Florida State University, Tallahassee, Florida 32306, United States

^{||}Departamento de Física, Universidade Federal do Ceará, Caixa Postal 6030, Campus do Pici, 60455-900 Fortaleza, Ceará, Brazil

[⊥]Theoretical Chemistry, Department of Chemistry and Food Chemistry & Center for Advancing Electronics Dresden, TU Dresden, 01062 Dresden, Germany

[#]Department of Theoretical Physics, Wrocław University of Science and Technology, Wyb. Wyspiańskiego 27, 50-370 Wrocław, Poland

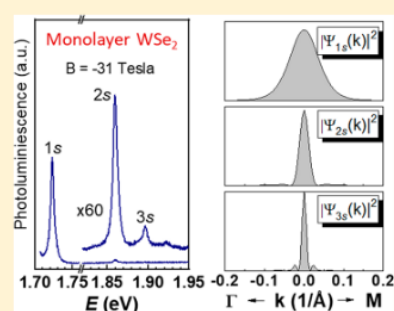
[∇]Department of Chemistry, Columbia University, New York, New York 10027, United States

[○]National Institute of Materials Science, 1-1 Namiki, Tsukuba, Ibaraki 305-0044, Japan

Supporting Information

ABSTRACT: We report the experimental observation of radiative recombination from Rydberg excitons in a two-dimensional semiconductor, monolayer WSe₂, encapsulated in hexagonal boron nitride. Excitonic emission up to the 4s excited state is directly observed in photoluminescence spectroscopy in an out-of-plane magnetic field up to 31 T. We confirm the progressively larger exciton size for higher energy excited states through diamagnetic shift measurements. This also enables us to estimate the 1s exciton binding energy to be about 170 meV, which is significantly smaller than most previous reports. The Zeeman shift of the 1s to 3s states, from both luminescence and absorption measurements, exhibits a monotonic increase of the g-factor, reflecting nontrivial magnetic-dipole-moment differences between ground and excited exciton states. This systematic evolution of magnetic dipole moments is theoretically explained from the spreading of the Rydberg states in momentum space.

KEYWORDS: Rydberg exciton, tungsten diselenide, diamagnetic shift, Zeeman shift, magnetic dipole moment



- L. S. R. Cavalcante, M. N. Gjerding, Andrey Chaves, and K. S. Thygesen. *Enhancing and Controlling Plasmons in Janus MoSSe–Graphene Based van der Waals Heterostructures*. *The Journal of Physical Chemistry C* **123**, 26, 16373-16379 (2019). DOI: 10.1021/acs.jpcc.9b04000

Enhancing and Controlling Plasmons in Janus MoSSe–Graphene Based van der Waals Heterostructures

L. S. R. Cavalcante,^{*,†} M. N. Gjerding,^{‡,§} Andrey Chaves,[†] and K. S. Thygesen^{*,‡,§}

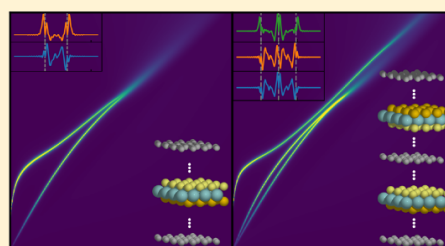
[†]Departamento de Física, Universidade Federal do Ceará, Caixa Postal 6030, Campus do Pici, 60455-900 Fortaleza, Ceará, Brazil

[‡]CAMD, Department of Physics, Technical University of Denmark, 2800 Kgs. Lyngby, Denmark

[§]Center for Nanostructured Graphene (CNG), Technical University of Denmark, Ørsted's Plads, Bldg. 345C, 2800 Kgs. Lyngby, Denmark

Supporting Information

ABSTRACT: We explore the use of MoSSe Janus layers, which possess an intrinsic electric dipole caused by their out-of-plane structural asymmetry, to selectively dope graphene embedded inside a heterostructure without the need of external sources (such as electrostatic gates or chemical functionalization) in order to engineer graphene plasmons. Using the quantum-electrostatic heterostructure method, we demonstrate that through the control of the plasmon energy via the doping level and the hybridization of plasmons in different layers, we can reach graphene plasmon energies up to 0.5 eV or selectively quench certain (symmetric) modes by Landau damping. The possibility of using other Janus transition-metal dichalcogenides that could improve this effect is also investigated.



- Morten N. Gjerding, Lucas S. R. Cavalcante, Andrey Chaves and Kristian S. Thygesen. *Efficient Ab-Initio Based Modeling of Dielectric Screening in 2D Van Der Waals Materials: Including Phonons, Substrates, and Doping*. The Journal of Physical Chemistry C (2020). DOI: 10.1021/acs.jpcc.0c01635

RETURN TO JUST ACCEPTED MANUSCRIPTS | < PREV C: PLASMONICS; OPTIC... NEXT >

Efficient Ab-Initio Based Modeling of Dielectric Screening in 2D Van Der Waals Materials: Including Phonons, Substrates, and Doping

Morten N. Gjerding, Lucas S. R. Cavalcante, Andrey Chaves and Kristian S. Thygesen

Cite this: *J. Phys. Chem. C* 2020, XXXX, XXX, XXX-XXX

XXX




Publication Date: May 4, 2020 -

<https://doi.org/10.1021/acs.jpcc.0c01635>

Copyright © 2020 American Chemical Society


[RIGHTS & PERMISSIONS](#)

Article Views 3 Altmetric Citations - -
LEARN ABOUT THESE METRICS

Share Add to Export
  



The Journal of Physical Chemistry C

 PDF (4 MB)

Abstract

The quantum electrostatic heterostructure (QEH) model allows for efficient computation of the dielectric screening properties of layered van der Waals bonded heterostructures in terms of the dielectric functions of the individual two-dimensional (2D) layers. Here, we extend the QEH model by including: (1) Contributions to the dielectric function from infrared active phonons in the 2D layers, (2) screening from homogeneous bulk substrates, and (3) intraband screening from free carriers in doped 2D semiconductor layers. We demonstrate the potential of the extended QEH model by calculating the dispersion of coupled phonons in multilayer stacks of hexagonal boron-nitride (hBN), the strong hybridization of plasmons and optical phonons in graphene/hBN heterostructures, the effect of substrate screening on the exciton series of monolayer MoS₂, and the properties of hyperbolic plasmons in a doped phosphorene sheet. The new QEH code is distributed as a Python package with a simple command line interface and a comprehensive library of dielectric building blocks for the most common 2D materials, providing an efficient open platform for dielectric modeling of realistic vdW heterostructures.

Bibliography

- [1] Novoselov, K. S. *et al.* Electric field in atomically thin carbon films. *Science* **306**, 666–669 (2004).
- [2] Mak, K. F., Lee, C., Hone, J., Shan, J. & Heinz, T. F. Atomically Thin MoS₂: A New Direct-Gap Semiconductor. *Physical Review Letters* **105**, 136805 (2010).
- [3] Manzeli, S., Ovchinnikov, D., Pasquier, D., Yazyev, O. V. & Kis, A. 2D transition metal dichalcogenides. *Nature Reviews Materials* **2**, 17033 (2017).
- [4] Li, L. *et al.* Black phosphorus field-effect transistors. *Nature Nanotechnology* **9**, 372–377 (2014).
- [5] Castellanos-Gomez, A. Black Phosphorus: Narrow Gap, Wide Applications. *Journal of Physical Chemistry Letters* **6**, 4280–4291 (2015).
- [6] Duan, X., Wang, C., Pan, A., Yu, R. & Duan, X. Two-dimensional transition metal dichalcogenides as atomically thin semiconductors: opportunities and challenges. *Chemical Society Reviews* **44**, 8859–8876 (2015).
- [7] Molina-Sánchez, A., Sangalli, D., Hummer, K., Marini, A. & Wirtz, L. Effect of spin-orbit interaction on the optical spectra of single-layer, double-layer, and bulk MoS₂. *Physical Review B* **88**, 045412 (2013).
- [8] Aslan, O. B., Chenet, D. A., van der Zande, A. M., Hone, J. C. & Heinz, T. F. Linearly Polarized Excitons in Single- and Few-Layer ReS₂ Crystals. *ACS Photonics* **3**, 96–101 (2016).
- [9] Chernikov, A. *et al.* Exciton Binding Energy and Nonhydrogenic Rydberg Series in Monolayer WS₂. *Physical Review Letters* **113**, 076802 (2014).
- [10] Mai, C. *et al.* Many-Body Effects in Valleytronics: Direct Measurement of Valley Lifetimes in Single-Layer MoS₂. *Nano Letters* **14**, 202–206 (2014).

-
- [11] Plechinger, G. *et al.* Identification of excitons, trions and biexcitons in single-layer WS₂. *physica status solidi (RRL) - Rapid Research Letters* **9**, 457–461 (2015).
- [12] You, Y. *et al.* Observation of biexcitons in monolayer WSe₂. *Nature Physics* **11**, 477–481 (2015).
- [13] Mayers, M. Z., Berkelbach, T. C., Hybertsen, M. S. & Reichman, D. R. Binding energies and spatial structures of small carrier complexes in monolayer transition-metal dichalcogenides via diffusion Monte Carlo. *Physical Review B* **92**, 161404 (2015).
- [14] Jariwala, D., Sangwan, V. K., Lauhon, L. J., Marks, T. J. & Hersam, M. C. Emerging Device Applications for Semiconducting Two-Dimensional Transition Metal Dichalcogenides. *ACS Nano* **8**, 1102–1120 (2014).
- [15] Pospischil, A., Furchi, M. M. & Mueller, T. Solar-energy conversion and light emission in an atomic monolayer p–n diode. *Nature Nanotechnology* **9**, 257–261 (2014).
- [16] Furchi, M. M., Pospischil, A., Libisch, F., Burgdörfer, J. & Mueller, T. Photovoltaic Effect in an Electrically Tunable van der Waals Heterojunction. *Nano Letters* **14**, 4785–4791 (2014).
- [17] Engel, M., Steiner, M. & Avouris, P. Black Phosphorus Photodetector for Multi-spectral, High-Resolution Imaging. *Nano Letters* **14**, 6414–6417 (2014).
- [18] Gong, K. *et al.* Electric control of spin in monolayer WSe₂ field effect transistors. *Nanotechnology* **25**, 435201 (2014).
- [19] Geim, A. K. & Grigorieva, I. V. Van der Waals heterostructures. *Nature* **499**, 419–425 (2013).
- [20] Withers, F. *et al.* Light-emitting diodes by band-structure engineering in van der Waals heterostructures. *Nature Materials* **14**, 301–306 (2015).
- [21] Massicotte, M. *et al.* Picosecond photoresponse in van der Waals heterostructures. *Nature Nanotechnology* **11**, 42–46 (2016).
- [22] Britnell, L. *et al.* Field-effect tunneling transistor based on vertical graphene heterostructures. *Science (New York, N.Y.)* **335**, 947–50 (2012).
- [23] Georgiou, T. *et al.* Vertical field-effect transistor based on graphene–WS₂ heterostructures for flexible and transparent electronics. *Nature Nanotechnology* **8**, 100–103 (2013).

- [24] Schmidt, P. *et al.* Nano-imaging of intersubband transitions in van der Waals quantum wells. *Nature Nanotechnology* **13**, 1035–1041 (2018).
- [25] Bistritzer, R. & MacDonald, A. H. Moire bands in twisted double-layer graphene. *Proceedings of the National Academy of Sciences of the United States of America* **108**, 12233–7 (2011).
- [26] Yankowitz, M. *et al.* Tuning superconductivity in twisted bilayer graphene. *Science (New York, N.Y.)* **363**, 1059–1064 (2019).
- [27] Cui, X. *et al.* Multi-terminal transport measurements of MoS₂ using a van der Waals heterostructure device platform. *Nature Nanotechnology* **10**, 534–540 (2015).
- [28] Rivera, P. *et al.* Observation of long-lived interlayer excitons in monolayer MoSe₂–WSe₂ heterostructures. *Nature Communications* **6**, 6242 (2015).
- [29] Fogler, M. M., Butov, L. V. & Novoselov, K. S. High-temperature superfluidity with indirect excitons in van der Waals heterostructures. *Nature Communications* **5**, 4555 (2014).
- [30] Combescot, M. & Shiau, S.-Y. *Excitons and cooper pairs : two composite bosons in many-body physics* (Oxford University Press, 2016).
- [31] Ashcroft, N. W. & Mermin, N. D. *Solid state physics* (Holt, Rinehart and Winston, 1976).
- [32] Frenkel, J. On the transformation of light into heat in solids. i. *Physical Review* **37**, 17–44 (1931).
- [33] Wannier, G. H. The structure of electronic excitation levels in insulating crystals. *Physical Review* **52**, 191–197 (1937).
- [34] Hayashi, M. & Katsuki, K. Absorption Spectrum of Cuprous Oxide. *Journal of the Physical Society of Japan* **5**, 380–381 (1950).
- [35] Gross, E. F. & Karryef, N. A. *Doklady Akademii NaukSSSR* **84**, 471 (1952).
- [36] Kazimierczuk, T., Fröhlich, D., Scheel, S., Stolz, H. & Bayer, M. Giant Rydberg excitons in the copper oxide Cu₂O. *Nature* **514**, 343–347 (2014).
- [37] Mak, K. F. & Shan, J. Photonics and optoelectronics of 2D semiconductor transition metal dichalcogenides. *Nature Photonics* **10**, 216–226 (2016).
- [38] Mak, K. F. *et al.* Tightly bound trions in monolayer MoS₂. *Nature Materials* **12**, 207–211 (2013).

- [39] Ando, T., Fowler, A. B. & Stern, F. Electronic properties of two-dimensional systems. *Reviews of Modern Physics* **54**, 437–672 (1982).
- [40] Bhimanapati, G. R. *et al.* Recent Advances in Two-Dimensional Materials beyond Graphene. *ACS Nano* **9**, 11509–11539 (2015).
- [41] Tan, C. *et al.* Recent Advances in Ultrathin Two-Dimensional Nanomaterials. *Chemical Reviews* **117**, 6225–6331 (2017).
- [42] Basov, D. N., Fogler, M. M. & García de Abajo, F. J. Polaritons in van der Waals materials. *Science (New York, N.Y.)* **354**, aag1992 (2016).
- [43] Low, T. *et al.* Polaritons in layered two-dimensional materials. *Nature Materials* **16**, 182–194 (2017).
- [44] Wang, G. *et al.* *<i>Colloquium</i>* : Excitons in atomically thin transition metal dichalcogenides. *Reviews of Modern Physics* **90**, 021001 (2018).
- [45] Ugeda, M. M. *et al.* Giant bandgap renormalization and excitonic effects in a monolayer transition metal dichalcogenide semiconductor. *Nature Materials* **13**, 1091–1095 (2014).
- [46] Thygesen, K. S. Calculating excitons, plasmons, and quasiparticles in 2D materials and van der Waals heterostructures. *2D Materials* **4**, 022004 (2017).
- [47] Berkelbach, T. C., Hybertsen, M. S. & Reichman, D. R. Theory of neutral and charged excitons in monolayer transition metal dichalcogenides. *Physical Review B - Condensed Matter and Materials Physics* **88**, 045318 (2013).
- [48] Drüppel, M., Deilmann, T., Krüger, P. & Rohlfing, M. Diversity of trion states and substrate effects in the optical properties of an MoS2 monolayer. *Nature Communications* **8**, 2117 (2017).
- [49] He, K. *et al.* Tightly Bound Excitons in Monolayer WSe 2. *Physical Review Letters* **113**, 026803 (2014).
- [50] Rytova, N. S. The screened potential of a point charge in a thin film. *Moscow University Physics Bulletin* **3**, 18 (1967).
- [51] Keldysh, L. V. Coulomb interaction in thin semiconductor and semimetal films. *Journal of Experimental and Theoretical Physics Letters, Vol. 29, p.658* **29**, 658 (1979).
- [52] Andersen, K., Latini, S. & Thygesen, K. S. Dielectric genome of van der Waals heterostructures. *Nano Letters* **15**, 4616–4621 (2015).

- [53] Latini, S., Olsen, T. & Thygesen, K. S. Excitons in van der Waals heterostructures: The important role of dielectric screening. *Physical Review B* **92**, 245123 (2015).
- [54] Olsen, T., Latini, S., Rasmussen, F. & Thygesen, K. S. Simple Screened Hydrogen Model of Excitons in Two-Dimensional Materials. *Physical Review Letters* **116**, 056401 (2016).
- [55] Raja, A. *et al.* Coulomb engineering of the bandgap and excitons in two-dimensional materials. *Nature Communications* **8**, 15251 (2017).
- [56] Mostaani, E. *et al.* Diffusion quantum Monte Carlo study of excitonic complexes in two-dimensional transition-metal dichalcogenides. *Physical Review B* **96**, 075431 (2017).
- [57] Kunstmann, J. *et al.* Momentum-space indirect interlayer excitons in transition-metal dichalcogenide van der Waals heterostructures. *Nature Physics* **14**, 801–805 (2018).
- [58] Zhang, G. *et al.* Infrared fingerprints of few-layer black phosphorus. *Nature Communications* **8**, 14071 (2017).
- [59] Li, L. *et al.* Direct observation of the layer-dependent electronic structure in phosphorene. *Nature Nanotechnology* **12**, 21–25 (2017).
- [60] Chaves, A., Azadani, J. G., Özçelik, V. O., Grassi, R. & Low, T. Electrical control of excitons in van der Waals heterostructures with type-II band alignment. *Physical Review B* **98**, 121302 (2018).
- [61] Huang, D. & Kaxiras, E. Electric field tuning of band offsets in transition metal dichalcogenides. *Physical Review B* **94**, 241303 (2016).
- [62] Koshino, M. Interlayer screening effect in graphene multilayers with A B A and A B C stacking. *Physical Review B* **81**, 125304 (2010).
- [63] Kuroda, M. A., Tersoff, J., Nistor, R. A. & Martyna, G. J. Optimal Thickness for Charge Transfer in Multilayer Graphene Electrodes. *Physical Review Applied* **1**, 014005 (2014).
- [64] Lui, C. H. *et al.* Imaging Stacking Order in Few-Layer Graphene. *Nano Letters* **11**, 164–169 (2011).
- [65] Liu, H. *et al.* Phosphorene: An Unexplored 2D Semiconductor with a High Hole Mobility. *ACS Nano* **8**, 4033–4041 (2014).
- [66] Yan, J. *et al.* Stacking-Dependent Interlayer Coupling in Trilayer MoS₂ with Broken Inversion Symmetry. *Nano Letters* **15**, 8155–8161 (2015).

- [67] van der Zande, A. M. *et al.* Tailoring the Electronic Structure in Bilayer Molybdenum Disulfide via Interlayer Twist. *Nano Letters* **14**, 3869–3875 (2014).
- [68] Rigosi, A. F., Hill, H. M., Li, Y., Chernikov, A. & Heinz, T. F. Probing Interlayer Interactions in Transition Metal Dichalcogenide Heterostructures by Optical Spectroscopy: MoS₂/WS₂ and MoSe₂/WSe₂. *Nano Letters* **15**, 5033–5038 (2015).
- [69] Fang, H. *et al.* Strong interlayer coupling in van der Waals heterostructures built from single-layer chalcogenides. *Proceedings of the National Academy of Sciences of the United States of America* **111**, 6198–202 (2014).
- [70] Chiu, M.-H. *et al.* Determination of band alignment in the single-layer MoS₂/WSe₂ heterojunction. *Nature Communications* **6**, 7666 (2015).
- [71] Nayak, P. K. *et al.* Probing Evolution of Twist-Angle-Dependent Interlayer Excitons in MoSe₂/WSe₂ van der Waals Heterostructures. *ACS Nano* **11**, 4041–4050 (2017).
- [72] Zhu, H. *et al.* Interfacial Charge Transfer Circumventing Momentum Mismatch at Two-Dimensional van der Waals Heterojunctions. *Nano Letters* **17**, 3591–3598 (2017).
- [73] Miller, B. *et al.* Long-Lived Direct and Indirect Interlayer Excitons in van der Waals Heterostructures. *Nano Letters* **17**, 5229–5237 (2017).
- [74] Calman, E. V. *et al.* Indirect excitons in van der Waals heterostructures at room temperature. *Nature Communications* **9**, 1895 (2018).
- [75] Berman, O. L. & Kezerashvili, R. Y. Superfluidity of dipolar excitons in a transition metal dichalcogenide double layer. *Physical Review B* **96**, 094502 (2017).
- [76] Berman, O. L. & Kezerashvili, R. Y. High-temperature superfluidity of the two-component Bose gas in a transition metal dichalcogenide bilayer. *Physical Review B* **93**, 245410 (2016).
- [77] Witham, O., Hunt, R. J. & Drummond, N. D. Stability of trions in coupled quantum wells modeled by two-dimensional bilayers. *Physical Review B* **97**, 075424 (2018).
- [78] Wilson, N. R. *et al.* Determination of band offsets, hybridization, and exciton binding in 2D semiconductor heterostructures. *Science Advances* **3**, e1601832 (2017).
- [79] Onida, G., Reining, L. & Rubio, A. Electronic excitations: density-functional versus many-body Green's-function approaches. *Reviews of Modern Physics* **74**, 601–659 (2002).

- [80] Qiu, D. Y., da Jornada, F. H. & Louie, S. G. Environmental Screening Effects in 2D Materials: Renormalization of the Bandgap, Electronic Structure, and Optical Spectra of Few-Layer Black Phosphorus. *Nano Letters* **17**, 4706–4712 (2017).
- [81] Tran, K. *et al.* Evidence for moiré excitons in van der Waals heterostructures. *Nature* **567**, 71–75 (2019).
- [82] Seyler, K. L. *et al.* Signatures of moiré-trapped valley excitons in MoSe₂/WSe₂ heterobilayers. *Nature* **567**, 66–70 (2019).
- [83] Matthes, L., Pulci, O. & Bechstedt, F. Influence of out-of-plane response on optical properties of two-dimensional materials: First principles approach. *Phys. Rev. B* **94**, 205408 (2016).
- [84] Laturia, A., Van de Put, M. L. & Vandenberghe, W. G. Dielectric properties of hexagonal boron nitride and transition metal dichalcogenides: from monolayer to bulk. *npj 2D Materials and Applications* **2**, 6 (2018).
- [85] Nerl, H. C. *et al.* Probing the local nature of excitons and plasmons in few-layer mos₂. *npj 2D Materials and Applications* **1**, 2 (2017).
- [86] Resta, R. Macroscopic polarization in crystalline dielectrics: the geometric phase approach. *Reviews of Modern Physics* **66**, 899–915 (1994).
- [87] King-Smith, R. D. & Vanderbilt, D. Theory of polarization of crystalline solids. *Physical Review B* **47**, 1651–1654 (1993).
- [88] Enkovaara, J. *et al.* Electronic structure calculations with GPAW: a real-space implementation of the projector augmented-wave method. *Journal of Physics: Condensed Matter* **22**, 253202 (2010).
- [89] Hastrup, S. *et al.* The Computational 2D Materials Database: high-throughput modeling and discovery of atomically thin crystals. *2D Materials* **5**, 042002 (2018).
- [90] The dielectric building blocks and qeh software can be downloaded at <https://cmr.fysik.dtu.dk/vdwh/vdwh.html>.
- [91] Griffiths, D. J. D. J. *Introduction to electrodynamics* (Prentice Hall, 1999).
- [92] Novoselov, K. S., Geim, A. K., Guinea, F., Peres, N. M. R. & Castro Neto, A. H. The electronic properties of graphene. *Reviews of Modern Physics* **81**, 109–162 (2009).
- [93] Wunsch, B., Stauber, T., Sols, F. & Guinea, F. Dynamical polarization of graphene at finite doping. *New Journal of Physics* **8**, 318–318 (2006).

-
- [94] Jablan, M., Buljan, H. & Soljačić, M. Plasmonics in graphene at infrared frequencies. *Physical Review B* **80**, 245435 (2009).
- [95] Gonçalves, P. A. D. & Peres, N. M. R. *An introduction to graphene plasmonics* (WORLD SCIENTIFIC, 2016).
- [96] Bohm, D. & Pines, D. A Collective Description of Electron Interactions. I. Magnetic Interactions. *Physical Review* **82**, 625–634 (1951).
- [97] Pines, D. & Bohm, D. A Collective Description of Electron Interactions: II. Collective vs Individual Particle Aspects of the Interactions. *Physical Review* **85**, 338–353 (1952).
- [98] Bohm, D. & Pines, D. A Collective Description of Electron Interactions: III. Coulomb Interactions in a Degenerate Electron Gas. *Physical Review* **92**, 609–625 (1953).
- [99] Stern, F. Polarizability of a Two-Dimensional Electron Gas. *Physical Review Letters* **18**, 546–548 (1967).
- [100] Maldague, P. F. Many-body corrections to the polarizability of the two-dimensional electron gas. *Surface Science* **73**, 296–302 (1978).
- [101] Andersen, K., Jacobsen, K. W. & Thygesen, K. S. Spatially resolved quantum plasmon modes in metallic nano-films from first-principles. *Physical Review B* **86**, 245129 (2012).
- [102] Sohler, T., Gibertini, M., Calandra, M., Mauri, F. & Marzari, N. Breakdown of Optical Phonons’ Splitting in Two-Dimensional Materials. *Nano Letters* **17**, 3758–3763 (2017).
- [103] Tornatzky, H., Gillen, R., Uchiyama, H. & Maultzsch, J. Phonon dispersion in MoS₂. *Physical Review B* **99**, 144309 (2019).
- [104] Koch, R. J., Seyller, T. & Schaefer, J. A. Strong phonon-plasmon coupled modes in the graphene/silicon carbide heterosystem. *Physical Review B* **82**, 201413 (2010).
- [105] Brar, V. W., Jang, M. S., Sherrott, M., Lopez, J. J. & Atwater, H. A. Highly Confined Tunable Mid-Infrared Plasmonics in Graphene Nanoresonators. *Nano Letters* **13**, 2541–2547 (2013).
- [106] Brar, V. W. *et al.* Hybrid Surface-Phonon-Plasmon Polariton Modes in Graphene/Monolayer h-BN Heterostructures. *Nano Letters* **14**, 3876–3880 (2014).
- [107] Yan, H. *et al.* Damping pathways of mid-infrared plasmons in graphene nanostructures. *Nature Photonics* **7**, 394–399 (2013).

- [108] Woessner, A. *et al.* Highly confined low-loss plasmons in graphene–boron nitride heterostructures. *Nature Materials* **14**, 421–425 (2015).
- [109] Hajian, H., Ghobadi, A., Dereshgi, S. A., Butun, B. & Ozbay, E. Hybrid plasmon–phonon polariton bands in graphene–hexagonal boron nitride metamaterials [Invited]. *Journal of the Optical Society of America B* **34**, D29 (2017).
- [110] Luxmoore, I. J. *et al.* Strong Coupling in the Far-Infrared between Graphene Plasmons and the Surface Optical Phonons of Silicon Dioxide. *ACS Photonics* **1**, 1151–1155 (2014).
- [111] Mele, E. J. Screening of a point charge by an anisotropic medium: Anamorphoses in the method of images. *American Journal of Physics* **69**, 557–562 (2001).
- [112] Liu, K. *et al.* Evolution of interlayer coupling in twisted molybdenum disulfide bilayers. *Nature Communications* **5**, 4966 (2014).
- [113] Xia, F., Wang, H. & Jia, Y. Rediscovering black phosphorus as an anisotropic layered material for optoelectronics and electronics. *Nature Communications* **5**, 4458 (2014).
- [114] Nemilentsau, A., Low, T. & Hanson, G. Anisotropic 2d materials for tunable hyperbolic plasmonics. *Phys. Rev. Lett.* **116**, 066804 (2016).
- [115] Gomez-Diaz, J. S., Tymchenko, M. & Alù, A. Hyperbolic plasmons and topological transitions over uniaxial metasurfaces. *Phys. Rev. Lett.* **114**, 233901 (2015).
- [116] Yan, W., Wubs, M. & Mortensen, N. A. Hyperbolic metamaterials: Nonlocal response regularizes broadband supersingularity. *Phys. Rev. B* **86**, 205429 (2012).
- [117] Wilson, N. P. *et al.* Interlayer valley excitons in heterobilayers of transition metal dichalcogenides. *Nature Nanotechnology* **13**, 1004–1015 (2018).
- [118] Novoselov, K. S., Mishchenko, A., Carvalho, A. & Castro Neto, A. H. 2D materials and van der Waals heterostructures. *Science* **353**, aac9439 (2016).
- [119] Liu, Y. *et al.* Van der Waals heterostructures and devices. *Nature Reviews Materials* **1**, 16042 (2016).
- [120] Cavalcante, L. S. R., Chaves, A., Van Duppen, B., Peeters, F. M. & Reichman, D. R. Electrostatics of electron-hole interactions in van der Waals heterostructures. *Physical Review B* **97**, 125427 (2018).
- [121] Viti, L. *et al.* Heterostructured hBN-BP-hBN nanodetectors at terahertz frequencies. *Advanced Materials* **28**, 7390–7396 (2016).

- [122] Mattheakis, M., Valagiannopoulos, C. A. & Kaxiras, E. Epsilon-near-zero behavior from plasmonic Dirac point: theory and realization using two-dimensional materials. *Physical Review B* **94**, 201404 (2016).
- [123] Tomadin, A. & Polini, M. Theory of the plasma-wave photoresponse of a gated graphene sheet. *Physical Review B* **88**, 205426 (2013).
- [124] Vicarelli, L. *et al.* Graphene field-effect transistors as room-temperature terahertz detectors. *Nature Materials* **11**, 865–871 (2012).
- [125] Koppens, F. H. L. *et al.* Photodetectors based on graphene, other two-dimensional materials and hybrid systems. *Nature Nanotechnology* **9**, 780–793 (2014).
- [126] Strano, M. S., Kis, A., Coleman, J. N., Wang, Q. H. & Kalantar-Zadeh, K. Electronics and optoelectronics of two-dimensional transition metal dichalcogenides. *Nature Nanotechnology* **7**, 699–712 (2012).
- [127] Lu, A. Y. *et al.* Janus monolayers of transition metal dichalcogenides. *Nature Nanotechnology* **12**, 744–749 (2017).
- [128] Riis-Jensen, A. C., Pandey, M. & Thygesen, K. S. Efficient charge separation in 2D janus van der Waals structures with built-in electric fields and intrinsic p-n doping. *Journal of Physical Chemistry C* **122**, 24520–24526 (2018).
- [129] Er, D. *et al.* Prediction of enhanced catalytic activity for hydrogen evolution reaction in Janus transition metal dichalcogenides. *Nano Letters* **18**, 3943–3949 (2018).
- [130] Guo, S.-D. Phonon transport in Janus monolayer MoSSe: a first-principles study. *Physical Chemistry Chemical Physics* **20**, 7236–7242 (2018).
- [131] Hu, T. *et al.* Intrinsic and anisotropic Rashba spin splitting in Janus transition-metal dichalcogenide monolayers. *Physical Review B* **97**, 235404 (2018).
- [132] Markussen, T., Brandbyge, M., Palsgaard, M., Gunst, T. & Thygesen, K. S. Stacked Janus device concepts: abrupt pn-junctions and cross-plane channels. *Nano Letters* **18**, 7275–7281 (2018).
- [133] Grigorenko, A. N., Polini, M. & Novoselov, K. S. Graphene plasmonics. *Nature Photonics* **6**, 749–758 (2012).
- [134] Low, T. & Avouris, P. Graphene plasmonics for terahertz to mid-infrared applications. *ACS Nano* **8**, 1086–1101 (2014).
- [135] Constant, T. J., Horneet, S. M., Chang, D. E. & Hendry, E. All-optical generation of surface plasmons in graphene. *Nature Physics* **12**, 124–127 (2016).

- [136] Koppens, F. H. L., Chang, D. E. & García de Abajo, F. J. Graphene plasmonics: a platform for strong light-matter interactions. *Nano Letters* **11**, 3370–3377 (2011).
- [137] Politano, A. & Chiarello, G. Plasmon modes in graphene: status and prospect. *Nanoscale* **6**, 10927–10940 (2014).
- [138] Shirodkar, S. N. *et al.* Quantum plasmons with optical-range frequencies in doped few-layer graphene. *Physical Review B* **97**, 195435 (2018).
- [139] Agarwal, A., Vitiello, M. S., Viti, L., Cupolillo, A. & Politano, A. Plasmonics with two-dimensional semiconductors: from basic research to technological applications. *Nanoscale* **10**, 8938–8946 (2018).
- [140] Zhang, J. *et al.* Janus monolayer transition-metal dichalcogenides. *ACS Nano* **11**, 8192–8198 (2017).
- [141] Li, F., Wei, W., Zhao, P., Huang, B. & Dai, Y. Electronic and optical properties of pristine and vertical and lateral heterostructures of Janus MoSSe and WSSe. *Journal of Physical Chemistry Letters* **8**, 5959–5965 (2017).
- [142] Meng, M., Li, T., Li, S. & Liu, K. Ferromagnetism induced by point defect in Janus monolayer MoSSe regulated by strain engineering. *Journal of Physics D: Applied Physics* **51**, 105004 (2018).
- [143] Mermin, N. D. Lindhard dielectric function in the relaxation-time approximation. *Physical Review B* **1**, 2362–2363 (1970).
- [144] Bezares, F. J. *et al.* Intrinsic plasmon-phonon interactions in highly doped graphene: a near-field imaging study. *Nano Letters* **17**, 5908–5913 (2017).
- [145] Freitag, M. *et al.* Photocurrent in graphene harnessed by tunable intrinsic plasmons. *Nature Communications* **4**, 1951 (2013).
- [146] Principi, A., Asgari, R. & Polini, M. Acoustic plasmons and composite hole-acoustic plasmon satellite bands in graphene on a metal gate. *Solid State Communications* **151**, 1627–1630 (2011).
- [147] Politano, A. *et al.* Evidence for acoustic-like plasmons on epitaxial graphene on Pt(111). *Physical Review B* **84**, 033401 (2011).
- [148] Alonso-González, P. *et al.* Acoustic terahertz graphene plasmons revealed by photocurrent nanoscopy. *Nature Nanotechnology* **12**, 31–35 (2017).
- [149] Politano, A., Yu, H. K., Farías, D. & Chiarello, G. Multiple acoustic surface plasmons in graphene/Cu(111) contacts. *Physical Review B* **97**, 035414 (2018).

- [150] Lee, I.-H., Yoo, D., Avouris, P., Low, T. & Oh, S.-H. Graphene acoustic plasmon resonator for ultrasensitive infrared spectroscopy. *Nature Nanotechnology* **14**, 313–319 (2019).
- [151] Torre, I. *et al.* Acoustic plasmons at the crossover between the collisionless and hydrodynamic regimes in two-dimensional electron liquids. *Physical Review B* **99**, 144307 (2019).
- [152] Luo, Y. F., Pang, Y., Tang, M., Song, Q. & Wang, M. Electronic properties of Janus MoSSe nanotubes. *Computational Materials Science* **156**, 315–320 (2019).
- [153] Stark, J. Observation of the separation of spectral lines by an electric field [7]. *Nature* **92**, 401 (1913).
- [154] Poem, E. *et al.* Accessing the dark exciton with light. *Nature Physics* **6**, 993–997 (2010).
- [155] Bishop, D. M. Polarizability and hyperpolarizability of atoms and ions. *Theoretical and Computational Chemistry* **6**, 129–146 (1999).
- [156] Kulina, P. & Rinkleff, R. H. Second and fourth order stark shifts in the 6 snd1D2 barium rydberg series. *Zeitschrift für Physik A Atoms and Nuclei* **318**, 251–259 (1984).
- [157] Kulina, P. & Rinkleff, R. H. Fourth-order Stark effect in the 4s21d 1D2 Ca Rydberg state. *Journal of Physics B: Atomic and Molecular Physics* **18**, L245–L250 (1985).
- [158] Haseyama, T. *et al.* Second- and fourth-order Stark shifts and their principal-quantum-number dependence in high Rydberg states of 85Rb. *Physics Letters, Section A: General, Atomic and Solid State Physics* **317**, 450–457 (2003).
- [159] Chaves, A., Low, T., Avouris, P., Çakır, D. & Peeters, F. M. Anisotropic exciton Stark shift in black phosphorus. *Physical Review B - Condensed Matter and Materials Physics* **91**, 155311 (2015).
- [160] Chaves, A., Mayers, M. Z., Peeters, F. M. & Reichman, D. R. Theoretical investigation of electron-hole complexes in anisotropic two-dimensional materials. *Physical Review B* **93**, 115314 (2016).
- [161] Chaves, A., Farias, G. A., Peeters, F. M. & Ferreira, R. The split-operator technique for the study of spinorial wavepacket dynamics. *Communications in Computational Physics* **17**, 850–866 (2015).
- [162] Castellanos-Gomez, A. *et al.* Isolation and characterization of few-layer black phosphorus. *2D Materials* **1**, 025001 (2014).

-
- [163] Pedersen, T. G. Exciton Stark shift and electroabsorption in monolayer transition-metal dichalcogenides. *Physical Review B* **94**, 125424 (2016).
- [164] Scharf, B. *et al.* Excitonic Stark effect in MoS₂ monolayers. *Physical Review B* **94**, 245434 (2016).
- [165] Haastrup, S., Latini, S., Bolotin, K. & Thygesen, K. S. Stark shift and electric-field-induced dissociation of excitons in monolayer MoS₂ and h BN/ MoS₂ heterostructures. *Physical Review B* **94**, 041401 (2016).
- [166] Massicotte, M. *et al.* Dissociation of two-dimensional excitons in monolayer WSe₂. *Nature Communications* **9**, 1633 (2018).
- [167] Van Der Donck, M., Zarenia, M. & Peeters, F. M. Excitons and trions in monolayer transition metal dichalcogenides: A comparative study between the multiband model and the quadratic single-band model. *Physical Review B* **96**, 035131 (2017).
- [168] Shepard, G. D. *et al.* Trion-Species-Resolved Quantum Beats in MoSe₂. *ACS Nano* **11**, 11550–11558 (2017).
- [169] Klein, J. *et al.* Stark Effect Spectroscopy of Mono- and Few-Layer MoS₂. *Nano Letters* **16**, 1554–1559 (2016).
- [170] Tran, V., Soklaski, R., Liang, Y. & Yang, L. Layer-controlled band gap and anisotropic excitons in few-layer black phosphorus. *Physical Review B - Condensed Matter and Materials Physics* **89**, 235319 (2014).
- [171] Needs, R. J., Towler, M. D., Drummond, N. D. & López Ríos, P. Continuum variational and diffusion quantum Monte Carlo calculations. *Journal of Physics: Condensed Matter* **22**, 023201 (2010).